Design of Minimally Actuated Legged Milli-Robots Using Compliant Mechanisms and Folding

by

Aaron Murdock Hoover

B.S. (Stanford University) 1999
M.S. (University of California, Berkeley) 2006

A dissertation submitted in partial satisfaction
of the requirements for the degree of

Doctor of Philosophy

in

Engineering - Mechanical Engineering

in the

GRADUATE DIVISION

of the

UNIVERSITY OF CALIFORNIA, BERKELEY

Committee in charge:

Professor Ronald S. Fearing, Co-chair
Professor Dennis K. Lieu, Co-chair
Professor Albert P. Pisano
Professor Carlo H. Séquin

Spring 2010

Design of Minimally Actuated Legged Milli-Robots Using Compliant Mechanisms and Folding

by

Aaron Murdock Hoover

Abstract

Design of Minimally Actuated Legged Milli-Robots Using Compliant Mechanisms and Folding

by

Aaron Murdock Hoover

Doctor of Philosophy in Engineering - Mechanical Engineering

University of California, Berkeley

Professor Ronald S. Fearing, Co-Chair

Professor Dennis K. Lieu, Co-Chair

This thesis explores milli- and meso-scale legged robot design and fabrication with compliant mechanisms. Our approach makes use of a process that integrates compliant flexure hinges and rigid links to form parallel kinematic structures through the folding of flat-fabricated sheets of articulated parts. Using screw theory, we propose the formulation of an equivalent mechanism compliance for a class of parallel mechanisms, and we use that compliance to evaluate a scalar performance metric based on the strain energy stored in a mechanism subjected to an arbitrary load. Results from the model are supported by experimental measurements of a representative mechanism. With the insight gained from the kinematic mechanism design analysis, we propose and demonstrate compliant designs for two six-legged robots comprising the robotic, autonomous, crawling hexapod (*RoACH*) family of robots. *RoACH* is a two degree of freedom, 2.4 gram, 3 cm long robot capable of untethered, sustained, steerable locomotion. *RoACH*'s successor, *DynaRoach*, is 10 cm long, has one actuated degree of freedom and is capable of running speeds of up to 1.4 m/s. *DynaRoACH* employs compliant legs to help enable dynamic running and maneuvering and is three orders of magnitude more efficient than its milli-scale predecessor. We

experimentally demonstrate the feasibility of a biologically-inspired approach to turning control and dynamic maneuvering by adjusting leg stiffness. While the result agrees qualitatively with predictions from existing reduced order models, initial data suggest the full 3-dimensional dynamics play an important role in six-legged turning.

To my grandmother, Millicent Murdock.

Contents

List of Figures

List of Tables

Acknowledgements

First and foremost I would like to thank my advisor, Professor Ron Fearing. His support, guidance, and knowledge over these past six years cannot be measured. It's truly been a pleasure to learn from him and to have him as a mentor.

When I joined the Biomimetic Millisystems lab, I was stunned by the talent, patience, and willingness to help demonstrated by the graduate students and post-docs alike. Rick Groff was incredibly helpful with everything from prelim exam problems to paper edits. Srinath Avadhanula demonstrated an uncanny willingness to teach me new concepts and suggest solutions to research problems I was facing. Rob Wood gave me an invaluable education in the art of trash-talking on the foosball table - a skill that continues to come in handy today. Carmel Majidi has helped me out of more than one continuum modeling jam and continues to be a good friend to this day. Finally, enormous thanks go to Erik Steltz who is responsible for my barely passable circuits and embedded systems literacy.

In recent years, I've had the good fortune to be surrounded by great labmates who've provided stimulating discussions and welcome distractions. In particular, Jongho Lee, Stan Baek, Paul Birkmeyer, and Kevin Peterson have demonstrated admirable willingness to shirk all academic responsibilities in the service of a good game of ping pong. To Bryan Schubert and Andrew Gillies I offer sincere thanks for a willingness to engage any problem and provide valuable insight even in areas unrelated to their specialties. Xiao-Yu Fu deserves many thanks for being the best "post-undergrad" assistant a graduate student could ask for. Without his help over the past six months, this dissertation wouldn't be finished right now.

I'd also like to thank all of the undergraduates I've had the opportunity to work with over the years - Minerva Pillai, Dianne Weeks, Andrew Parra, and Maribel Hudson. They each helped teach me a lot about how to improve as a mentor, and I've thoroughly enjoyed keeping in touch with them and learning about their latest academic exploits.

For educating me in the mysterious ways of biology I must thank Professors Bob Full, Robert

Dudley, and Mimi Koehl. For providing a truly memorable experience in my computer graphics coursework and later valuable feedback as one of my committee members I thank Carlo Séquin. His passion for engineering and intense curiosity are infectious, and I am humbled by his geometric problem-solving intuition.

As my time in Berkeley draws to a close, I can reflect fondly on many pleasant experiences of first making new friends through shared intellectual interests and then watching those friendships grow over coffee and lunch and the occasional beer. Among the many friends who've made Berkeley a supremely enjoyable experience Athulan Vijayaraghavan, Alan Van Pelt, Yonatan Munk, and Maria José Fernandez stand out. Most recently, I've also had the pleasure of working with and getting to know Sam Burden. I look forward to continuing to collaborate with him and possibly even one day having the opportunity to "wheeeze the joooo hooose."

Finally, I would like to thank my family. My sister, Melissa, and my mom, Kathy, have been unwavering in their support of me. They've always expressed a sincere interest in my work and genuine desire for me to succeed. Most of all, I want thank my fiancée, Robin, for all her care and loving support throughout my graduate career. It wasn't always clear that keeping me sane was a task that could be accomplished, but she took up the mantle and did it with aplomb.

Part I

Introduction and Background

Chapter 1

Introduction

Any intelligent fool can make things bigger, more complex, and more violent. It takes a touch of genius – and a lot of courage – to move in the opposite direction.

-Albert Einstein

Though much maligned, the humble cockroach is one of nature's most remarkable examples of high performance legged locomotion. The American cockroach, *Periplaneta americana*, for example, is capable of achieving running speeds of up to 50 body lengths per second [33][27]. It can traverse rough and smooth terrains alike with little or no modification to the train of neural signals activating its leg muscles [82], and it shows remarkable robustness to disturbances ranging from forced vertical running transitions, to falls from heights of many body lengths, to loss of entire limbs [26]. Finally, anyone who's ever attempted to squash one of these bugs can't help but appreciate its unparalleled toughness.

From a robotics perspective, a system with the characteristics of a cockroach represents the "holy grail" of terrestrial locomotion. With the ability to nimbly run over loose or rugged terrain and climb vertical surfaces quickly, a very small legged robot could prove invaluable for penetrating tiny openings in rubble to search for survivors after an earthquake. Many nearly unnoticeable bug-like robots equipped with sensors and radios could be quickly dispersed over a region to form a reconfigurable, mobile sensor network that could have applications like surveillance, or environmental and structural monitoring in sensitive areas. Finally, large numbers of small, inexpensive legged robots, each programmed with a simple set of local rules, could be used to study emergent, or swarm behavior on dynamic platforms.

However, the design and development of such small scale legged robots is still in its nascency, and challenging engineering problems abound. In some cases, biological insight is helpful - organisms often utilize strategies that are remarkably simple, yet elegant, to solve problems of locomotion like gait coordination, robustness to disturbances, and maneuverability. In other cases, we must draw upon our knowledge of engineered systems to solve problems inherent to building

robots at the small scale like the fabrication and actuation of mechanisms. The broad goal of this thesis is to combine engineering insights, with biological inspiration where appropriate, to design and build legged robots at or near the size scale of some of nature's most incredible locomotion "machines" - cockroaches. While the design approach as well as the robot designs themselves in this thesis have yielded a certain amount of success with respect to that goal, the work presented here represents just the first steps in the direction of truly capable legged robots at the insect scale.

1.1 Design and Fabrication Challenges for Milliscale Mobile Robots

The quest to build a capable legged robot at the scale of a cockroach is ambitious. Organisms themselves are "assembled" from a complex hierarchy of materials comprising cells, tissues, and organs at levels of increasing complexity and organization. Furthermore, evolution has had millions of years to tune their fitness, constantly refining and improving upon previous generations of designs.

Nonetheless, we are drawn to the challenge of engineering very small robots at the millimeter scale (millirobots) because they have great potential as mobile robotic platforms. Millirobots' small size provides myriad advantages compared to their larger robot counterparts: it enables them to operate in environments where large robots would be impractical or impossible; at a few dollars per robot, their low cost means they could be produced in large quantities inexpensively; large numbers of them can be networked to form highly mobile and robust sensor and communication networks [54]. By distributing the challenges of mobility, computation, and sensing, it is possible to gain overall system robustness and added capability compared to a single, large mobile robot.

In addition to those features mentioned above, small robots have another unique advantage over large robots: their surface area to volume (and therefore mass) ratio is relatively high. One important ramification of this fact is that fluid drag force (which scales proportionally to surface area) begins to dominate inertial forces associated with the robot's mass at speeds that are relevant to everyday operation. This can create striking physical robustness on par with some of nature's most resilient arthropods by, for example, enabling a small legged robot to survive falls at its terminal velocity [15].

However, designing capable milliscale robotic systems means first addressing some engineering challenges that are unique to the small scale. As mechanical systems shrink in size, the nature of the forces acting on the system components begins to change. Inertial forces scale with robot volume or proportionally to L^3 where L is some characteristic dimension. Surfaces forces like electrostatic attraction, Van der Waals, and capillary scale with surface area or proportionally to L^2 [30]. Thus the ratio of the surfaces forces to inertial forces scales as:

$$\frac{\text{Surface Forces}}{\text{Inertial Forces}} \propto \frac{1}{L} \tag{1.1}$$

Minimizing the mechanical interaction of surfaces becomes relatively more important as size decreases. Additional constraints imposed by small size mean milliscale robotic system designs necessarily become tightly coupled and the design must be considered holistically rather than as a aggregate of subsystems.

A major contribution that attempts to address this issue of tight system coupling at the milliscale has come from the UC Berkeley Biomimetic Millisystems Lab in the form of the smart composite microstructures (SCM) paradigm [91]. At its core, SCM is a planar fabrication process that integrates rigid, fiber-reinforced polymer composites with compliant homogeneous polymer films to create structures that can be folded up into functional, articulated compliant mechanisms whose mobility is enabled by elastic deformation of flexural elements. In addition to enabling the creation of milliscale articulated mechanisms, SCM structures can be directly integrated with a variety of "smart" material actuators [94][73][45] as well as wiring [74][23]. The first successful millirobotic structure to make use of SCM was the Berkeley micromechanical flying insect (MFI) [90].

Robots produced by the SCM process typically consist of complex interconnections of parallel kinematic structures whose design is driven by a need to minimize the number of actuators required to control their motion. In previous millirobotic designs [95][9][73] a large amount of work has gone into devising mechanical transmissions capable of converting typically small motions of actuators [94] into large, coordinated outputs of wings or legs. In the purely kinematic design phase, these mechanisms may be modeled as consisting of ideal rigid links connected by ideal revolute joints with zero stiffness. This is a convenient abstraction from a design perspective as it allows for the design of motion curves and the optimization of mechanisms using traditional geometric approaches to kinematics. In this abstraction an ideal lower pair like a revolute joint enables one degree of freedom and enforces five degrees of constraint. In practice however, SCM produces joints whose mobility is a result of compliance, and those joints have compliance in all directions. The design process for a mechanism comprising these joints and links is therefore one of enabling compliance in desired directions to produce degrees of *freedom* and reducing it in others to create degrees of *constraint*. Successful mechanism and robot designs making use of SCM often require many iterations and rely on the designer's intuition about material behavior and process limitations to tune their performance. To improve the design process, in Chapter 3 we present one approach to modeling and analyzing SCM mechanisms that makes use of screw theory combined with a strain energy-based performance metric from structural design to assess the fitness of SCM mechanism designs.

The SCM process (described in more detail in Chapter 3) is a powerful tool enabling the fabrication of very small robots, but it also comes with some drawbacks. As with any small-scale fabrication technology, design and assembly can be time-consuming and error prone. For example, a typical millirobot design like the UC Berkeley micromechanical flying insect (MFI) [10] shown in Fig. 1.1 can have feature dimensions as small as 100μm, requires precise integration of very small actuators [93], and is fabricated from pre-impregnated composite materials [91] which require long cure times. Fabrication of an SCM assembly using pre-impregnated carbon fiber consists of a multi-step process of alternately laser micromachining and curing layers which can take one to two days depending on the complexity of the part. Small feature sizes typically necessitate the use of an optical microscope and delicate and careful hand assembly techniques to ensure kine-

matic integrity of the completed structure. This hand assembly process is error-prone, and errors in assembly can be difficult or sometimes impossible to recover from. Actuators must be precisely aligned to enable the delivery of appropriate forces to the structure and the environment. The overall complexity of these processes makes them time consuming and significantly reduces the rate at which new designs and improvements to existing designs can be implemented. Typically, from the start of cutting to the assembly of a finished artifact can take a minimum of three days. For these reasons, the small-scale process is not well suited for use in the early stages of robotic design during which many ideas and designs will be explored, but most will be discarded.

In our initial attempts to conceive of and build new legged millirobot designs, we were motivated by the above limitations to develop a prototyping process that closely mimics SCM, but eliminates the most time-consuming step of curing composites, as well as painstaking hand assembly at the milliscale. The result is the scaled prototyping process described in Appendix A that uses commonly available, inexpensive materials to reduce the time it takes from days to hours to fabricate and assemble a robot prototype. And, because SCM is a planar approach to creating compliant mechanisms, designs resulting from the scaled prototyping process can be scaled down trivially according to simple geometric scaling rules. Chapter 4 provides a validation of the prototyping approach by demonstrating a functional prototype of a six-legged millirobot at a 2X scale. In the same chapter we demonstrate the feasibility of scaling the prototype to produce an actual autonomous, untethered, legged millirobot at the size scale of a cockroach and capable of sustained steerable walking.

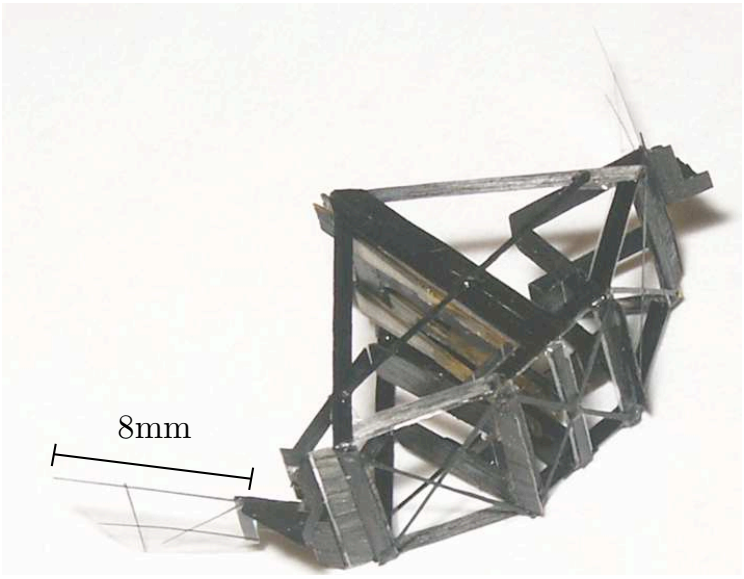

Figure 1.1: An example robot built using the smart composite microstructures (SCM) paradigm - a version of the UC Berkeley micromechanical flying insect from 2006.

1.2 Biological Inspiration

SCM provides an engineering solution for small scale fabrication, but in order for these highly constrained mobile millirobotic systems to be capable of autonomous locomotion, they must be powered and controlled. Actuation, power, and control at the milli-scale are very challenging research problems which require very different approaches from the control systems employed in macro-scale robotic systems. Weight and size constraints restrict the number and size of actuators, making uncontrolled degrees of freedom unavoidable. Limitations on power density impose a trade-off between locomotion and computation; achieving rapid motion restricts the allowable complexity of control algorithms. Taken together, these constraints necessitate increased reliance on mechanical control for these robots. This tight coupling requires the robot designer to consider simultaneously, and in an integrated fashion, issues of fabrication, actuation, power, and control.

In this arena, turning to the biological world for inspiration enables us to extract important principles that can inform our choices in mechanical design, actuation, and control. Although they can be highly complex and sophisticated, there are notable cases in which they use simplified control strategies that still enable high performance locomotion. The cockroach, *Blaberus discoidalis*, can traverse very large obstacles without changing neural activation patterns to its hind leg muscles responsible for propulsion [82], all the while maintaining a roughly constant gait pattern. With regard to maneuverability, the same cockroach can generate asymmetric force patterns that enable it to make fast, dynamic turns with very small modifications of its leg stiffness and gait kinematics [52].

Reduced order dynamic models that attempt to explain these unique system properties like self-stabilization and dynamic turning have recently been the subject of much study [16][17][52][76][71] and are discussed in more detail in Chapter 2. The goal of the work presented in Chapters 4 and 5 is to couple some of these underlying principles from biology with the design and fabrication approaches described in Chapter 3 to enable capable legged robots despite the challenging constraints imposed by working at the small scale.

1.3 Contributions

This work makes the following contributions:

- **Fitness metric for evaluating compliant, folded robot designs** - An approach to analyzing the compliant mechanisms resulting from the SCM process that makes use of an equivalent mechanism stiffness formulation combined with an energy-based metric from structural analysis. The result is a scalar metric that is useful for characterizing the fitness of a folded compliant mechanism design from the perspective of its resistance to off-axis loads. We also demonstrate a qualitative agreement between the theoretical model and experimental results.
- **RoACH - the smallest untethered, autonomous crawling robot to date** - The design and complete kinematic model of a 2.4 gram, untethered hexapedal robot using a modified SCM

process, integrated shape memory alloy wire actuators, and onboard power and control. The robot is steerable and capable of sustained quasi-static locomotion. To the author's knowledge, this robot is the smallest, untethered, power-autonomous legged robot to date.

- **DynaRoACH** - The design and kinematic model of a 24 gram, dynamic hexapod driven by a single DC motor. The robot is capable of dynamic turning by adjusting leg stiffness and, as such, represents the first effort to use a biologically inspired control approach to dynamic turning. We demonstrate a distributed compliance, viscoelastic leg for high-speed running enabling running speeds of up to 14 body lengths per second at stride frequencies of up to 20 Hz. Measurements of the dynamic stiffness of the C-shaped leg are provided, and we demonstrate the feasibility of an actuated leg design using shape memory alloy wire to adjust leg stiffness as well as length.

- **A scaled prototyping process for folded millirobots** - A low-cost, fast, scaled version of the Smart Composite Microstructures process that enables complete design and assembly of a compliant robotic structure from inexpensive materials in just a few hours is presented in Appendix A. The prototyping process enables the robot designer to iterate over a large design space quickly and has already enabled the design of viable new robots in the Biomimetic Millisystems Lab.

Chapter 2

Previous Work

It's not hard to understand the considerable interest among engineers in using lessons from biology to inform the design of mobile robotic systems. Nature provides us with a wealth of exemplary displays of high performance locomotion — cockroaches running over rough terrain [82] [4], geckos climbing a variety of vertical surfaces and even running upside down [51], and fruit flies executing 90° turns called saccades in less than 50 ms [31].

Observing and modeling these systems can reveal important principles that robotics engineers can take advantage of to improve performance, enable novel behaviors, or simply create mobile robots at scales heretofore impossible. In this chapter, we first provide a brief review of models for legged locomotion that have emerged from the study of organisms. These reduced-order models allow us to discern key principles at work in legged systems, but are simple enough to admit parametric analysis in most cases. Following the exposition of the reduced order dynamic models, we present a review of a few of the most recent milli- and meso-scale legged robots, some of which are capable of dynamic locomotion.

2.1 Simple Models for Legged Locomotion

The study of legged locomotion from a biological perspective can be daunting — an enormous number of legged animals exist all with varying morphologies, body sizes, and preferred natural environment. However, biologists have worked to show that some aspects of legged locomotion follow single functions irrespective of body size, leg morphology, or preferred operating environment. For example, two-, four-, six-, and eight-legged animals all demonstrate qualitatively similar ground reaction force patterns [32][33]; animals that vary in body mass over 5 orders of magnitude all use about the same amount of energy to move one kilogram of their body mass one meter [40] (though larger animals do so more efficiently [84]); even despite differing leg numbers many animals use equivalent gaits [6].

Given these similarities across species, morphology, body size, and operating environment, biologists have constructed reduced-order models that attempt to capture features of legged locomotion that are common to a variety of organisms.

2.1.1 Rigid Inverted Pendulum

The simplest model for legged locomotion is the rigid, inverted pendulum model of walking [5][20] restricted to the sagittal plane. Walking is modeled as a point mass atop a massless rigid rod as depicted in Fig. 2.1. In this model, kinetic energy of the mass is exchanged for gravitational potential at the apex of the stride and then back into kinetic energy at the end of the stride. If no double support phase (both legs in contact with the ground) exists, some kinetic energy must be dissipated on foot impact. With a double support phase, the leading leg does negative work on the center of mass while the trailing leg does positive work in redirecting the velocity vector of the center of mass. Stride parameters like length and width (out of plane) can help to explain the energetic cost of walking using this model [58]. And, despite the fact the model is essentially bipedal, it is possible to treat multi-legged locomotion by considering groups of legs (three legs in a six-legged animal, four in an eight-legged animal, etc.) as single functional legs.

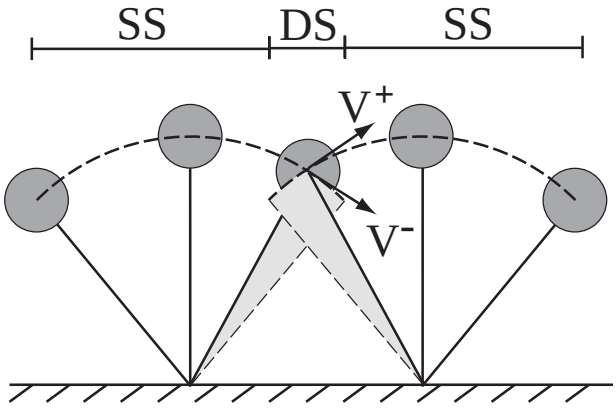

Figure 2.1: Walking modeled as a rigid inverted pendulum. The SS portions are single support in which only one leg is in contact, and DS is double support (light grey shaded areas), during which time both legs are in contact with the ground. V^- is the velocity of the center of mass just before touchdown and V^+ is the velocity of the center of mass just after double support ends.

2.1.2 The Spring-Loaded Inverted Pendulum (SLIP)

The SLIP model [16][17] depicted in Fig. 2.2 is an extension of the inverted pendulum to include vertical compliance of a massless leg. Adding leg compliance makes the model much

more dynamically rich while still restricting the configuration to a tractable number of system parameters that determine performance. Because of the leg compliance, it is possible for the leg to lose contact with the ground at the end of a stride given the appropriate initial conditions. This behavior makes SLIP a *hybrid* dynamical system, that is the time evolution of the state of the system is governed by two distinct sets of differential equations. One set governs the stance phase when the leg is in contact with the ground (beginning at a touchdown event) and the other governs the ballistic or flight phase (beginning at a liftoff event). The system switches between the two continuous vector fields based on events of liftoff (LO) and touchdown (TD). The SLIP model assumes that the touchdown angle of the leg is reset to the same initial value every stride.

Despite being a conservative system, SLIP has been demonstrated to have stable limit cycles [36] using both linear and air spring laws for the spring-loaded legs. More recently, Seipel and Holmes demonstrated the clock-torqued SLIP (CT-SLIP), an actuated version of SLIP that includes damping and a clock-driven torque action at the hip that more accurately predicts performance and stability seen in robots and natural systems with SLIP-like dynamics [78].

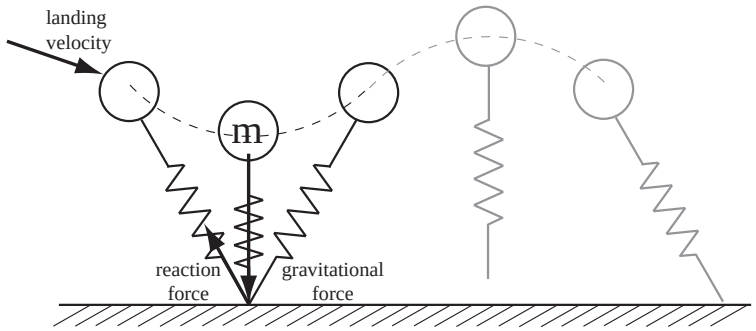

Figure 2.2: A schematic of the spring-loaded inverted pendulum (SLIP) model

2.1.3 The Lateral Leg Spring (LLS)

The LLS is a reduced-order dynamical model of legged locomotion in the horizontal plane [76][77]. The LLS, a schematic of which is shown in Fig. 2.3, was motivated by observation of side-to-side bouncing of cockroaches in the horizontal plane and therefore models legged locomotion in the horizontal plane as a single mass with two legs sprawled out to either side of the body. Like SLIP, the touchdown angle of each leg is prescribed at the beginning of each stride. Motion of the LLS model can be parameterized by the initial leg length, leg touchdown angle, leg stiffness, and the distance of the center of pressure from the center of mass along the major axis of the body. Also like SLIP, despite the fact that it's a conservative dynamical system, LLS shows self-stabilizing properties with respect to heading (velocity vector of the center of mass) and body orientation.

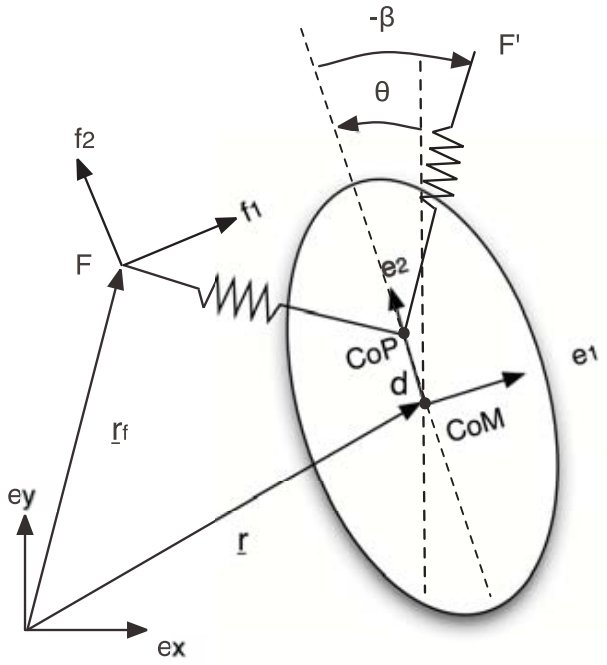

Figure 2.3: A schematic from [76] illustrating the relevant parameters of the lateral leg spring (LLS) model for locomotion in the horizontal plane

LLS and Maneuverability

In addition to the interesting self-stabilizing properties of the LLS model, Proctor and Holmes also demonstrated the possibility of inducing turns simply by momentarily destabilizing the system [71]. Changes to model parameters like leg stiffness and location of the center of pressure with respect to the center of mass can shift the magnitude of one of the eigenvalues of the Jacobian of the stride map to temporarily destabilize the system and cause translational kinetic energy to be exchanged for rotational, thereby inducing a turn. Our experimental results in Chapter 6 provide support for the hypothesis that turning is possible with small differential adjustments to leg stiffness.

2.2 Legged millirobots

Interest in legged millirobots has begun to take off in recent years. Perhaps one of the best indicators of this increased interest is in the commercial availability of milliscale robotic toys. The Hexbug [49] shown in Fig. 2.4 is a 5 cm long, 15.6 g hexapedal legged robot driven by a single motor but still capable of walking (and turning) in reverse. It's equipped with a microphone and bump sensors (at the base of the antennae) that enable it to sense obstacles and noises in order to initiate an escape maneuver that consists of turning while backing up. The Hexbug's kinematics

Figure 2.4: HEXBUG®: A commercially available 16 g, hexapedal millirobot with auditory and touch sensing capabilities.

prevent it from being able to traverse anything but the smoothest surfaces (several pieces of paper stacked are capable of tripping the robot up), but it's nevertheless an impressive robotic toy.

2.2.1 Compliant robots

The first attempt at a legged millirobot using the SCM process came from Sahai *et al.* [73]. The proposed robot depicted in Fig. 2.5a design integrates power, communication, control electronics, and battery into a 35 mm long, 3 g package. The leg drive mechanism consists of a novel kinematic design that couples two piezoelectric bending actuators to the six legs - one to each tripod - through a parallel arrangement of slider crank linkages. Although this robot did not walk due to excessive serial compliance, it was the first legged robot to integrate all systems required for locomotion with the SCM fabrication process.

More recently, work from the Harvard Microrobotics Laboratory has explored using shape memory alloys in a legged millirobot. Fig. 2.5b shows the Harvard Ambulatory Microrobot (HAMR), a 17 mm x 22 mm robot fabricated using the SCM process with ten integrated SMA actuators to control its gait. The robot has been demonstrated at actuation frequencies of up to 1 Hz, and is capable of performing zero radius turns. In addition to actuated locomotion, HAMR is capable of supporting 100 times its own weight while attached to a vertical surface using micro-claws. The robot is powered and controlled by offboard electronics through an attached tether.

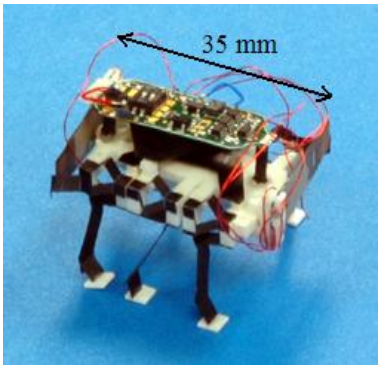

(a)

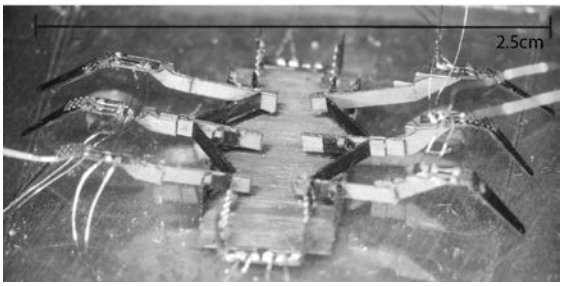

(b)

Figure 2.5: Previous work in legged millirobots using the smart composite microstructures (SCM) fabrication paradigm. (a) A fully integrated, six-legged, piezoelectrically actuated 3 g crawling robot [73]. (b) A mobile six-legged millirobot with eight independent degrees of freedom, actuated with shape memory alloy [12].

2.2.2 MEMS-based robots

Some attempts at locomotion at the millimeter scale have also been made using traditional MEMS processes. Ebefors silicon microrobot [28] is just 15 mm x 5 mm, weighs 80 mg, and is capable of walking at speeds of up to 6 mm/s. Shown in Fig. 2.6a, the robot uses thermal actuators consisting of soft-baked polyimide deposited on silicon in a standard MEMS process. Geometry of the leg joints is such that heating of the polyimide creates a thermal expansion that causes the joint to deflect and the leg to engage the surface. One limitation of this approach is that the thermal actuators require a considerable amount of power (approximately 1.1 W at the fastest actuation speeds) thus, on-board power was deemed infeasible, so the robot operates on a wire tether.

Hollar et al. used a silicon-on-insulator (SOI) process to create a two-legged robot 8.5 mm x 4 mm with a mass of only 10.2 mg [43]. The robot is remarkable in that the mechanical system consisting of compliant joints, rigid silicon legs, and electrostatic inchworm motors, the solar power supply, and a sequencer chip for controlling leg motion are all integrated and on board. In initial tests, the robot was capable of generating 3 mm of sideways motion. The fully integrated system is depicted in Fig. 2.6b

While not strictly legged, Bergbreiter and Pister have developed a MEMS-based robot intended to locomote not by walking or running, but rather by jumping [13]. The design makes use of a novel arrangement of electrostatic inchworm actuators to stretch a micro-rubberband fabricated from molded elastomer. A release mechanism enables very fast release of stored elastic energy ultimately intended to launch the robot into the air. A macro view of the whole robot can be seen in Fig. 2.7c.

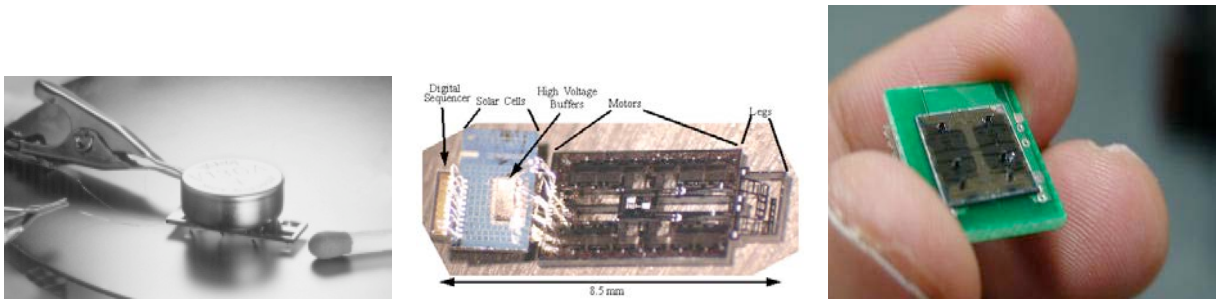

(a) (b) (c)

Figure 2.6: Previous work in legged millirobots using MEMS fabrication technology. (a) A tethered, thermally actuated legged robot from [28]. (b) A mobile two-legged millirobot with integrated solar power and control electronics [43]. (c) The thermally actuated ARRIpede [68], shown with power/control electronics backpack attached.

The most recent legged millirobot built using traditional MEMS processes is the 1 cm x 1 cm, 3.8 g ARRIpede from Murthy et al. [68]. Like Ebefors' robot, the ARRIpede in Fig. 2.6c also uses electrothermal actuators. Unlike Ebefors robot, ARRIpede's actuators are prismatic. With a power consumption of approximately 750 mW, the ARRIpede is capable of walking at 1.5 mm/s. However, the ARRIpede includes a power electronics and battery backpack that enables it to walk untethered and accounts for most of the weight of the robot.

2.3 Dynamic Locomotion

With the exception of Bergbreiter's hopper, all of the robots mentioned above use a quasi-static approach to locomotion. Dynamic locomotion is quite a bit more complex, and the transition from quasi-static locomotion modes like walking to dynamic running or hopping is generally discrete and abrupt. Dynamic locomotion often requires the coordination multiple limbs (or, at the very least, one limb and one body), entails impulsive ground interaction, and can involve complex 6 DOF motions coupling angular and translational degrees of freedom to induce surprising behaviors. However, it is exactly this complicated behavior that makes these dynamic systems a rich area for robotics research.

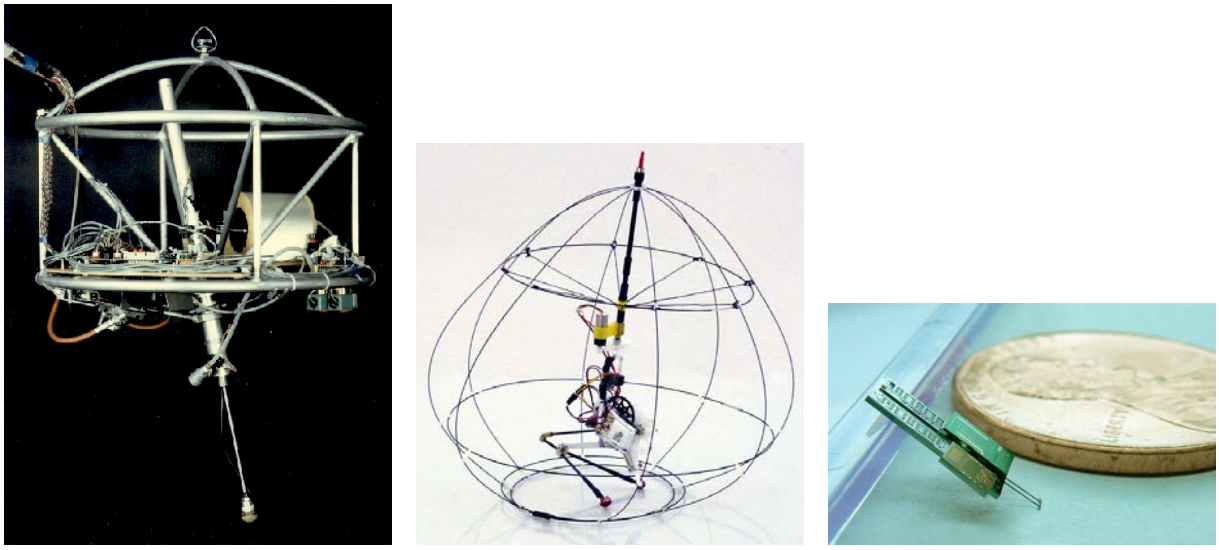

(a) (b) (c)

Figure 2.7: Dynamic hopping robots at the macro-, meso-, and milli-scales. (a) Raibert's self-balancing, hopping 3D monopedal robot [72]. (b) 18 cm tall steerable hopper capable of hopping to heights of more than three times it's body length and reorienting upon landing. [57]. (c) A milliscale hopper fabricated using MEMS technology integrated with elastomers for energy storage [13].

2.3.1 Hopping

In some ways, hopping represents a logical starting point for the study of dynamic legged locomotion. It's inherently dynamic as it often involves the sudden release of stored energy and appropriate redirection or dissipation of that energy on landing. In fact, as is demonstrated in the SLIP abstraction of dynamic running, in the sagittal plane running can be reduced to hopping with some forward speed.

Some of the first successful examples of dynamic legged locomotion were products of research from the Leg Lab at MIT under the direction of Raibert. There, they designed and built the 3D single leg hopping robot shown in Fig. 2.7a. The monopod was capable of balancing itself and following prescribed paths on a flat surface [72]. In addition to the 3D monopedal hopper, Hodgins and Raibert designed, built, and programmed a bipedal robot capable of performing flips [42]. The flipping biped used a simple primarily feedforward, open loop control strategy with some event synchronization based on sensory feedback. Many of Raibert's robots relied on a pneumatic air supply and offboard power and control, so most operated on a tether.

More recently, in the space of hopping robots, Kovač has developed a 14 g, 18 cm spherical hopping robot driven by a single DC motor [57]. The robot uses a cam to wind a spring and rapidly release the elastic energy to hop. The robot depicted in Fig. 2.7b is capable of hopping almost 3.5 times its own height and righting and orienting itself after landing, making it possible for the robot to "steer" itself toward a goal.

2.3.2 Multi-legged Meso-Scale Robots

In the past ten years, a variety of robot designs inspired by running arthropods like cockroaches have emerged. One of the most successful six-legged robots to run dynamically is the RHex robot [75][8], a version of which is shown in Fig. 2.8a. RHex is a 7 Kg, six-legged robot with compliant legs that rotate continuously and are each driven by a single motor. As such, it's capable of mounting obstacles higher than its hip height and has even demonstrated stair-climbing [66] as well as stair descent [19].

Shortly after RHex was developed, the Whegs™family of legged robots was also released, the smallest of which is Mini-Whegs [67]. The Mini-Whegs in Fig. 2.8c is a 150 g quadruped that also uses a hybrid wheel-leg design similar to RHex, but unlike RHex it uses a single motor to drive all four legs, with servo motors to provide steering. At 9 cm long, Mini-Whegs is capable of running 10 body lengths per second and surmounting obstacles approximately 1.5 times the radius of its wheel-legs.

The Sprawl family of robots from Stanford, are also directly inspired by the kinematics and dynamics of cockroach locomotion. Sprawlita [21] is a six-legged robot that's fabricated using a process called shaped deposition manufacturing (SDM) that makes it possible to integrate viscoelastic compliant polymers with rigid, structural polymers as well as enable embedding of sensors and actuators in the actual robot body itself [64]. Sprawlita used pneumatic actuators as primary power

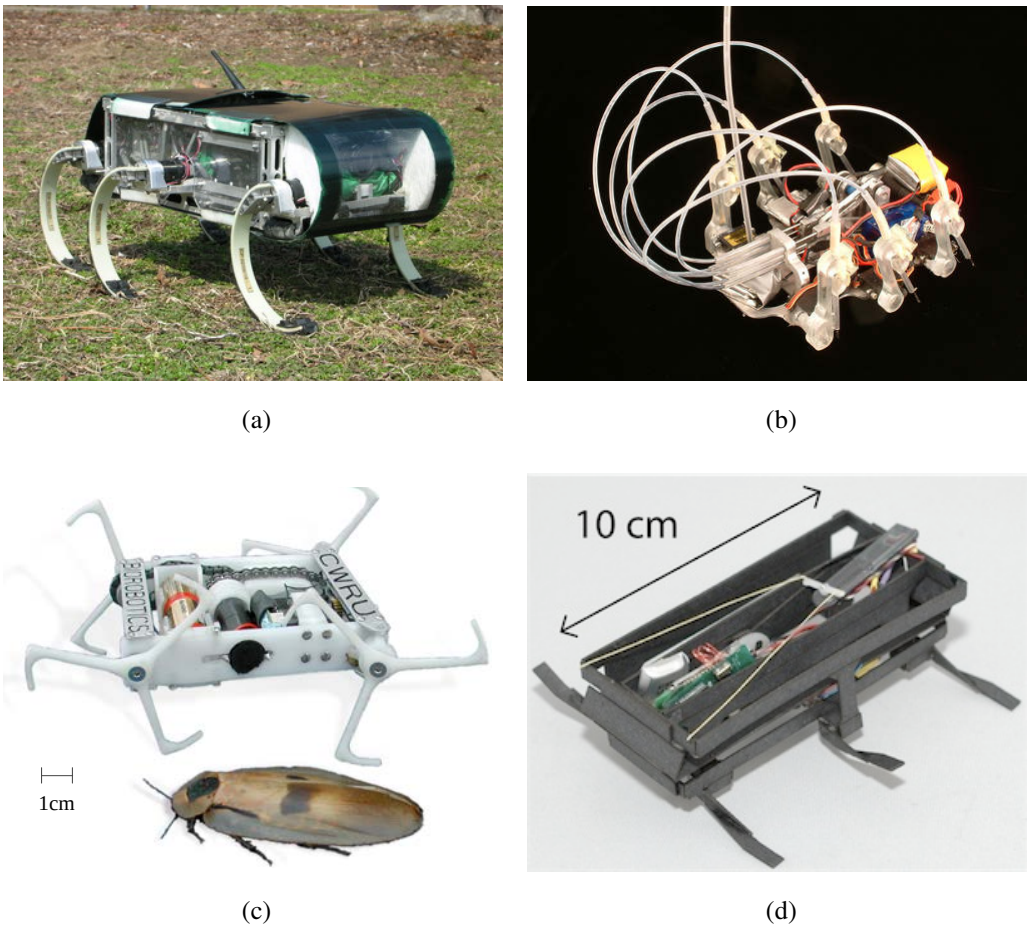

Figure 2.8: Previous work in dynamic, meso-scale, multi-legged running robots. (a) RHex: a 7 Kg, six-legged robot capable of dynamic running, stair-climbing, and a variety of biologically-inspired gaits [75]. (b) iSprawl: a 16 cm long six-legged runner with cable actuation driven by a single motor. iSprawl can run at speeds up to 15 body lengths per second [55]. (c) Mini-Whegs™: a wheel-leg hybrid quadruped that can jump and run 10 body lengths per second [67]. (d) DASH: a 16 g six-legged runner driven by a single motor, capable of running at 15 body lengths per second and withstanding impacts at its terminal velocity [15].

sources to drive prismatic legs that are attached to the hips with compliant, viscoelastic hinges that helped to stabilize the robot motion by providing tuned damping. Because of the pneumatic actuation, Sprawlita has not been able to run autonomously. However, a later Sprawl family robot based on very similar kinematics, iSprawl (shown in Fig. 2.8b), is capable of autonomous locomotion as it uses a single DC motor to drive all six legs through a slider crank mechanism connected to push-pull cables that operate the prismatic legs [55]. The key insight of iSprawl was the introduction of series compliance to the leg design that enabled it to go from running 5 body lengths per second to running 15 body lengths per second.

The most recent addition to the current lot of biologically inspired six-legged running robots is from UC Berkeley. At just 16 g, and 10 cm long, the Dynamic Autonomous Sprawled Hexapod (DASH) [15] shown in Fig. 2.8d is one of the lightest and fastest legged robots for its size. It's fabricated using the scaled SCM process [44], is driven by a single DC motor, and is capable of speeds up to 15 body lengths, or 1.5 m per second. It's unique design and construction also enable it to withstand impacts at its terminal velocity.

Part II

Design Principles and Tools for Folded Millirobots

Chapter 3

A Strain Energy-Based Fitness Metric for Compliant Mechanism Designs

Compliant mechanisms are a useful class of mechanisms because they attain their mobility from the elastic deformation of compliant members. The term "compliant mechanism" has been broadly used in the literature to describe both continuum mechanisms in which large scale deformation can be distributed throughout the body [98] [86] and so-called discrete or lumped compliance models in which compliance is concentrated at nodes which connect members that are generally assumed to be rigid [48] [47]. Because they have no mechanical parts whose surfaces move with respect to each other, they are free from backlash and friction and require no lubrication, making them advantageous for use at the microscale. These advantages have led to their adoption in a variety of robotic applications from microscale silicon-based robots [28] [43], to high resolution mesoscale precision positioning devices [11] [24], to milliscale mobile robots with microscale feature sizes [89] [45] as well as the scaled prototypes discussed in the previous chapter.

3.1 Fabrication of Millirobotic Compliant Mechanisms

3.1.1 SCM - Smart Composite Microstructures

Robot fabrication at the millimeter scale is inherently difficult with conventional mechanical components like continuous revolute joints, bearings, and motors because as component size is reduced, surface forces begin to dominate Newtonian forces [87]. Some MEMS research has been successful in creating robotic mechanisms like hinged joints [70], folded structures [97], and mobile microrobots [28][43][13]. However, MEMS processes require an expensive infrastructure,

are restricted to a specific set of materials compatible with existing microfabrication processes, and the design cycle can be very long.

SCM was designed expressly for the fabrication of milli-scale articulated components with micro-scale features. It's a process that integrates laser micromachined composite fiber laminates with polymer films to create mechanisms consisting of rigid composite links and compliant polymer hinges as shown in Fig. 3.2. The process as it has been implemented for the fabrication of previous robots in the Biomimetic Millisystems Lab is shown in Fig. 3.1 and the steps are outlined below.

1. The process begins with a sheet of uncured, pre-impregnated composite fiber laminate.
2. Gaps are laser micro-machined into the composite fiber.
3. A polymer film (typically polyimide) is then placed on top of the laminate.
4. The polymer sheet is cured to the composite fiber.
5. The cured composite and polymer are released and aligned onto another composite fiber layer.
6. The parts are cured.
7. The resulting flat structure is released.

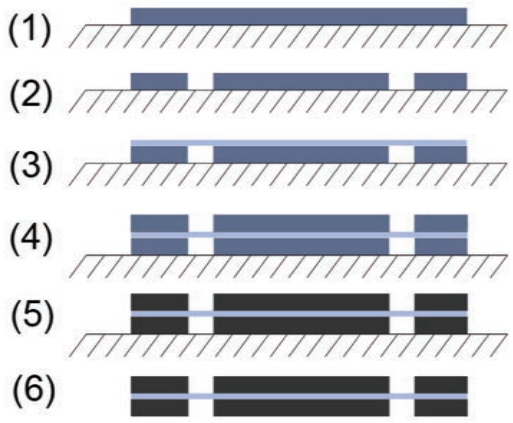

Figure 3.1: A step-by-step illustration of the SCM link and hinge fabrication process as implemented in the fabrication of the Berkeley micromechanical flying insect (MFI).

Fig. 3.2 is an illustration of a flexure hinge created using the SCM process. A layer of polymer film sandwiched between two cured sheets of carbon fiber provide a large range-of-motion compliant flexural joint that is devoid of friction and backlash and as a result does not wear. Entire

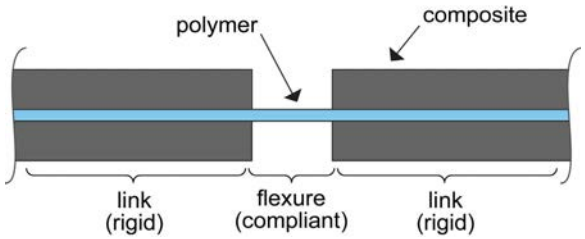

Figure 3.2: Schematic illustration of an SCM flexure hinge

structures consisting of rigid joints as well as flexible joints can be fabricated in this fashion. The structure can be folded from its flat position into a fully 3D structure - flexure hinges can be glued in place to form permanent rigid joints or left free to serve as compliant hinges for motion transmission as the design requires. The process has the advantages that an entire articulated robotic structure can be fabricated in a single flat "piece," and, unlike MEMS technology, it can quickly and easily produce truly 3D structures.

3.1.2 Existing Approaches to Modeling SCM Mechanisms

The most typical approach to modeling of compliant mechanisms is the finite element method (FEM) in which the body is subdivided into mesh elements and a large system of equations relating the tractions to the displacements for each elastic element are solved numerically. This method can be very powerful for optimizing or predicting the behavior of an existing topology [41], but its complexity and lack of analytical predictive power make it a cumbersome tool to apply during initial design or prototyping stages.

3.1.3 The Pseudo-Rigid-Body model

In the early stages of prototyping, designs tend to change very quickly, making time-consuming finite element analysis infeasible. At theses stages, to simplify the design process and provide a closed form approximation for the behavior of loaded flexures it is helpful to employ an approximate model of flexure stiffness. One such model that is useful for this purpose is the pseudo-rigid-body model (PRBM). The PRBM enables a mechanism designer to replace a continuum model of a flexural element with a lumped parameter model consisting of two rigid links connected by a linear torsional spring at some distance along the length of the original element as depicted in Fig. 3.3.

If the flexural element connects two comparatively rigid bodies and can be considered "small-length," it's possible to reduce the flexure joint to an ideal pin joint connecting the two rigid mem-

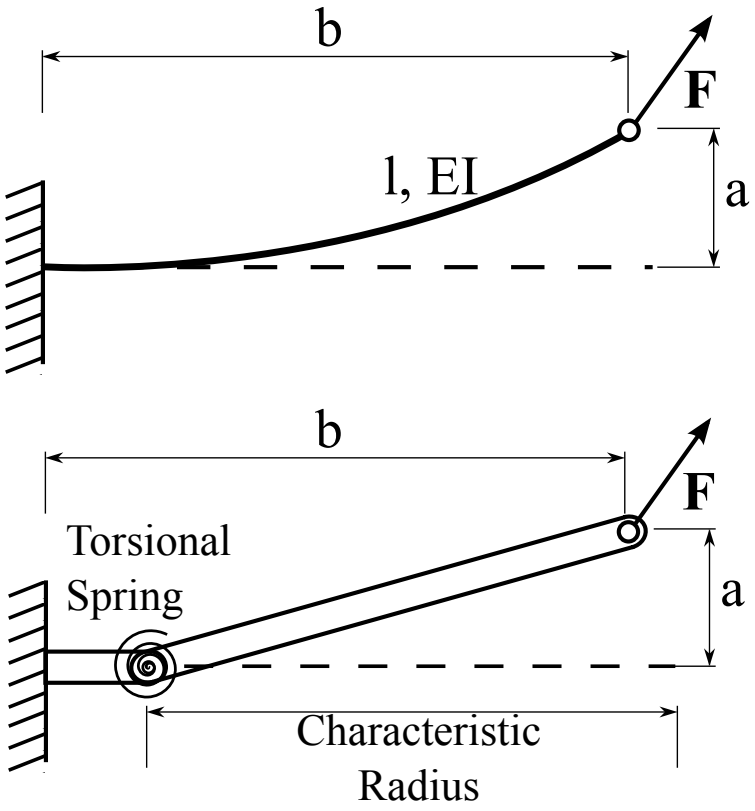

Figure 3.3: (a) Continuum and (b) Pseudo-Rigid-Body models of a beam flexure

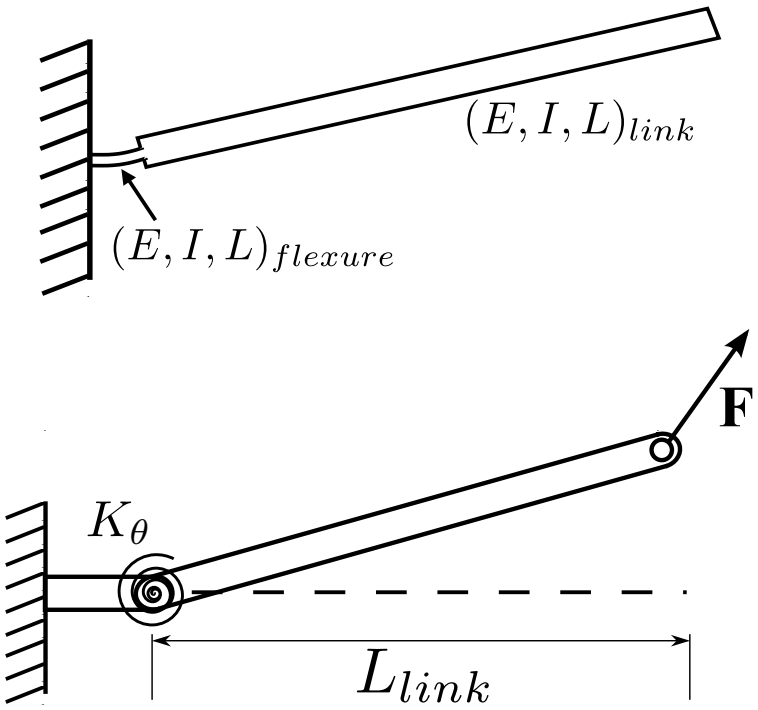

Figure 3.4: (a) Continuum and (b) Pseudo-Rigid-Body models of a small length flexure arrangement

bers in parallel with a linear torsional spring as shown in Fig. 3.4. More specifically, [47] defines flexure pivots as "small-length" if they meet the following criteria:

$$L_{link} >> L_{flexure} \tag{3.1}$$

$$(EI)_{flexure} << (EI)_{link} \tag{3.2}$$

In Eqn. 3.1 L_{link} is the length of a comparatively rigid link to which one end of the flexure is attached, and in Eqn. 3.2 the flexural stiffness, $(EI)_{link}$ is the flexural stiffness of that link. Characteristic link dimensions in millirobots are on the order of multiple millimeters while flexure lengths are typically 100-200μm, so this requirement is generally satisfied by the designs we are interested in creating. If a flexure can be considered small length, the expression for its rotational stiffness is reduced to the following:

$$K_\theta = \frac{EI}{L} \tag{3.3}$$

In Eqn. 3.3, E is the flexural modulus of the material from which the flexure hinge is constructed, I is the area moment of inertia, and L is the length of the flexure. This approximation is very useful in the early stages of design because it enables the designer to quickly estimate forces

and torques for a given mechanism design. However, because the model is planar and accounts for only a single degree of freedom, it cannot give any useful information regarding mechanism behavior in the presence of off-axis loads. This limitation has motivated the analysis in the rest of this chapter wherein SCM mechanisms are treated as spatial mechanisms which are designed to produce desired degrees of freedom as well as degrees of *constraint*.

3.1.4 Limitations of the PRBM

The PRBM was developed in an effort to simplify the compliant mechanism design process and bridge the gap between rigid mechanism design and compliant mechanism design. Most of the time, the PRBM is sufficient to model and analyze flexure mechanisms, and has been used with success in a variety of applications such as compliant robot leg design [34]. However, in practice, in our complicated kinematic designs, flexures experience loading and the consequent displacements in as many six axes. For larger scale devices or mechanisms where the applied and reaction loads are consistent and predictable this limitation of the PRBM may not be significant. But, for small scale mechanisms incorporated into millirobots where actuation involves the amplification of small strains or actuator output motions [94], the consideration of additional off-axis loads and displacements becomes increasingly important for avoiding the loss of actuator displacement to serial compliance in the structure. Put another way, our compliant mechanisms are designed to provide degrees of *freedom* and degrees of *constraint*. We desire that the mechanisms are most mobile in the directions enabled by their degrees of freedom and least mobile in the constrained directions determined by their degrees of constraint.

In cases where we are willing to assume small deflections, we may explicitly incorporate these multi-axis effects (in closed form) into our model in order to better study the off-axis behavior of a mechanism. In this chapter, we address the problem of improving the design of a single degree of freedom (DOF) compliant mechanism consisting of rigid links connected by simple flat flexure hinges experiencing small deflections. Specifically, we are interested in improving the various off-axis stiffnesses of such mechanisms while preserving the output motion in the desired direction. The example mechanism to which we apply our analysis here is the compliant version of a simple 1 DOF exact straight line linkage (shown in Fig. 3.8) known as the Sarrus linkage after its inventor, French mathematician Pierre Frédéric Sarrus.

3.2 Preliminaries

3.2.1 Rigid Transformations in 3-Space

Rigid motions in space can be represented as screws, or translations along a line plus a rotation about that line. A screw, $\mathbf{s}^\mathsf{T} = [\omega, \mathbf{v}]$, is an element of the Lie algebra of $SE(3)$. As such, it is transformed actively by the action of an element from the adjoint representation of the group:

$$\mathbf{s}' = Ad(g)\mathbf{s} \tag{3.4}$$

where $Ad(g)$ is a 6x6 matrix with the following form:

$$Ad(g) = \begin{bmatrix} \mathbf{R} & \mathbf{0} \\ \mathbf{SR} & \mathbf{R} \end{bmatrix} \tag{3.5}$$

For the remainder of this chapter we'll refer to this rigid transformation as $\mathbf{T}$. Further decomposing $\mathbf{T}$ enables us to write it as:

$$\mathbf{T} = \begin{bmatrix} \mathbf{I} & \mathbf{0} \\ \mathbf{S(r)} & \mathbf{I} \end{bmatrix} \cdot \begin{bmatrix} \mathbf{R} & \mathbf{0} \\ \mathbf{0} & \mathbf{R} \end{bmatrix} \tag{3.6}$$

In Eqn. 3.6, the matrix $\mathbf{S(r)}$ is the cross-product matrix defined as follows:

$$\mathbf{S(r)} = \begin{bmatrix} 0 & -r_z & r_y \\ r_z & 0 & -r_x \\ -r_y & r_x & 0 \end{bmatrix} \tag{3.7}$$

So, we see that $\mathbf{R}$ is the rotation matrix that defines the portion of the transform that consists of a rotation of the screw, and $\mathbf{S}$ accounts for the translation portion of the transformation with $\mathbf{r}$ being the vector from the initial position of the rigid body to its transformed position. The active transformation also has a corresponding passive change of coordinates that's given by the inverse of the transformation:

$$\bar{\mathbf{s}} = \mathbf{T}^{-1}\mathbf{s} = \begin{bmatrix} \mathbf{R}^\mathsf{T} & \mathbf{0} \\ -\mathbf{R}^\mathsf{T}\mathbf{S} & \mathbf{R}^\mathsf{T} \end{bmatrix} \begin{bmatrix} \omega \\ \mathbf{v} \end{bmatrix} \tag{3.8}$$

3.2.2 Wrenches

A wrench can be thought of as a generalized force. It generalizes forces and moments in the same way the screw generalizes translations and rotations into a six-dimensional vector. Wrenches

are elements of the dual to the Lie Algebra and so transform according to the inverse transpose of $\mathbf{T}$:

$$\overline{\mathbf{w}} = \mathbf{T}^{-\mathsf{T}}\mathbf{w} = \begin{bmatrix} \mathbf{R} & \mathbf{SR} \\ \mathbf{0} & \mathbf{R} \end{bmatrix} \begin{bmatrix} \mathbf{M} \\ \mathbf{f} \end{bmatrix} \tag{3.9}$$

3.2.3 Transformation of the Compliance Matrix

The compliance matrix of a body is a generalization of the concept of one-dimensional compliance into multiple dimensions. The compliance matrix relates applied forces and moments (wrenches) to linear and angular displacements (screws). More precisely, the compliance matrix is a linear operator that transforms wrenches into screws. In this chapter we will use rigid coordinate transformations of the compliance matrix extensively, so we note that combining Eqns. 3.8 and 3.9 yields the equation determining how the compliance matrix transforms under a coordinate change:

$$\overline{\mathbf{C}} = \mathbf{T}^{-1}\mathbf{C}\mathbf{T}^{-\mathsf{T}} \tag{3.10}$$

3.3 Modeling Mechanism Stiffness

In this section, we derive the expression for the compliance matrix of a beam by first starting from a small beam element. This derivation was done in [79], but it is repeated here for completeness. Then, using the compliance matrix resulting from that derivation, we describe a process for referring the compliance matrix of each flexure in an SCM mechanism to a common coordinate system. This compliance transformation will enable us to express an "equivalent" mechanism compliance in a common output coordinate system. The focus on a rectangular cross-section beam of uniform thickness is motivated by the compliant structures we are currently capable of producing using the SCM process.

3.3.1 Compliance of a Small Beam Element

Fig. 3.5 shows a small element from a beam subjected to a wrench, $\mathbf{w}$. The beam element is assumed to be in equilibrium. The beam element has a finite compliance that transforms the applied wrench into a screw displacement expressed as the difference of two screws:

$$\mathbf{C}\mathbf{w} = \Delta\mathbf{s} \tag{3.11}$$

In Eqn. 3.11 $\mathbf{C}$ is the compliance matrix for the small beam element. In this analysis we will assume small deflections, so that $\Delta\mu \approx \Delta s$ where s is the arc length of the beam. This is the

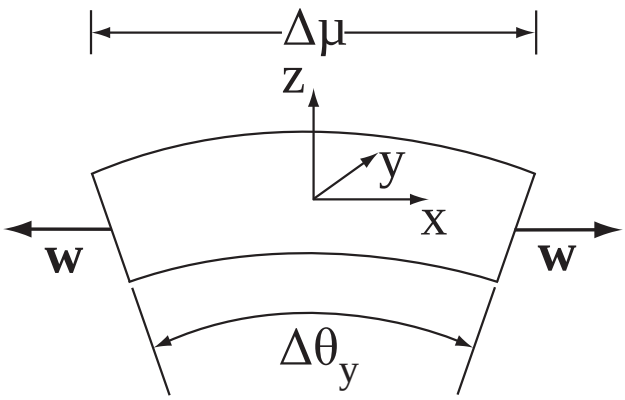

Figure 3.5: A small element in a beam subjected to a wrench, $\mathbf{w}$.

same assumption that enables curvature to be approximated as $\frac{\partial^2 y}{\partial x^2}$ in the classic analysis of a beam proceeding directly from the Euler-Bernoulli equation. Additionally, we assume that cross-sections of the beam remain perpendicular to the neutral axis even in the deformed state.

Starting with the axial force component of the wrench, we have the following relation describing the displacement of the beam due to an applied force along the beam axis:

$$F_x \left(\frac{1}{EA} \right) = \frac{\Delta x}{\Delta \mu} \tag{3.12}$$

Where E is the modulus of the material and A is the cross sectional area of the beam element.

For a moment about the x axis, the angular displacement is dependent on the size and shape of the cross section. Here we are only considering a beam with a rectangular cross section of constant thickness. However, an approximate expression relating the moment about the x axis and the angular displacement in the $y - z$ plane is:

$$M_x \left(\frac{1}{\alpha G} \right) \approx \frac{\Delta \theta_x}{\Delta \mu} \tag{3.13}$$

where α is a function of the geometry of the cross-sectional area. Formulas for α for a rectangular cross-section beam can be found in [35].

A moment applied about the y axis results in pure bending of the beam element and gives the familiar equation:

$$M_y \frac{1}{EI_z} = \frac{\Delta \theta_y}{\Delta \mu} \tag{3.14}$$

where I_z is the area moment of inertia defined for the beam geometry shown in Fig. 3.6 as $bh^3/12$.

Similarly, a moment applied about the z axis also results in pure bending:

$$M_z \frac{1}{EI_y} = \frac{\Delta\theta_z}{\Delta\mu} \tag{3.15}$$

where I_y is the area moment of inertia about the y axis: $b^3h/12$.

We choose to neglect the effect of shear in the beam, so displacements due to forces in the y and z directions are ignored.

Assembling Eqns. 3.12 - 3.15 into matrix form gives the following:

$$c \begin{bmatrix} M_x \\ M_y \\ M_z \\ F_x \\ F_y \\ F_z \end{bmatrix} = \frac{1}{\Delta\mu} \begin{bmatrix} \Delta\theta_x \\ \Delta\theta_y \\ \Delta\theta_z \\ \Delta x \\ \Delta y \\ \Delta z \end{bmatrix} \tag{3.16}$$

In Eqn. 3.16 c can be considered a compliance per length, $\Delta\mu$.

3.3.2 Compliance Matrix of a Linear Beam

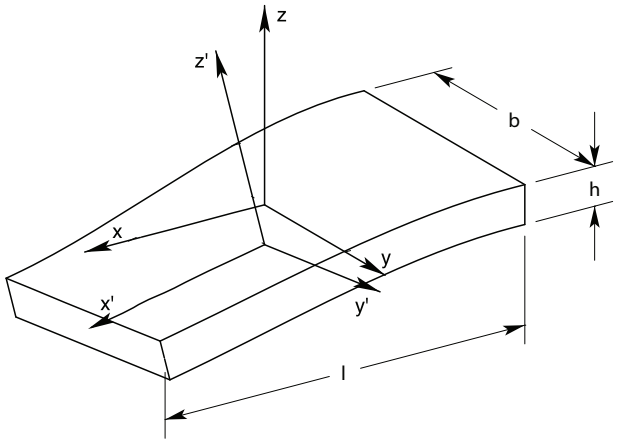

Figure 3.6: From [39]: A flat flexure depicting local coordinate systems before $(\mathbf{x}, \mathbf{y}, \mathbf{z})$ and after $(\mathbf{x}', \mathbf{y}', \mathbf{z}')$ deformation. This choice of local coordinate system diagonalizes the compliance matrix.

We can now use Eqn. 3.16 to compute the compliance matrix for an entire beam. First, however, because c is expressed in a local coordinate frame (located at the center of the element), we must first transform it to a common coordinate system for the entire beam before we can sum the individual compliance matrices for the differential elements. We parameterize the distance along

the x axis from the fixed base of the beam by μ. How we express the location of the coordinate system for each differential element of the beam will depend on our choice of common coordinate system in which to express the whole beam compliance. We choose to take the location of the origin of our common coordinate system to be located at half the length of the beam, or $\frac{l}{2}$. The reason for our choice of coordinate system will become clear later.

The location of the origin of each coordinate system local to the differential beam elements is given by μ, meaning we must translate the local coordinate system for each beam element by a distance $\frac{l}{2} - \mu$. To do this we construct the following transformation matrix using Eqns. 3.6 and 3.7:

$$\mathbf{T^{-1}} = \begin{bmatrix} 1 & 0 & 0 & 0 & 0 & 0 \\ 0 & 1 & 0 & 0 & 0 & 0 \\ 0 & 0 & 1 & 0 & 0 & 0 \\ 0 & 0 & 0 & 1 & 0 & 0 \\ 0 & 0 & \frac{l}{2} - \mu & 0 & 1 & 0 \\ 0 & -\frac{l}{2} + \mu & 0 & 0 & 0 & 1 \end{bmatrix} \tag{3.17}$$

Combining Eqns. 3.17 and 3.10 generates the following expression for the compliance matrix of the beam as a function of the distance, μ, along the beam:

$$c(\mu) = \begin{bmatrix} \frac{1}{G\alpha} & 0 & 0 & 0 & 0 & 0 \\ 0 & \frac{1}{EI_z} & 0 & 0 & 0 & \frac{\mu - \frac{l}{2}}{EI_z} \\ 0 & 0 & \frac{1}{EI_y} & 0 & \frac{l-2\mu}{2EI_y} & 0 \\ 0 & 0 & 0 & \frac{1}{AE} & 0 & 0 \\ 0 & 0 & \frac{l-2\mu}{2EI_y} & 0 & \frac{(l-2\mu)^2}{4EI_y} & 0 \\ 0 & \frac{\mu - \frac{l}{2}}{EI_z} & 0 & 0 & 0 & \frac{\left(\mu - \frac{l}{2}\right)^2}{EI_z} \end{bmatrix} \tag{3.18}$$

Integration of Eqn. 3.18 with respect to μ on the interval $[0, l]$ reveals the reason for our choice of origin location for the common coordinate system at $\frac{l}{2}$:

$$\begin{bmatrix} \frac{l}{G\alpha} & 0 & 0 & 0 & 0 & 0 \\ 0 & \frac{l}{EI_z} & 0 & 0 & 0 & 0 \\ 0 & 0 & \frac{l}{EI_y} & 0 & 0 & 0 \\ 0 & 0 & 0 & \frac{l}{AE} & 0 & 0 \\ 0 & 0 & 0 & 0 & \frac{l^3}{12EI_y} & 0 \\ 0 & 0 & 0 & 0 & 0 & \frac{l^3}{12EI_z} \end{bmatrix} \tag{3.19}$$

Clearly, our choice of common coordinate system for the compliance of the beam diagonalizes the compliance matrix. This result agrees with the results in [88] and [29]. However, to further verify the compliance matrix, we can take the common coordinate reference to be located at the

end of the beam. Elements $\mathbf{T_{54}}$ and $\mathbf{T_{62}}$ in Eqn. 3.17 are replaced by $l-\mu$ and -$l+\mu$ respectively. Eqn. 3.18 becomes:

$$c(\mu) = \begin{bmatrix} \frac{1}{G\alpha} & 0 & 0 & 0 & 0 & 0 \\ 0 & \frac{1}{EI_z} & 0 & 0 & 0 & \frac{\mu-l}{EI_z} \\ 0 & 0 & \frac{1}{EI_y} & 0 & \frac{l-\mu}{EI_y} & 0 \\ 0 & 0 & 0 & \frac{1}{AE} & 0 & 0 \\ 0 & 0 & \frac{l-\mu}{EI_y} & 0 & \frac{(l-\mu)^2}{EI_y} & 0 \\ 0 & \frac{\mu-l}{EI_z} & 0 & 0 & 0 & \frac{(l-\mu)^2}{EI_z} \end{bmatrix} \tag{3.20}$$

Integrating 3.20 on the interval $[0, l]$ yields the familiar compliance matrix for a beam in which the cross-coupling between moments and forces applied at the end of the beam is apparent in the off-diagonal terms of $\mathbf{C}$:

$$\mathbf{C} = \begin{bmatrix} \frac{l}{G\alpha} & 0 & 0 & 0 & 0 & 0 \\ 0 & \frac{l}{EI_z} & 0 & 0 & 0 & -\frac{l^2}{2EI_z} \\ 0 & 0 & \frac{l}{EI_y} & 0 & \frac{l^2}{2EI_y} & 0 \\ 0 & 0 & 0 & \frac{l}{AE} & 0 & 0 \\ 0 & 0 & \frac{l^2}{2EI_y} & 0 & \frac{l^3}{3EI_y} & 0 \\ 0 & -\frac{l^2}{2EI_z} & 0 & 0 & 0 & \frac{l^3}{3EI_z} \end{bmatrix} \tag{3.21}$$

Finally, we note that the above formulation only considers deformation due to bending, torsion, and axial extension - we have not considered shear forces or applied axial loads. A formulation of the diagonal compliance matrix that includes terms representing these effects was presented in [46].

3.3.3 Compliance Transformation for Individual Flexures

Eqn. 3.19 describes the compliance properties of a single flexure, but the mechanisms in which we are interested are typically comprised of multiple flexures connecting sets of rigid links in both serial and parallel configurations. In order to analyze the stiffness properties of an entire mechanism, we must combine the flexure compliance matrix with knowledge of mechanism geometry to generate an equivalent *mechanism* compliance. Just as we did with individual small beam elements to construct a compliance matrix for the beam, this is begun by transforming the flexure compliance in the local coordinate frame into the output coordinate frame of the mechanism.

In general, for any system of springs, elements in parallel are those that experience the same displacement and their stiffnesses can therefore be added to create an equivalent stiffness. Elements in series experience the same load - their compliances add to create a single equivalent compliance. However, this combination is only possible when the stiffnesses or compliances to be added are expressed in a common coordinate system. Therefore, we require that the compliance matrix in (3.19) for each flexure in the mechanism be transformed to a common coordinate system.

This transformation refers the compliance of each flexure joint to the base coordinate system (usually attached to the output platform or link of a parallel mechanism), and, in general, will depend on the position and orientation of each flexure relative to the chosen base coordinate system. While the compliance matrix of each flexure explicitly represents a general six axis spring, the spatial transformation introduces the mechanism geometry into the computation of the overall compliance of the mechanism.

Here, again, we use 6x6 transformation matrix in Eqn. 3.5 to transform the compliance of an individual flexure in the local coordinate system to the common coordinate system chosen to be at the output of the mechanism. For each flexure in a parallel flexure mechanism the matrices $\mathbf{S}$ and $\mathbf{R}$ will be functions of the mechanism geometry. For each flexure, we formulate $\mathbf{S}$ and $\mathbf{R}$ matrices and apply the tranformation in Eqn. 3.10 in order to express the compliance matrix in a common coordinate system. The resulting compliance matrix for the whole mechanism, $\mathbf{C_0}$ is the result:

$$\mathbf{C_0} = \sum_i \mathbf{T_{0/i}}^{-\mathsf{T}} \mathbf{C_i} \mathbf{T_{0/i}}^{-1} \tag{3.22}$$

In Eqn. 3.22, $\mathbf{C_i}$ is the compliance matrix of the i^{th} flexure in the mechanism and $\mathbf{T_{0/i}}$ is the transformation from the i^{th} coordinate frame to the output coordinate frame of the mechanism.

3.4 Application to Compliant Mechanism Design

Using the above formulation, we would like to analyze compliant mechanism designs that result from using the SCM process. In addition to the constraints imposed by the limits of the SCM fabrication process, mobile millirobot design is highly constrained by the size and mass of the electronics and power source needed to power and control actuators. As such, current and past robot designs [96] [45] have made extensive use of parallel kinematics in order to appropriately couple and control the desired degrees of freedom while minimizing the number of required actuators.

3.4.1 An Energy-Based Design Metric

With these considerations in mind, we aim to design a compliant mechanism that exhibits maximal compliance in the desired degrees of freedom and maximal stiffness in the undesired degrees of freedom. In order to compare the performance of different designs, it is therefore necessary to adopt a metric by which to judge a mechanism. In this work, we use the ratio of the so-called "mutual potential energy" [80] (also sometimes referred to as "mutual strain energy") to the total strain energy of the mechanism:

$$f = \frac{\text{MPE}}{\text{SE}} \tag{3.23}$$

The mutual potential energy is defined as:

$$\text{MPE} = \mathbf{v}^{\mathsf{T}}\mathbf{K}\mathbf{u} \tag{3.24}$$

where $\mathbf{v}$ is the displacement vector at the output when only a unit dummy load is applied in the desired output direction, $\mathbf{K}$ is the equivalent stiffness of the mechanism expressed in the base or output coordinate system, and $\mathbf{u}$ is the displacement vector when the entire input load is applied. Intuitively, we can think of mutual potential energy as the amount of useful work or displacement generated at the output port by an input load. The strain energy of the mechanism is given by:

$$\text{SE} = \frac{1}{2}\mathbf{u}^{\mathsf{T}}\mathbf{K}\mathbf{u} \tag{3.25}$$

Thus, the performance metric given in Eqn. 3.23 is a ratio of the work output in the desired direction (the useful work) to the work done in deforming the mechanism. The larger this ratio, the more "efficient" the mechanism can be considered, ie. the undesirable degrees of freedom remain stiff while the desirable degrees of freedom are compliant.

3.4.2 Design Evaluation and Analysis

SCM robots' highly constrained mechanical and kinematic requirements often lead to mechanically complex designs. As a simple example of the usefulness of modeling the full compliance of these SCM structures, we focus on the design of a mechanism that plays a prominent role in the robot described in Chapter 4, the Sarrus linkage. Fig. 3.7 shows a model of the robot in which a central Sarrus linkage (shown in blue) can been seen connecting two sets of three hips such that when it contracts the upper legs are adducted while the lower legs are abducted. The Sarrus' central role in this compliant robotic structure and the complex loads that are applied at the hips as a result of ground reaction forces transferred through the legs make it an interesting case study.

Before proceeding with our analysis it is important to note the distinction between topology and geometry as we use the terms here. A mechanism topology refers to the number of links and joints and their connectedness. One can consider an abstraction of a linkage as a graph in which joints are represented by edges of the graph and links are represented as nodes. In this abstraction, the addition of a redundant kinematic chain to a mechanism clearly changes the topology of the linkage as well as its graph representation. Geometry, however, refers to the physical dimensions and configuration of the mechanism. It can include, for example, link lengths, angles between links, and in the case of compliant mechanisms, flexure dimensions.

The most common (and minimal) topology of the Sarrus linkage (as pictured in Fig. 3.8) consists of two planar kinematic chains of 4 links connected by three hinges. The two chains are rigidly connected at their base and outputs and are oriented at an angle (usually 90°) with respect to each other such that the rotation axes of all the joints intersect. Mobility of the chain as predicted

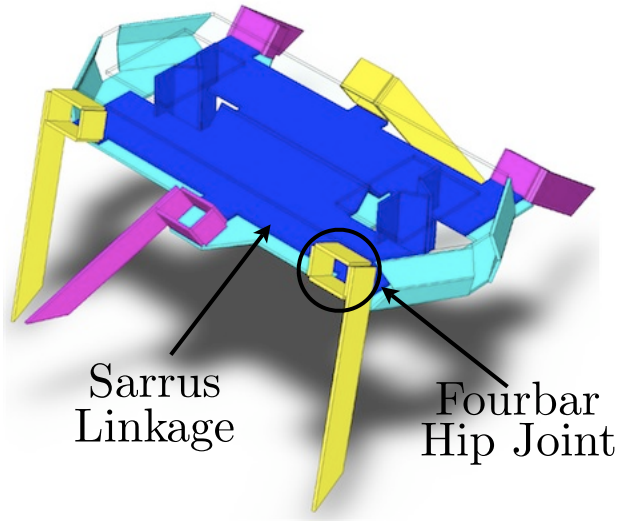

Figure 3.7: A CAD model of a hexapedal crawler that uses a Sarrus linkage to connect six fourbar hip joints.

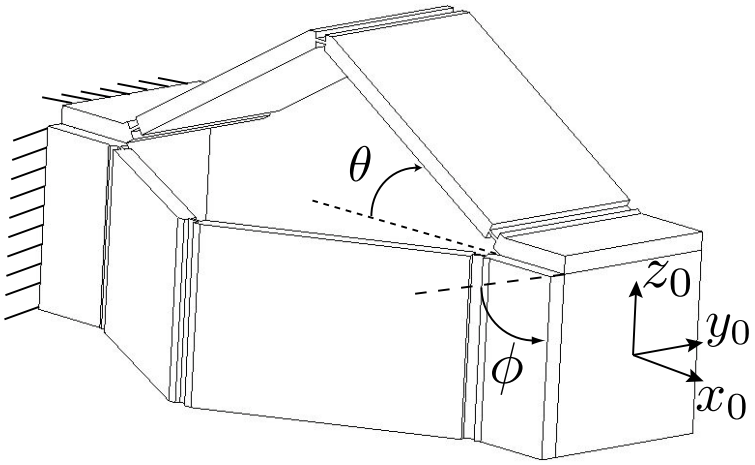

Figure 3.8: A compliant Sarrus linkage shown with its simplest topology and configuration: Two 4 link kinematic chains rigidly joined at their base and output links and oriented at ϕ = 90°to each other.

by Grübler's criterion is zero, so it's important that the rotation axes for the joints be precisely aligned.

Using conventional mechanical components, the Sarrus linkage would typically be constructed with pin-type hinges, which ideally provide infinite compliance in rotation about the hinge axis and infinite stiffness in all other directions. However, we are designing a compliant Sarrus linkage in which each hinge has finite compliance/stiffness. Given that fact, we are interested in the topologies and geometries of the Sarrus linkage which, for a given set of forces applied at the output, maximize the metric in (3.23).

The minimal topology for the compliant Sarrus consists of two serial kinematic chains connected at some angle, ϕ, with respect to each other. Conventional Sarrus linkage designs typically set $\phi = 90°$. In fact, for conventional designs with ideal hinges, any angle other than zero and 180° will provide equivalent exact straight line motion constraint. However, for the compliant case, the angle between the two kinematic chains becomes an important design variable when considered in tandem with loading conditions at the output frame. All cases considered below have the geometric parameter θ (depicted in Fig. 3.8) set to 30°. Additionally, the loading condition considered is the simultaneous application of forces (but no moments) in all three axes.

Case I: Two chain compliant Sarrus

This topology is shown in Fig. 3.8. We are interested in the angle between the two kinematic chains, ϕ that gives the best performance in the sense of Eqn. 3.23 for forces in the x_0, y_0, z_0 coordinate frame. Fig. 3.9 shows the performance of the two chain Sarrus for the range $\phi \in [0, \pi]$ for four different loading conditions. The parameter β represents the ratio of the magnitude of the two off-axis forces (taken to be equal in these examples) to the forces in the direction of highest compliance (the x_0 direction, in this case).

From the figure, we see that as the off-axis forces become large in comparison to the force in the compliant direction, a clear optimal orientation angle for the kinematic chains appears at approximately 0.85 radians.

Case II: Three chain compliant Sarrus

From a strictly kinematic perspective, the redundancy introduced by adding a third kinematic chain is unnecessary for the straight line constraint. However, from a compliance perspective, our design intuition is that redundancy should provide an improvement in mechanism performance. Fig. 3.10 shows that, in fact, we do see an improvement in performance. For the case of relatively small off-axis forces (β=0.5) maximum performance is unchanged. However, the mechanism shows a reduced sensitivity to an increase in β at the optimal orientation angle of ϕ = 0.85 radians. It's important to note, however, that this relative insensitivity to off-axis forces only occurs at the optimal orientation angle. Away from that angle, performance drops markedly with increased off-axis loading. Additionally, the peak performance predicted for this configuration oc-

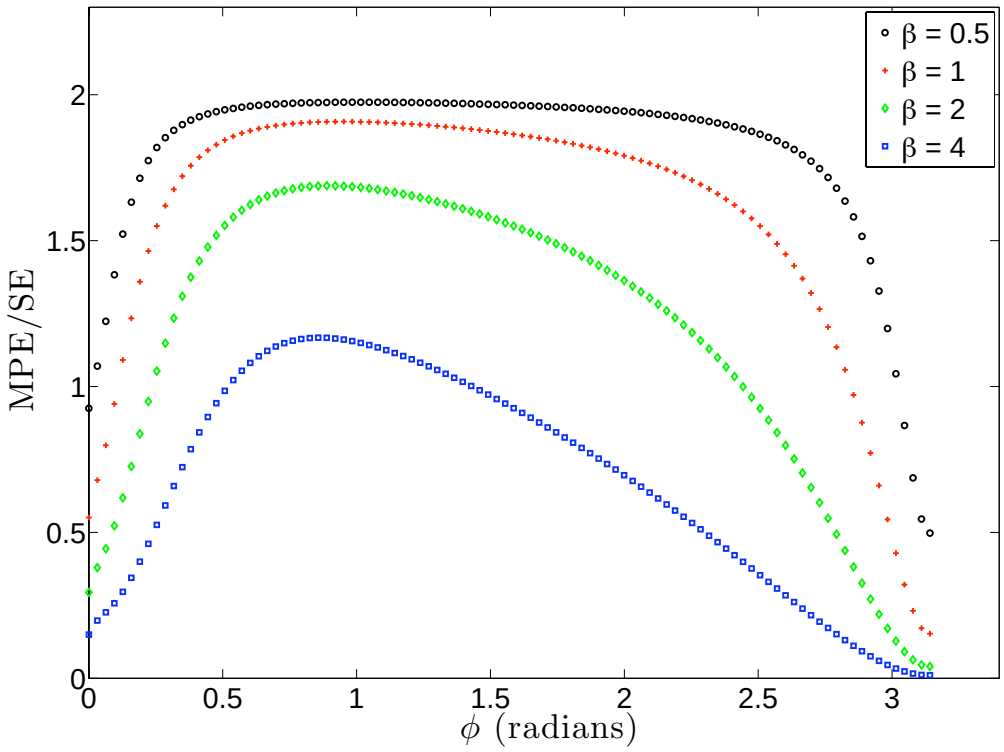

Figure 3.9: Performance of a Sarrus linkage consisting of two kinematic chains connected at an angle, ϕ. The parameter β is the ratio of the off-axis forces to the force in the direction of highest compliance.

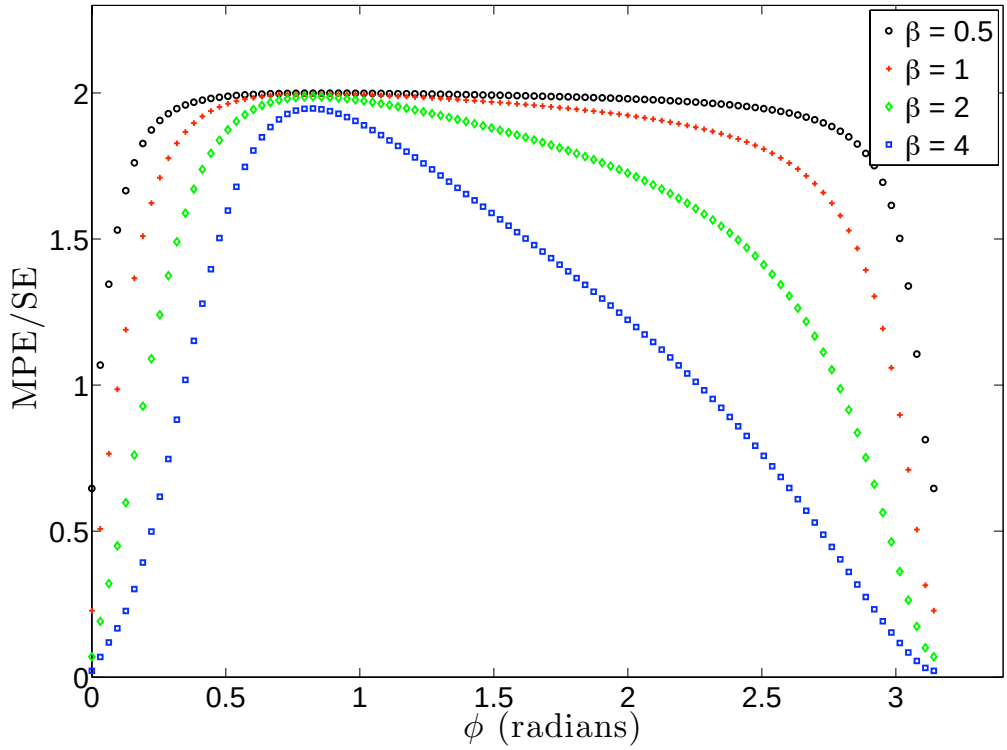

Figure 3.10: Performance variation in a Sarrus linkage comprised of three kinematic chains with two chains connected at angles of ϕ and -ϕ with respect to the third. β is the ratio of off-axis forces to forces in the most compliant direction.

curs to the left of the $\phi = \frac{\pi}{2}$ due to the asymmetric loading configuration. When the force in the y direction is removed, because of the symmetry of the topology and geometry of the mechanism, the peak performance occurs at the angle $\phi = \frac{\pi}{2}$.

Case III: Four chain compliant Sarrus

The geometry of this case corresponds to a mirroring of the geometry in case I about the plane $z = y$. Results from the analysis of this topology are shown in Fig. 3.11.

This topology shows the best performance in two senses. First, the maximal performance is relatively insensitive to the orientation angle of the chains (away from the singular $\phi = 0$ and $\phi = \pi$ orientations). Secondly, the performance of the mechanism is relatively insensitive to increases in the off-axis loads over that range of ϕ.

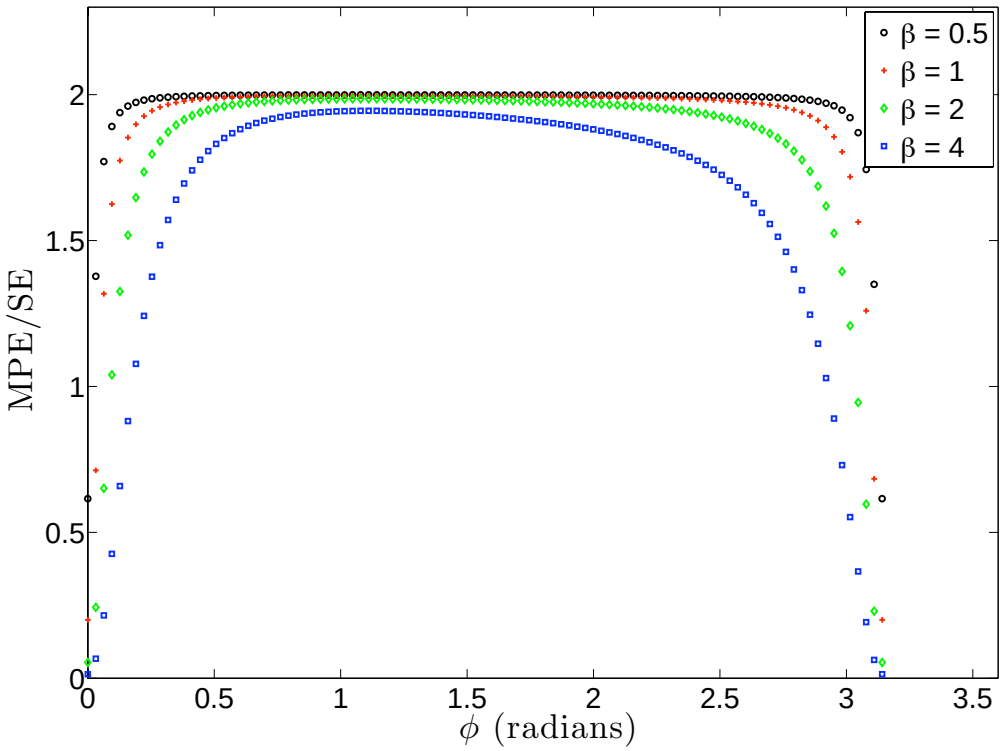

Figure 3.11: Performance variation in a Sarrus linkage comprised of four kinematic chains. This configuration shows the overall best performance encapsulated by a lack of sensitivity to off-axis forces (β) as well as orientation angle (ϕ).

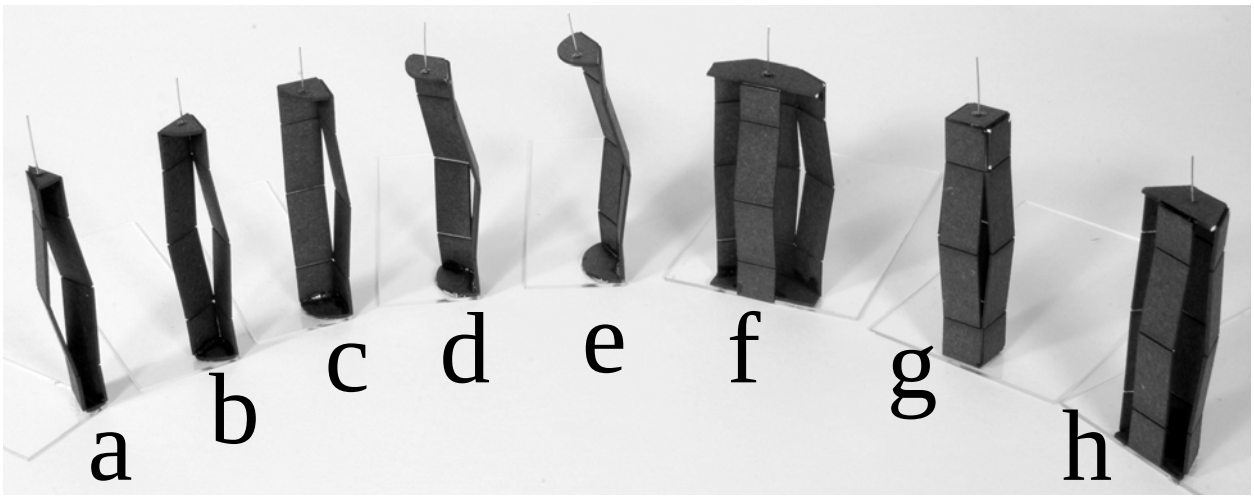

Figure 3.12: Sarrus linkage topologies and configurations used to experimentally verify the predictions of the model. **a-e** are the five configurations of the two chain topology **a**, ϕ = 30° up to **e**, ϕ = 150°. **f-h** represent the five configurations for the four chain topology. For **f**, ϕ = 30°(150°), **g**, ϕ = 90°, and **h**, ϕ=60°(120°). Only three linkage configurations are necessary for the four chain topology because the 120° and 150° orientations are reflections of the 60° and 30° orientations respectively.

3.5 Experimental Results

To test the predictions of model, we fabricated 5 different geometric configurations of two topologies of the Sarrus linkage - the two chain topology and the four chain topology. The mechanisms were constructed using the folding process described in [44] and Appendix A. Table I summarizes the common geometric parameters for all linkages tested.

The base of each linkage was grounded and a load was applied to the output link at the free end

Parameter	**Value**
b	8mm
h	50μm
l	600μm
l_{link}	20mm
θ	10°

Table 3.1: Sarrus linkage geometric parameters

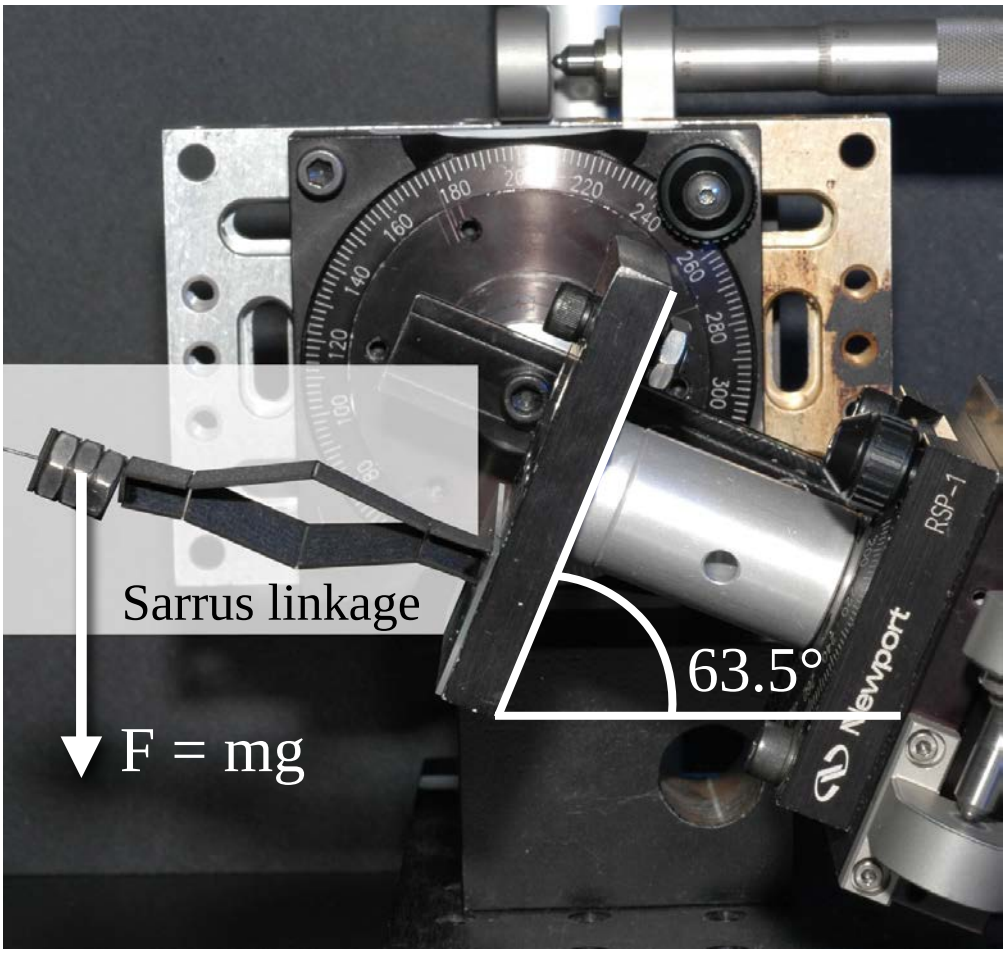

Figure 3.13: Experimental setup used to generate controlled off-axis loading for testing compliant Sarrus linkage performance.

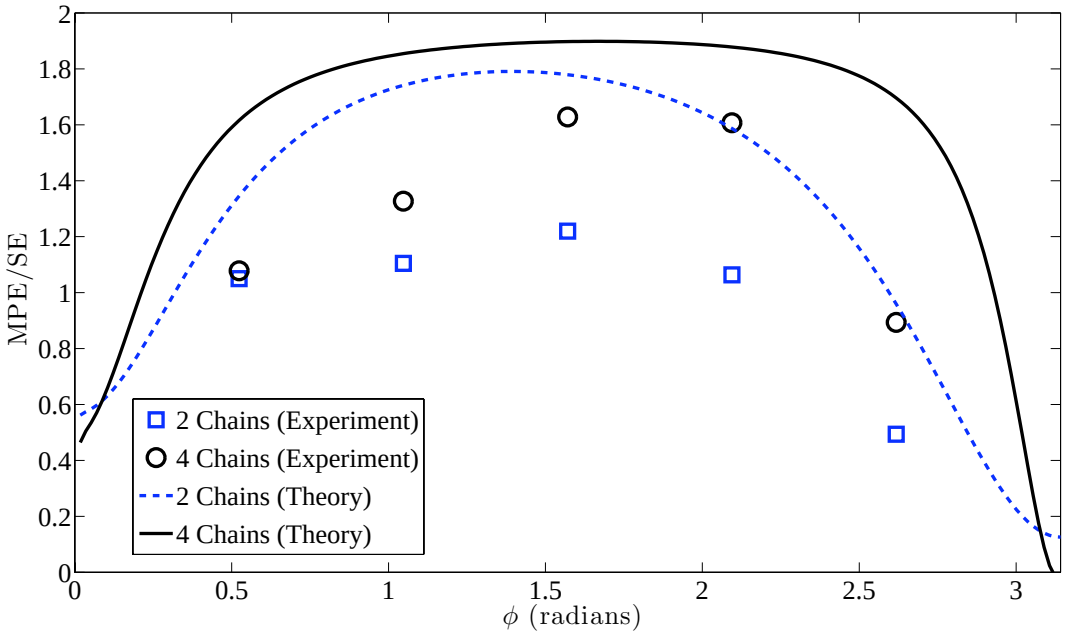

Figure 3.14: Comparison of theory to experimental measurements of two and four chain Sarrus linkages of varying geometries.

by a simple mass as depicted in Fig. 3.13. The entire linkage was rotated through several angles to create ratios of off-axis to on-axis loading, β, of 0-2. The linear and angular displacements in the XZ plane were measured optically, and the 3x3 stiffness matrix was estimated from the displacement data using the procedure outlined in [22]. Results comparing the performance of the two topologies are shown in Fig. 3.14.

For each topology 5 different configurations (orientation angles of the individual chains) were subjected to an off-axis force in the negative Z direction and a moment about the Y axis as well as an on-axis load in the negative X direction. Fig. 3.14 shows a comparison of the theoretical prediction for the mechanism performance to the experimental data. While the theory and experiment are not an exact match, both bear out the conclusion that the 4 chain Sarrus is preferable to the two chain topology and the peak performance, or maximal off-axis stiffness, for both occurs when the chains are oriented at $\frac{\pi}{2}$ radians or 90° to each other. The overprediction of the mechanism performance by the model could be due to the fact that the model does not account for types of loading other than bending and normal axial loads. More accurate results may be achievable by integrating, for example, the effect of shear forces.

3.6 Concluding Remarks

By transforming the stiffnesses of simple, constant cross section, beam-like flexures into a common coordinate system we can generate an expression for the generalized stiffness of a compliant mechanism consisting of rigid links interconnected by flat flexures. Using a strain energy-based metric, we can analyze the performance of a given topology and geometry subject to a prescribed set of loads at the output of the mechanism. In this work, this approach has been applied to understanding and improving the off-axis performance of a compliant linkage commonly used in the design of our millirobots - the exact straight line Sarrus linkage.

Using the tools described we demonstrated a quantifiable improvement in the performance of the compliant Sarrus linkage by adjusting only the linkage topology. However, we have not optimized in any formal, global sense the topology or geometry of the mechanism. Rather, we have applied a straightforward closed form model to assist in understanding mechanism behavior under general loading conditions. That ability to quickly predict performance improvements of these compliant linkages has the potential to provide additional insights at the early stages of design and reduce the overall design cycle time for SCM millirobots.

It is important to note, however, that the results of this approach are dependent not only on the mechanism topology and geometry, but also on the loading conditions imposed at the output of the mechanism. This dependence of the mechanism performance on the loading condition requires the mechanism designer to understand the nature of the output loads associated with the intended application. If those loads are well understood, this approach provides a useful tool for guiding the initial exploration of the design space. Once a promising design has been identified, more intensive approaches such as finite element modeling can be applied to improve the precision or performance of the design.

Part III

Legged Robot Designs and Experiments

Chapter 4

Design and Prototyping of RoACH, a 2.4 Gram Hexapedal Robot

In this chapter, we merge the areas of legged locomotion and millirobotic design to present the Robotic Autonomous Crawling Hexapod (RoACH) a 2.4 g legged millirobot capable of steerable locomotion. The robot makes use of the SCM process for its design and construction and of shape memory alloy wire actuators to provide the mechanical power for locomotion.

The design of the robot presented here progresses from a scaled, functional, kinematic prototype using the process described in Appendix A to a true-scale, fully capable untethered millirobot. The prototype is useful for verifying and quickly adjusting the kinematic design, after which point more thorough analysis is performed to complete the design at the milli-scale. This work represents the first step in applying the enabling technology of SCM to produce a fully functional, integrated, legged millirobot. As such, we focus primarily on the robot's mechanical design, the use of the SCM process, and the integration of the actuation, power, and control but do not present a dynamic system model or a control map. The primary contribution of this chapter is demonstrating the viability of legged machines at the milliscale through the integration of novel processes and technologies.

4.1 Prototyping the RoACH Hexapod

Because millirobot fabrication at scale can be a difficult and time-consuming process for the reasons listed in Section 1.1 of Chapter 1, and because our proposed design represents a major departure from previous legged robot designs in the Biomimetic Millisystems Lab [73], we have chosen to begin the design process with a 2× scaled prototype of the robot. This approach serves two purposes: 1) it enables us to verify that the scaled prototyping process in Appendix A works

as designed, and 2) it allows us to verify kinematic functionality before committing time and effort to milli-scale fabrication.

4.1.1 Kinematic Sketch

Here we will briefly describe a simple kinematic sketch of the scaled prototype of the robot, leaving the bulk of the analysis to be done in the portion of this chapter that deals with the milliscale design. Because the flexure joints that SCM relies on do not admit continuous rotation, it is impossible for the output of a single degree of freedom linkage to produce motion on a closed curve without experiencing a kinematic singularity or some kind of elastic instability such as snap-through buckling. However, effective locomotion that does not rely on stick-slip phenomena or vibrational excitation requires that a "foot" move on just such a closed trajectory. The implication of this limitation of SCM joints is that our kinematic design requires a minimum of two degrees of freedom to enable walking.

We would also like to implement a gait that provides static stability to the robot actively (when it's walking) and passively so that when all of the robot's actuators are switched off, it is still capable of standing. Looking to nature for biological inspiration reveals the simplest possible gait for a hexapod - the alternating tripod gait [4]. In this gait, the ipsilateral front and hind legs move in phase with the contralateral middle leg, and as long as the center of mass remains over the triangle of support formed by those three contacts, the robot is statically stable. A schematic depiction of the gait is shown in Fig. 4.1.

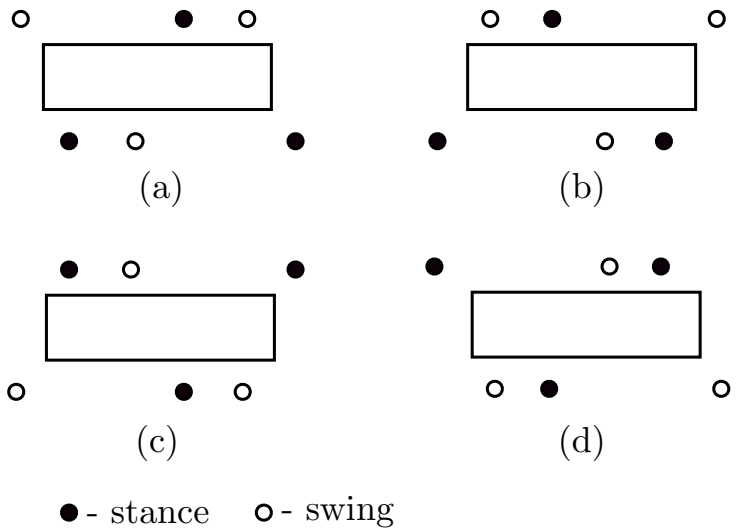

Figure 4.1: Diagram of the alternating tripod gait at four extreme positions

Fig. 4.2 depicts the kinematic concept for instantiating the two degrees of freedom required to move the foot on a closed trajectory and coupling them appropriately to six legs to create the

Position	Actuator 1	Actuator 2
a	OFF	OFF
b	ON	OFF
c	ON	ON
d	OFF	ON

Table 4.1: Map of actuator states to gait positions shown in Fig. 4.1

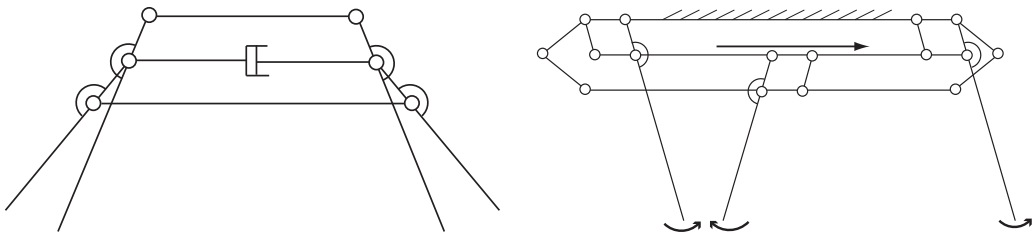

(a) First degree of freedom - abduction and adduction (rear view)

(b) Second degree of freedom - protraction and retraction (side view)

Figure 4.2: Prototype crawler kinematics showing two independent degrees of freedom

alternating tripod gait depicted in Fig. 4.1. The concept sketch makes use of parallel kinematics to appropriately couple the legs and generate an alternating tripod gait using just two actuated degrees of freedom.

4.1.2 Prototype Fabrication

A 2X scale prototype of the robot based on the kinematic sketch above was fabricated according the process described in Appendix A. The progression from flat component parts to the folded robot skeleton is shown in Fig. 4.3.

There are three primary pieces in the robot prototype design, and they are pictured in Fig. 4.3a. The two similar looking plates are the top and bottom plates of the robot prototype. Each includes the links necessary for folding up three fourbars which altogether form the six hips. Once assembled, each hip is connected to its respective plate (top or bottom) and the middle plate. The hip joint is designed for two degrees of freedom. The first of these degrees of freedom is the rotation of the links of the parallel fourbar. With the leg attached, these are the protraction and retraction motions of the leg shown schematically in Fig. 4.2a. The other degree of freedom comes from the fact that the hips of the upper (lower) tripod combined with the middle and upper (lower) plate also form a fourbar linkage. When the middle plate contracts, the hips connected to

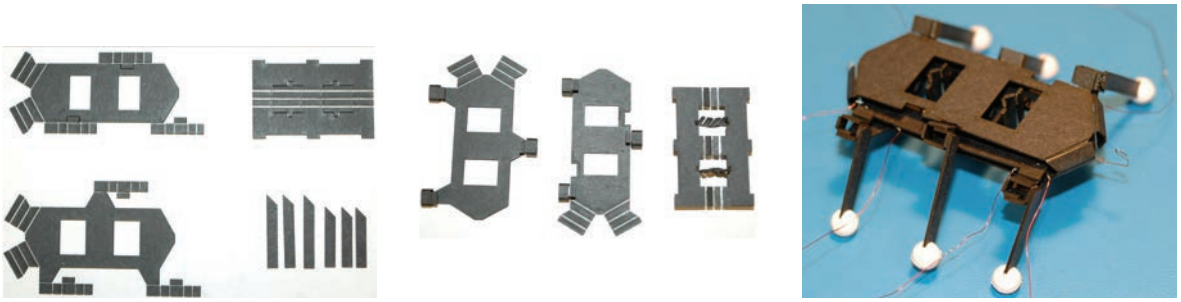

(a) Flat prototype parts (b) Component linkages folded (c) Complete folded and assembled prototype

Figure 4.3: Progression of scaled prototype of a hexapedal legged robot from flat parts to folded final result.

the upper plate cause the legs to pull inward toward the body while the hips connected to the lower plate cause the legs to swing outward away from the body. This motion is depicted in Fig. 4.2b More detail and an analytical formulation of the kinematics are given later in Section 4.2.2.

4.1.3 Prototype Testing - First Steps

To test the prototype, the degrees of freedom shown in Fig. 4.2 were actuated with 75 μm SMA wire. Actuator timing was controlled manually, and the prototype was run on flat surfaces and an incline. Fig. 4.4 shows a sequence of frames from a video demonstrating the prototype walking in a quasi-static fashion on a flat surface. Fig. 4.5 demonstrates the ability of the prototype to walk up inclines as large a 30°.

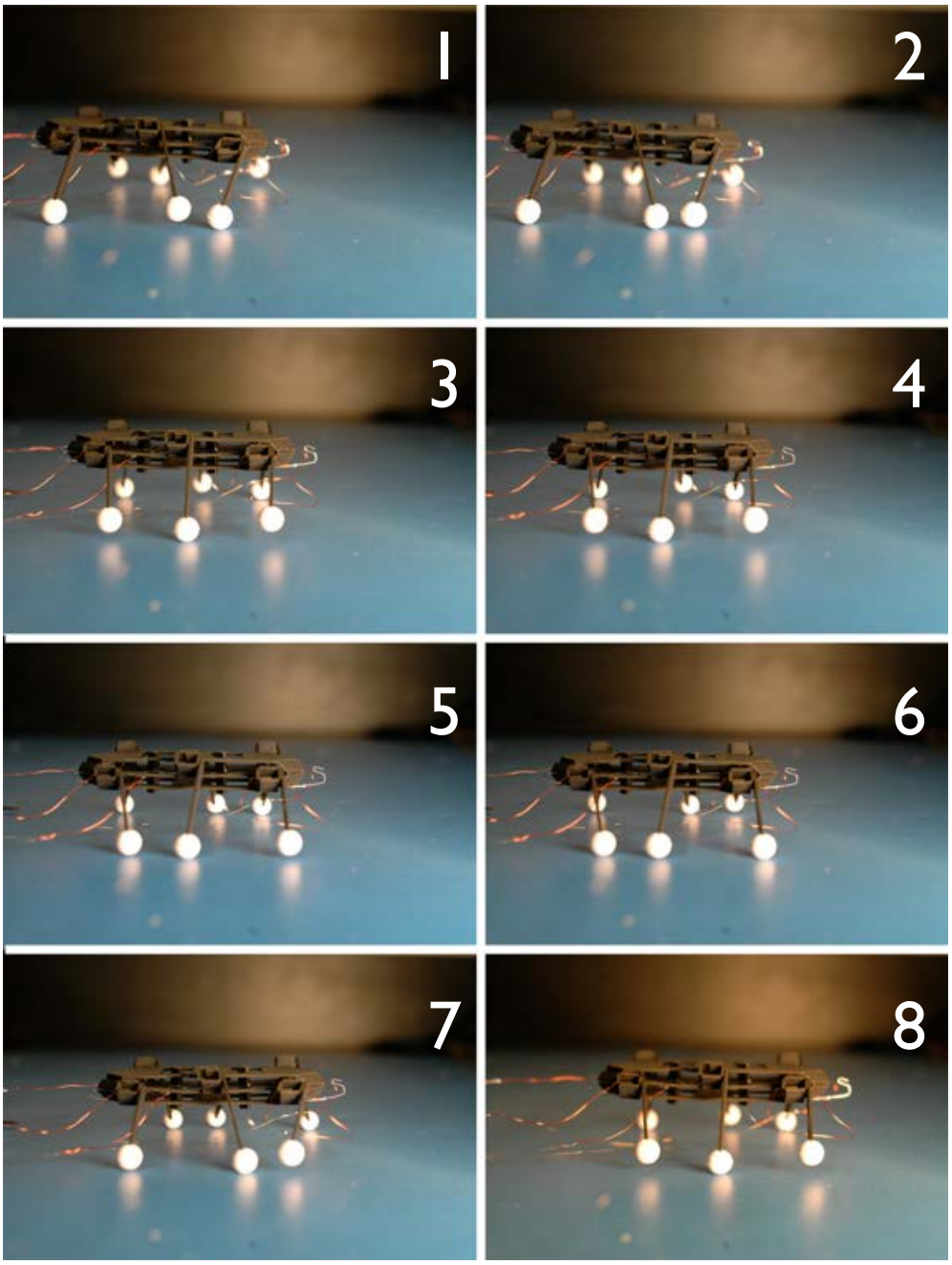

Figure 4.4: Time sequence of steps from the robot prototype's alternating tripod gait

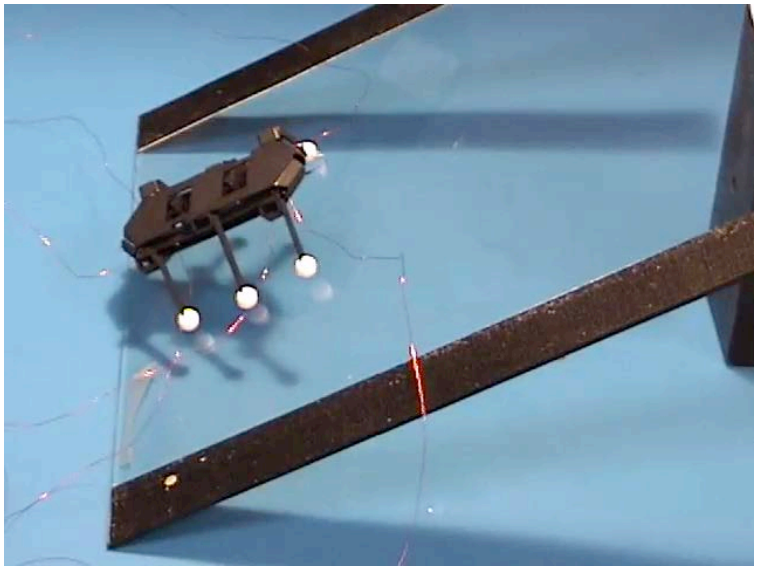

Figure 4.5: The robot prototype climbing a 30° incline enabled by the addition of spherical rubber feet.

4.2 Design and Fabrication at Scale

Building on the success of the 2X scaled prototype, we proceeded with the design for the robot at the milli-scale.

4.2.1 Fabrication Process

RoACH uses a modified version of the SCM process that enables alignment of uncured parts to each other before curing. This slight modification eliminates one curing cycle (approximately four hours) from the process used to fabricate the MFI, and this represents a significant reduction in the total time required for a fabrication cycle. The SCM process for RoACH's fabrication is depicted in Fig. 4.6 and the steps are outlined below.

1. The process begins with a sheet of uncured, pre-impregnated composite fiber laminate (S2-Glass).
2. Gaps are laser micro-machined into the composite fiber using a 25 W CO_2 laser (Versalaser, Universal Laser Systems).
3. A polymer film (PET) is placed on top of the laminate.
4. A laminate with the mirrored cut pattern is placed on top of the polymer layer.
5. The entire structure is cured.

6. The resulting flat structure is released.

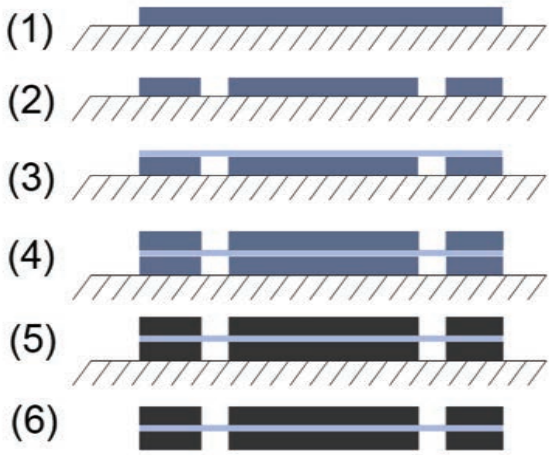

Figure 4.6: A step-by-step illustration of the SCM link and hinge fabrication process as implemented for the RoACH robot.

A palette of parts for the construction of RoACH is shown in Fig. 4.7. This palette demonstrates two distinct advantages of the SCM process. 1) It enables the fabrication of a robot with a large number of articulated joints for the same cost as a robot with a minimal number of joints. For example, RoACH's design uses 57 joints. This is in contrast to robotic design with conventional materials and mechanisms in which the cost of each joint is significant. In addition, the ability to add an arbitrary number of joints to the design makes it possible to implement the kinematic redundancy strategy for SCM mechanisms suggested by the analysis in Chapter 3. 2) Multiple copies of parts can be fabricated in parallel. The number of parts that can be made in parallel is limited only by the equipment used to produce them (ie. size of the laser cutting table, volume of the curing oven, etc.). These two factors combined make the fabrication of millirobots (from glass fiber composites, at least) inexpensive in terms of time and materials. From start to finish (including cure time and time required to populate the circuit board), RoACH requires approximately 16 hours to layup, cut out, assemble, and wire.

4.2.2 Mechanical Design

As discussed in Chapter 1, size limitations severely affect the power and control budgets for mobile millirobot designs. At the milliscale, actuators can be expensive from a weight perspective (in the case of piezoelectric materials) and/or an efficiency perspective (the case with SMA). Thus, minimal actuation is a core guiding principle of robotic design at this scale. This minimal actuation

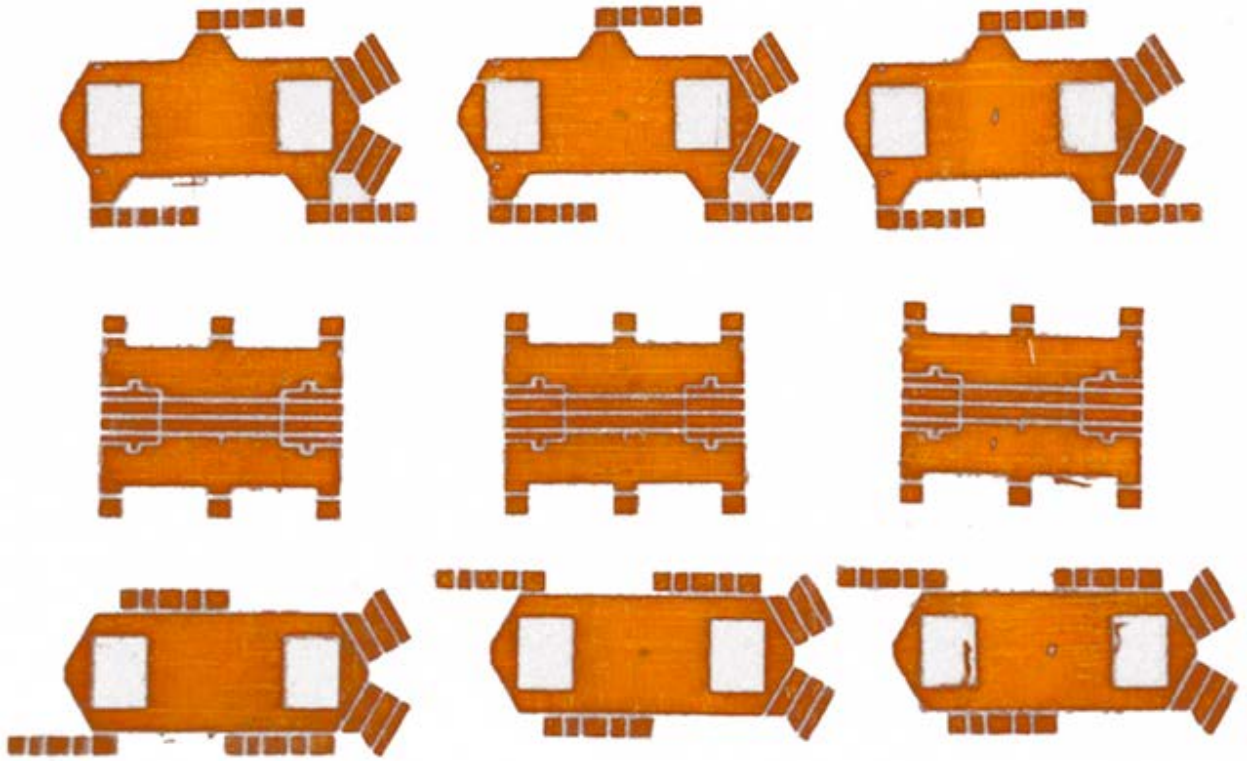

Figure 4.7: A palette of flat SCM parts showing 3 complete RoACH thoraxes ready for folding and assembly

constraint necessarily requires "programming" some of the robot's gait into the structure via the kinematics.

However, SCM has the advantage of being a near-monolithic fabrication process in which the cost of adding a single joint (and, hence, mechanism complexity) is essentially negligible. This enables us to create very complex parallel kinematic designs for little to no added cost in manufacturing. (Notably, though, complex designs require more time to assemble by hand.)

Actuation

Given constraints imposed by the milliscale, we chose SMA wire to provide actuation for a number of reasons. Firstly, SMA integrates easily with the SCM process. Alignment and routing features can be directly machined into the composites to enable easy attachment and tensioning of the SMA wire. Secondly, SMA wire provides a force in a single direction. One difficulty of working with compliant mechanisms is their susceptibility to off-axis forces and undesirable moments as discussed in Chapter 3. The single line force between points of attachment of SMA enables greater design freedom. Additionally, the target operating speed range (1 - 15 Hz) makes SMA viable. Lastly, it's lightweight. One 80 mm actuator weighs less than 1 mg and can generate up to approximately 0.5 mW of mechanical power.

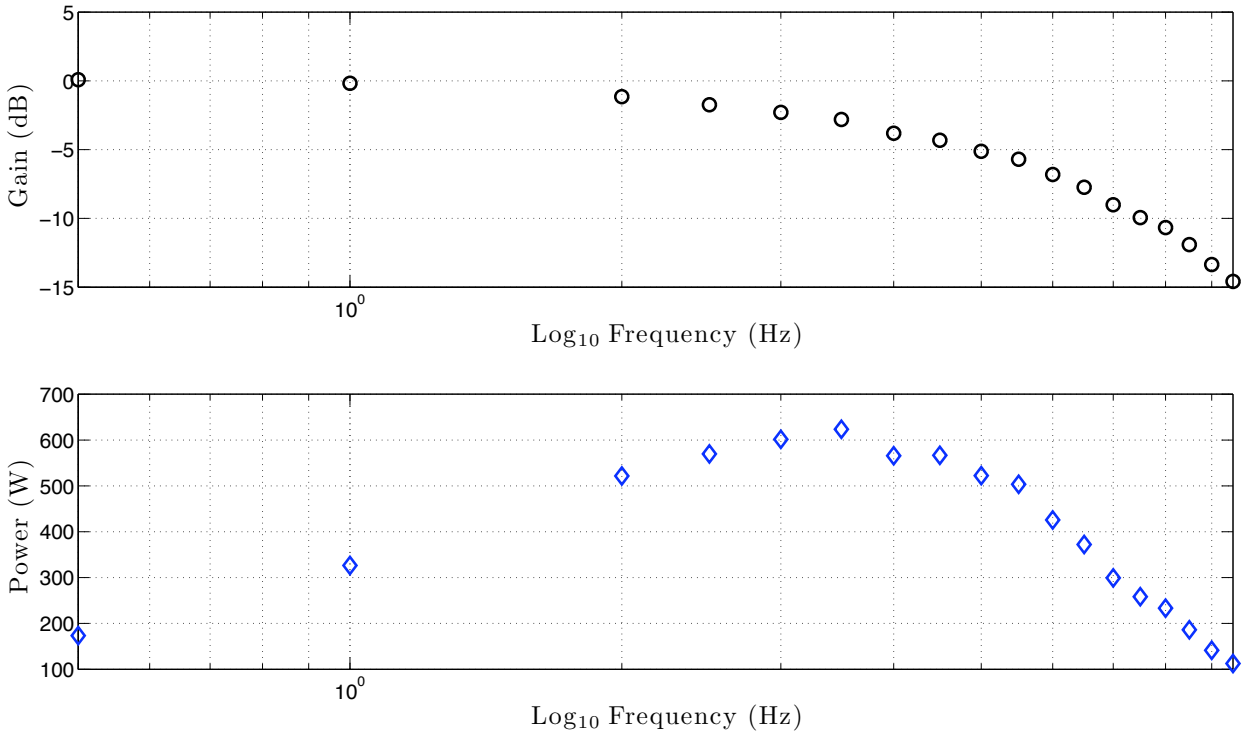

Figure 4.9: Frequency response (above) and output power (below) for a 37.5 μm (1.5 mil) diameter straight shape memory alloy wire actuator.

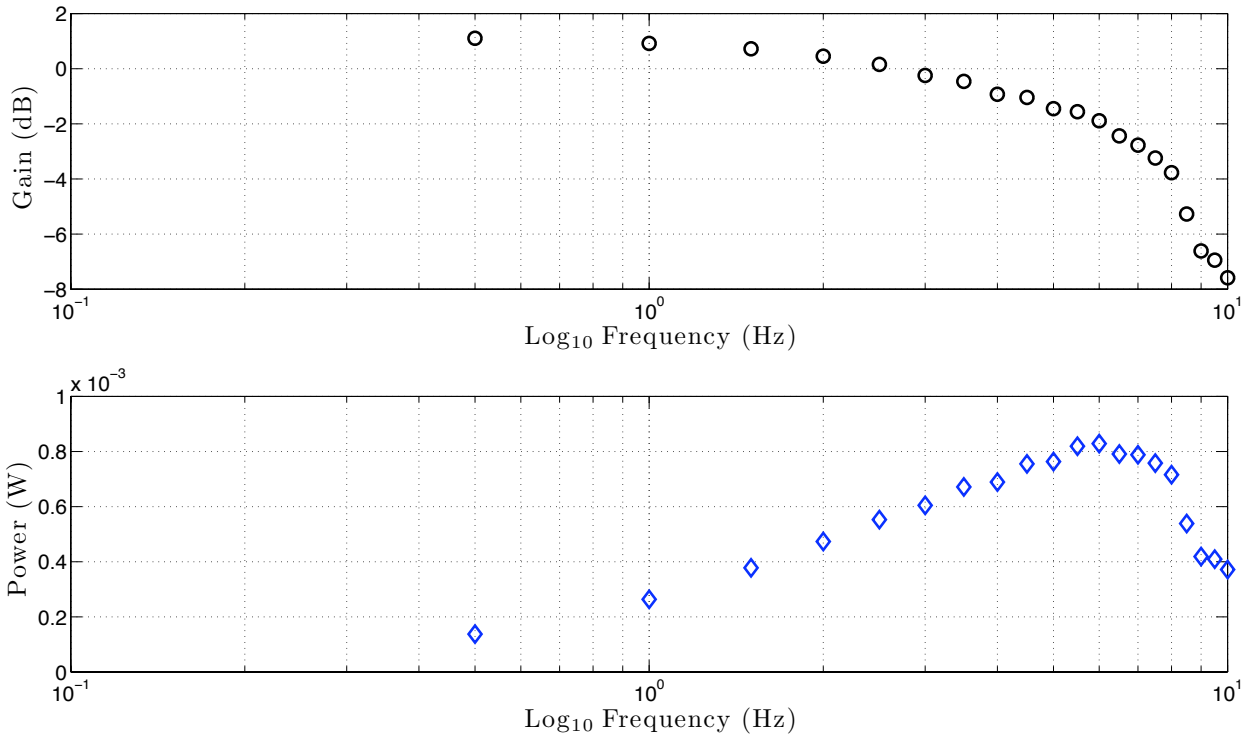

Figure 4.8: Frequency response (above) and output power (below) for a 25 μm (1 mil) diameter straight shape memory alloy wire actuator.

Dynamic characterization data for 25 μm and 37.5 μm SMA wire are shown in Figs. 4.8 and 4.9 respectively. The data shown were collected in a series of benchtop experiments in which the SMA wire was connected to a parallel beam flexure spring with a stiffness of 170 N/m and actuated over a range of frequencies. Displacement was measured using an infrared emitter/collector sensor. The 25 μm wire resulted in a bandwidth (using the -3 dB criterion) of approximately 7.5 Hz with peak power achieved at 6 Hz. The 37.5 μm wire demonstrated a bandwidth of approximately 3.5 Hz with peak power at the same frequency.

However, because SMA is a tensile actuator only, it is necessary to provide a return force either with an antagonistic SMA or spring. With SCM, it is possible to design return springs into the hinges of the mechanism. Similar to tendons in animal muscles [25], this approach enables storage of elastic energy which is then returned when the actuator is switched off and the joint returns to its equilibrium state. The characteristics of the SMA actuators for our actuation conditions are summarized in Table 4.3. The SMA wire used in RoACH is 37.5 μm wire (Flexinol, Dynalloy Inc.), and it is attached to the robot by first crimping stainless steel hypodermic tubing to the ends of the wire and gluing the crimps to the robot's body. Exposed portions of the crimps provide solder connections for wires providing the electrical power to heat the wire.

The use of SMA is, however, not without its disadvantages. Lifetime of the wires can be significantly shortened by accidental overstraining or overheating. Care must be taken to ensure that preloading of the SMA does not exceed strain limits specified by the manufacturer [1]. In section 4.3, a drive scheme designed to heat the actuator quickly, but avoid overheating is described. This

approach helps extend the life of the actuator. While manufacturer's specifications claim lifetimes on the order of 10^6 cycles, a lifetime on the order of 10^4 - 10^5 cycles is a more reasonable estimate in this application.

Kinematics

RoACH's alternating tripod gait is achieved through a combination of kinematics and basic feedforward, clock-based control. A schematic depiction of the gait and a map of the actuator inputs corresponding to the gait positions are shown in Fig. 4.1 and Table 4.1 respectively.

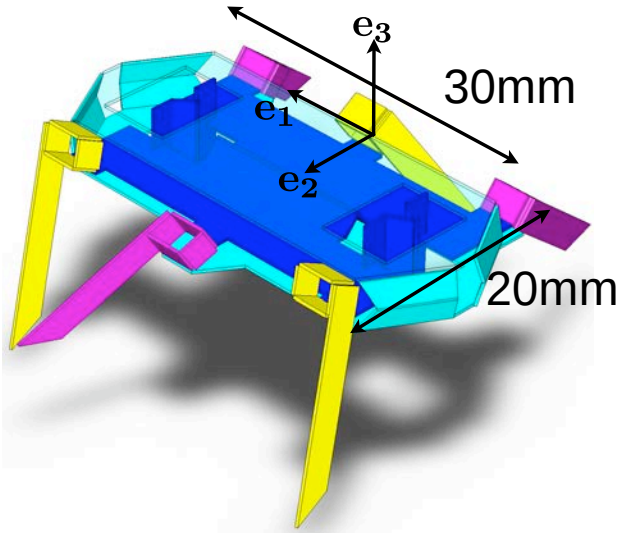

Figure 4.10: A CAD model of the robot showing the body-fixed basis used for kinematic analysis of the motion of the limbs. The top plate is shown nearly transparent so the inside of the robot may be seen.

RoACH's kinematics can be reduced to two translational degrees of freedom which are appropriately coupled through a central 2 DOF translating element to fourbar linkages that map those translational inputs into angular outputs. The design is ground-free in the sense that any rigid link could be used to establish the body coordinate system. RoACH's kinematics can be understood by examining two structures and their interactions: the central plate (shown in blue in the CAD model in Fig. 4.10) and the two outer plates of the body (shown in cyan, with the top plate transparent in Fig. 4.10).

The outer plates are constrained to move together in the horizontal plane, but are free to translate vertically with respect to each other. The middle plate is designed to contract laterally in the horizontal plane and is coupled to the upper and lower plates through fourbar linkages at the "hips" of the robot. From Fig. 4.10, when the central plate is moved forward along the anteroposterior

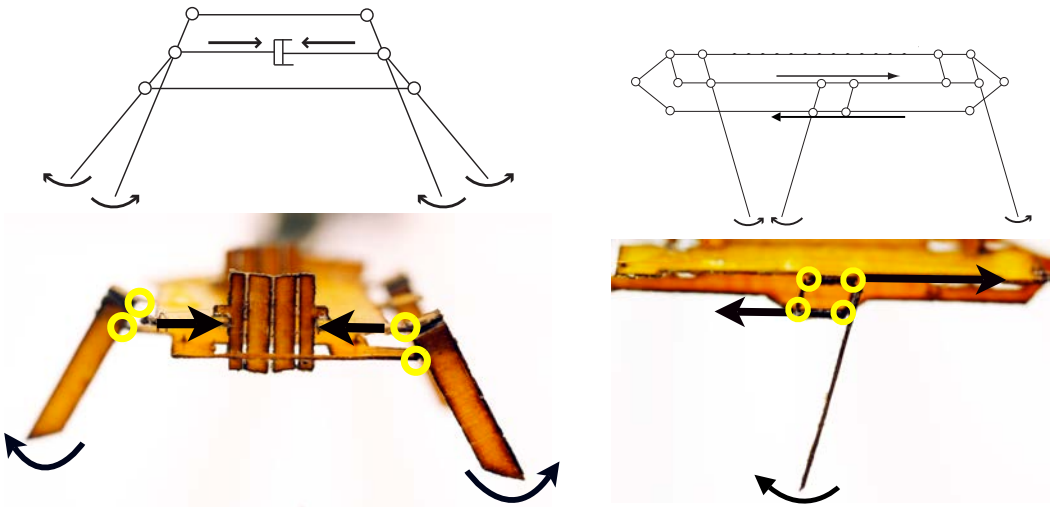

(a) First degree of freedom - abduction/adduction of the legs (rear view): model and actual robot (with only one tripod attached)

(b) Second degree of freedom - flexion/extension of the leg (side view): model and actual robot (one hip only)

Figure 4.11: Crawler kinematics depicting two independent degrees of freedom

axis of the body with respect to the outer plates, the magenta tripod swings back and the yellow tripod forward. When the central plate is contracted along the mediolateral axis of the body the magenta legs are lifted, and the yellow legs are lowered. These motions are also depicted individually in Fig. 4.11 while Fig. 4.13 shows the configuration of the SMA wire actuators used to control the two degrees of freedom.

The two links of each hip fourbar that remain parallel to the ground are hinged one to the middle plate and the other to either the upper or lower plate depending on which tripod it belongs to. Hips which are hinged to the top plate will cause their respective legs to be pulled toward the ground when the middle plate contracts laterally and those hinged to the bottom plate will be lifted from the ground. Likewise those hips hinged to the top plate will swing the legs forward when then middle plate moves forward with respect to the top and bottom plates while the hips hinged to the lower plate will swing the legs backward.

The kinematics can be written explicitly using the body fixed basis shown in Fig. 4.10 in which the origin of the basis is located at the idealized point on the top plate where the middle leg attaches. The x_1 input represents the contraction of the first SMA in the $\mathbf{e_1}$ direction and swings the legs forward and back. The x_2 input represents the contraction of the second SMA in the $\mathbf{e_2}$ direction and is responsible for swinging the legs inward toward (or outward away from) the body

to engage or disengage the tripods with the ground. The position of the end of the middle leg with the coordinate basis attached at its hip can be computed from a simple rotation matrix:

$$\mathbf{r} = L_{leg} \begin{bmatrix} \cos\theta & \cos\psi\sin\theta & \sin\psi\sin\theta \\ -\sin\theta & \cos\psi\cos\theta & \cos\theta\sin\psi \\ 0 & -\sin\psi & \cos\psi \end{bmatrix} \begin{bmatrix} \mathbf{e_1} \\ \mathbf{e_2} \\ \mathbf{e_3} \end{bmatrix} \tag{4.1}$$

$$\psi = \psi_0 + \sin^{-1}(\frac{x_2}{2l}) \tag{4.2}$$

$$\theta = \theta_0 + \sin^{-1}(\frac{x_1}{2l}) \tag{4.3}$$

In Eqns. 4.2 and 4.3 l is the length of the vertical link of the hip fourbar as pictured in Fig. 4.16 and ψ_0 and θ_0 are the unactuated angles of the hip. Once the position of a single leg is known, the positions of the others are trivially determined due to the parallel nature of the design. Kinematics were also simulated using Matlab and the resulting visualization of the foot paths in the body-fixed reference frame is shown in Fig. 4.12.

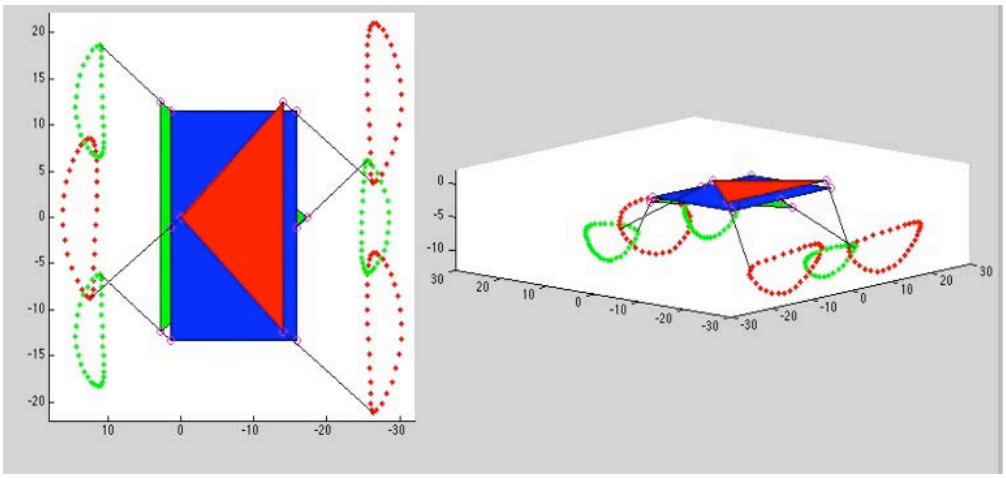

Figure 4.12: Output from a simulation of the robot kinematics showing the closed paths along which the feet travel with respect to the body.

Flexure linkage design

Each degree of freedom in the robot begins its actuation cycle at one extreme of its output motion and must be returned to this position at the end of one actuation cycle by the flexure return springs. Because our actuators provide primarily line forces aligned with the most compliant

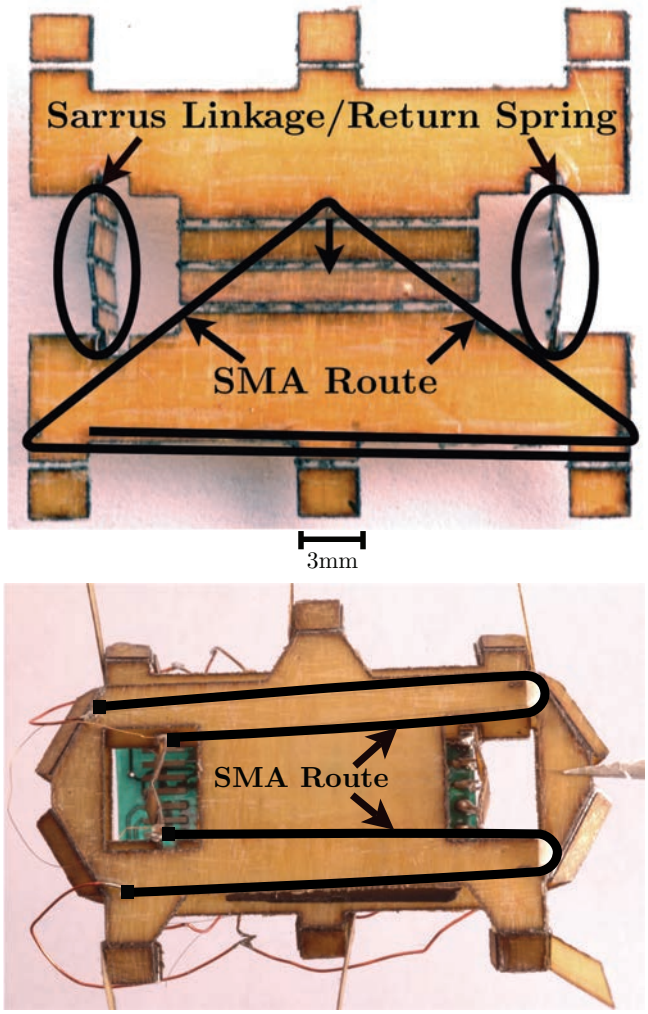

Figure 4.13: **Above:** The central contracting plate showing the route for the actuator responsible for abduction and adduction of the legs. **Below:** The bottom plate depicting the routing of the actuator connecting the bottom and middle plates and used to flexion and extension of the legs.

directions of our linkages, we have chosen to use the PRBM to get approximate linkage stiffness for the purpose of sizing our flexure hinges and our actuators.

Using the short flexure approximation [47], recall that the expression for the angular spring constant of a simple flexure hinge is:

$$K_\theta = \frac{Ebh^3}{L} \tag{4.4}$$

In Eqn. 4.4 E is the flexural modulus, b is the width of the flexure, h is the thickness, and L is the length.

The first return spring works in opposition to contraction of the middle plate shown at the top of Fig. 4.13. It consists of a compliant approximation of a Sarrus linkage - a spatial linkage which provides a single translational degree of freedom. The second degree of freedom is provided by the parallel fourbar linkage at the hip joint shown in Fig 4.16. The equivalent spring "constant" (the spring force is a nonlinear function of linkage displacement) for these linkages can be determined using Castigliano's second theorem as follows:

$$\frac{\partial U}{\partial q_1} = \mathbf{F}\frac{\partial s}{\partial q_1} = \mathbf{F}\frac{\partial s}{\partial x}\frac{\partial x}{\partial q_1} \tag{4.5}$$

In Eqn. 4.5 U is the potential or strain energy stored in the linkage, q_1 is a generalized coordinate (angular displacement of a link in our case), s is a generalized output displacement, and x is a linear output displacement. In our case, s and x are equivalent, so we solve for $\mathbf{F}$ as a function of x and differentiate to give the expression for the equivalent linkage spring constant, K:

$$K = \frac{\partial^2 U}{\partial x^2} \tag{4.6}$$

In the fourbar linkage it is also possible to induce the linkage to rest in a biased position such that the joint angles are not all 90°. This is accomplished by stiffening the flexure hinges at opposite corners. For a parallel fourbar with 2 joints catercorner from each other having a stiffness, K_1, and the other two having stiffness K_2 the rest angle, θ is given as:

$$\theta = \frac{\pi}{1 + \frac{K_2}{K_1}} \tag{4.7}$$

Thus it is possible to affect an arbitrary bias angle and therefore set the return point of the leg for the beginning of its stance phase simply by adjusting the stiffness of a flexure (either through material properties or geometric changes).

For a fourbar with an arbitrary bias angle induced by a stiffness differential in two of the four joints and loaded as in Fig. 4.14, the expression for the spring constant resulting from Eqn. 4.6 is:

$$K_{fourbar} = \frac{n_1 + n_2}{m} \tag{4.8}$$

$$n_1 = -2El\sqrt{1 - \frac{(x+d)^2}{l^2}}\,(I_1 + I_2) \tag{4.9}$$

$$n_2 = 2E\,(x+d)\left(\cos^{-1}\left(\frac{x}{l} + \cos\left(\frac{\pi I_2}{I_1 + I_2}\right)\right)(I_1 + I_2) - \pi I_2\right) \tag{4.10}$$

$$m = lL\,(d - l + x)\,(d + l + x)\sqrt{1 - \frac{(x+d)^2}{l^2}} \tag{4.11}$$

$$d = l\frac{\pi I_2}{I_1 + I_2} \tag{4.12}$$

In Eqns. 4.8 - 4.12, I_1 and I_2 are the area moments of inertia for the flexures represented as K_1 and K_2 respectively in Fig. 4.14, E is the modulus of the flexure material, and L is the length of all the flexures. In practice, the stiffness of each flexure joint could also be adjusted by changing L. Fig. 4.15 shows the force displacement curve for a biased fourbar with the same flexure and link length dimensions used on the actual robot.

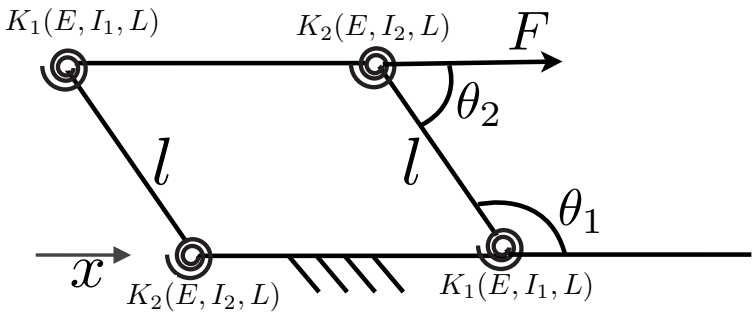

Figure 4.14: A kinematic model of a fourbar linkage using the pseudo-rigid body model to approximate joint stiffness.

Fig. 4.17 shows half of a Sarrus linkage where the linear constraint imposed by the non-planar portion of the linkage is instead replaced by a kinematically equivalent sliding joint. For the Sarrus linkage configuration shown, the stiffness is:

$$K_{Sarrus} = \frac{3EI}{2l^2L\left(1 - \left(1 - \frac{x}{2l}\right)^2\right)} - \frac{3EI\left(1 - \frac{x}{2l}\right)\cos^{-1}\left(1 - \frac{x}{2l}\right)}{2l^2L\left(1 - \left(1 - \frac{x}{2l}\right)^2\right)^{3/2}} \tag{4.13}$$

Fig. 4.18 shows a force displacement curve for a Sarrus linkage of the same dimensions as the one used on the RoACH robot. We note that when $\alpha = 0$, the mechanism is singular, so a stiffness

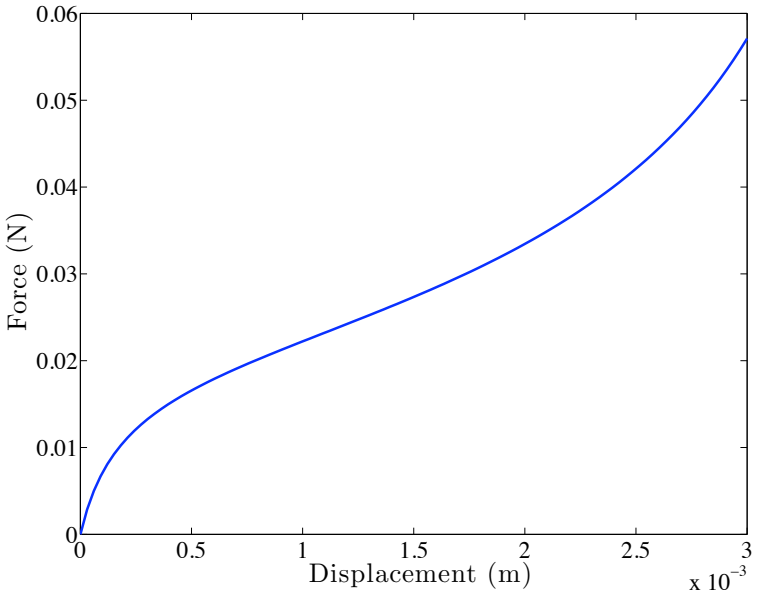

Figure 4.15: Force displacement curve for a biased fourbar linkage loaded only in the x direction.

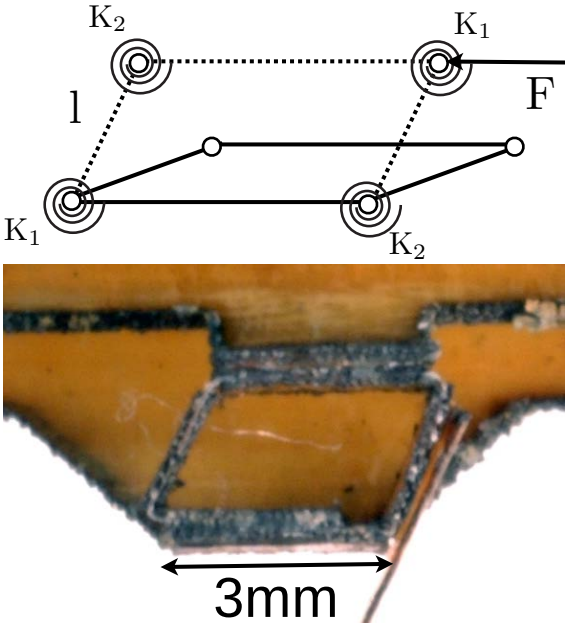

Figure 4.16: Above: A model of a biased parallel fourbar (shown relaxed and displaced) using flexure hinges as springs with different rotational spring constants. Below: an actual hip fourbar in equilibrium position on the robot showing the biased return spring for forward and backward swinging of the legs.

cannot be computed at the position. In practice, we always operate the Sarrus linkage with some initial displacement to prevent it reaching a singular configuration.

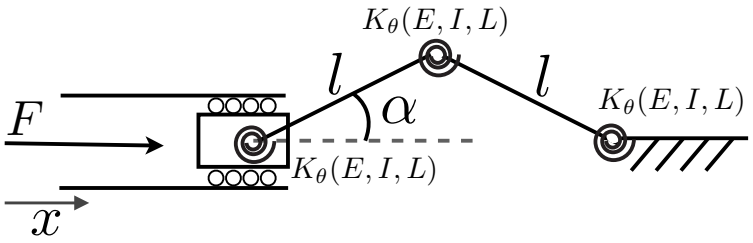

Figure 4.17: A kinematic model of half of a Sarrus linkage using the pseudo-rigid body model to approximate joint stiffness.

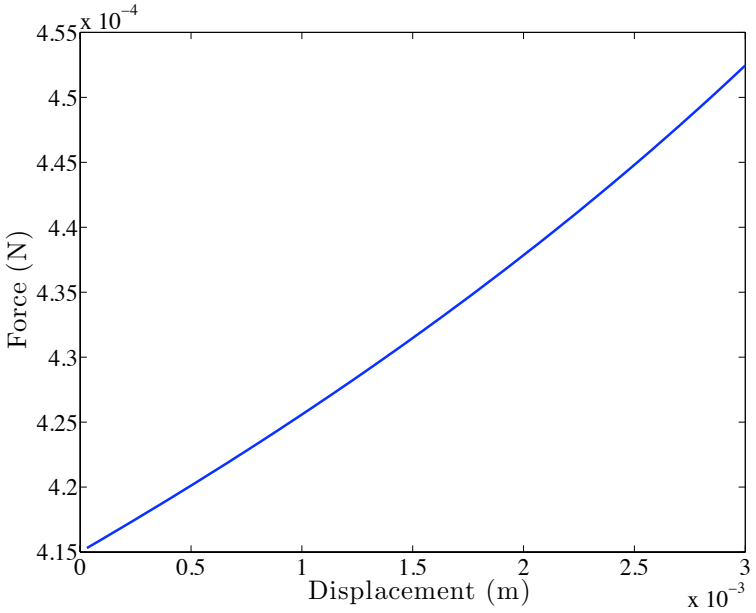

Figure 4.18: Force displacement curve for a Sarrus linkage loaded in the x direction.

SMA Kinematic Constraints

It is also important to note that the displacement limitations of the SMA wire must be considered in the kinematic design. For example, to achieve our desired angular displacement of the legs, we require approximately 3 mm of linear displacement from each actuator. By conservative estimation, SMA wire is capable of 3% strain, implying a requirement of 100 mm length wire. In theory it would be possible to achieve the same displacement output from several SMA wires connected mechanically in series, but electrically in parallel and avoid issues associated with the

high electrical resistance that accompanies long wires. However, for simplicity, we have chosen a single continuous wire for each of the actuators. The electronics design ramifications of this decision are discussed in more detail in the following section.

4.3 Electronics Design

For very small robots, integration of power and control electronics is a crucial design consideration. Since the selection of lightweight batteries at this scale is limited, the battery represents a high percentage of the overall robot weight. Likewise, since custom integrated circuits are quite expensive, lightweight PC board construction is the practical solution for electronics design. Nonetheless, the electronics are still relatively heavy, representing a significant portion of the robot's weight. Careful selection and design of electronic components can decrease overall robot weight significantly, improving performance.

System	**Component**	**Mass (mg)**
Control Electronics	Blank Board	180
	PIC Processor + LEDs	97
	Regulator + Battery Monitor	22
	IrDA	103
SMA Power Electronics	Blank Board	124
	DC-DC Converter	153
	Drive Transistors	10
Power Supply	Battery	847
Structure	Skeleton + Joints	700
Actuators	SMA Wires + Crimps	2
Wiring	Wiring, Solder, Trim	160
Total Mass:		**2398**

Table 4.2: Mass breakdown for the entire robot

4.3.1 Control Board

A lightweight circuit board is needed for controlling the SMA actuators as well as for steering, communication, and potential future sensing needs. A custom 402 mg control electronics board (shown in Fig. 4.19) was manufactured using, 25 μm core FR4 fiberglass. The board utilizes surface mount components and features a connector not only to the power electronics but also to a sensing "daughter" card. None is presented here but several daughter cards exist for such sensors as accelerometers, gyros, or a compass. This control board is a more recent revision of the control

board used in [92], which demonstrated autonomous glider navigation toward a light using an infrared sensor.

4.3.2 Power and Processing

The control board contains a 10 Mips PIC LF2520 processor running at 3.3 V through a ZXCL330 low dropout regulator. The PIC processor was chosen for its internal oscillator to save weight and for its low power consumption. Red and green LEDs indicate battery voltage status using a MN1382 battery monitor. RoACH is powered by a 20 mAh Lithium polymer battery (Model# 301218HS20C, FULLRIVER Battery New Technology Co.) that weighs 850 mg (after trimming).

4.3.3 Wireless Communication

The board contains a complete implementation of the bidirectional IrDA infrared communication standard common in PDAs and laptops. Infrared communication uses very little power compared with RF technologies like Bluetooth. The lack of antenna also decreases the weight of the module at the expense of range. Communication uses the PIC's hardware UART and communicates with a PC at 115.2kbps via a serial port and IrDA converter.

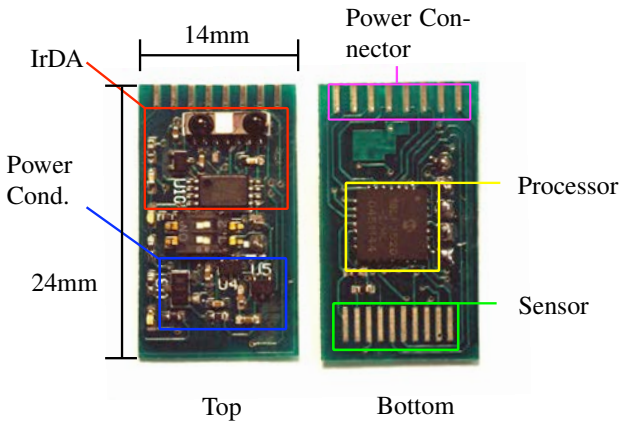

Figure 4.19: Top and bottom of the control electronics PC board.

4.3.4 SMA Power Supply

SMA wire is a thermal actuator, actuated by resistive heating with the power requirement for each actuator given by:

$$P = I^2 R \tag{4.14}$$

where R is the resistance of the Flexinol (SMA) wire. The SMA power supply should be capable of driving a variety of wire sizes. Available Flexinol wire diameters and the associated resistance per unit length (from www.dynalloy.com) are shown in Table 4.3.

Wire Diameter (μm)	Force Output (g)	Resistance (Ω/in)	Maximum Pulse Current (mA)
25	7	45	60
37.5	17	21	100

Table 4.3: Two Flexinol sizes and associated characteristics. Maximum pulse current estimates are from our own experiments.

The maximum length of SMA wire in the design is approximately 100 mm. For 25 μm wire, the resistance is 177 Ω. To drive the maximum of 60 mA pulsed current through this resistance, a voltage of 10.6 V is needed, meaning a DC to DC converter is necessary to boost from the nominal battery voltage of 3.7 V. A safety factor was included to make the target output voltage of the SMA power converter 13.6 V. This is the highest voltage necessary to drive either of the wire diameters in Table 4.3. Maximum output power of the proposed DC to DC converter is 0.83 W for a single channel driving the 37 μm wire or 1.66 W for both channels. This target power output is an upper design bound only; both actuators are not pulsed to their maximum drive current at the same time.

A standard boost converter topology was chosen as the DC to DC converter. A Coilcraft LPS4018 15.3 μH surface mount inductor weighing 97 mg was used for its light weight and high current tolerance (0.86 A, 10% drop). Switching is realized via an LT3580 boost converter IC capable of switching frequencies from 200 kHz to 2.5 MHz. A high speed, Schottky diode was used for switching (UPS120). Resistors govern both the switching frequency and the output voltage, making the circuit easily customizable for different SMA wire diameters. An efficiency plot for 1 MHz and 2 MHz switching frequencies at 13.6 V output voltage and 3.5 V input voltage is shown in Fig. 4.20.

The use of the DC to DC converter could have been avoided by connecting several SMA wires mechanically in series, but electrically in parallel. The 3.7 V battery is capable of sourcing the required 60 mA of current (for a 25 μm SMA) into a 61 Ω resistive load. With a resistance of 1.8 Ω per mm, a 100 mm actuator would need to be broken into at least three segments to be driven by the battery with no boost circuitry. The series mechanical/parallel electrical arrangement adds significant complexity to the design motivating our design decision to use the DC to DC converter.

The boost converter was implemented on a 25 μm core FR4 custom PC board (like the control board). It was fabricated to match the power connector on the control board and is shown in Fig. 4.21. Its total weight is 340 mg.

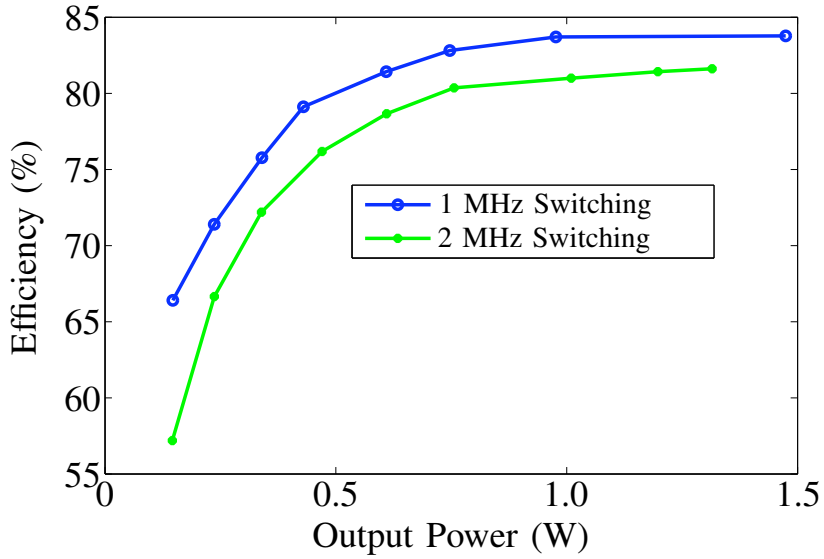

Figure 4.20: Miniature power supply efficiency for 1 MHz and 2 MHz switching frequencies.

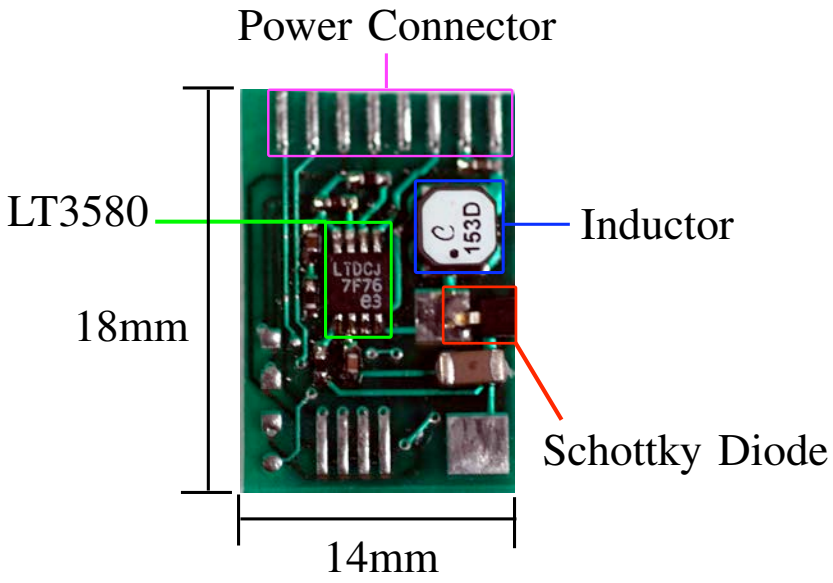

Figure 4.21: Miniature boost converter pc board.

4.3.5 SMA Drive Method

The boost converter was used as the biasing voltage for an NMOS transistor (FDG6301N). An optional current sensing resistor is routed on the PC board to an A/D input of the PIC processor

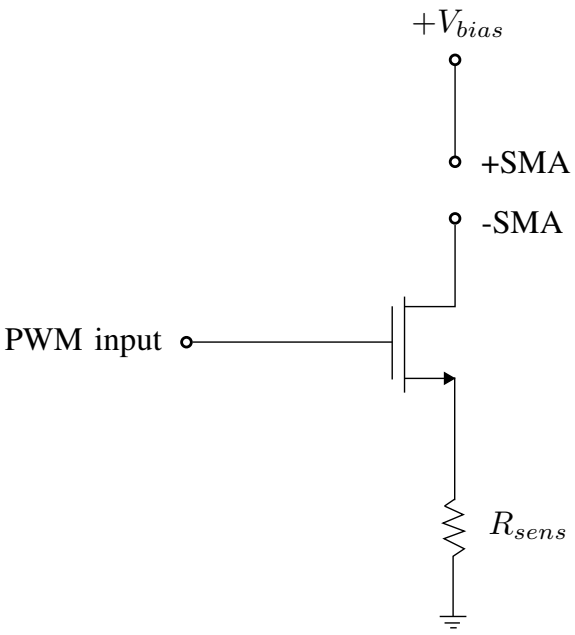

Figure 4.22: Transistor drive scheme for SMA.

for future implementation of closed loop current control. The gate of the NMOS was driven by the PIC with a PWM signal (19 kHz) to govern the current through the SMA wire. A "spike" plus "normal" current drive method was used to increase efficiency of the actuator. This approach achieves initial actuation with a large spike in the current drive that quickly heats the wire. This spike is followed by a lower current level (normal level) that keeps the wire heated. An illustration of the drive scheme is shown in Fig. 4.23.

Using the drive scheme depicted in Fig. 4.23 we actuate the alternating tripod gait, but programming a phase difference of approximately 90°. This phase difference between the two actuator signals effectively produces the gait depicted in Fig. 4.1. To achieve steering, phase difference between the two channels is varied (more on steering in Section 4.4.1).

4.3.6 Communication/Software

The control board utilizes IrDA for wireless communication. Both the gait control PC and the robot control board implement a cyclic redundancy check to detect communication errors. The interface to the robot that enables updating the gait parameters and starting and stopping the robot is a GUI written in Matlab. The software communicates with the robot continuously and can change gaits (if needed) each step cycle. Currently, we tele-operate the robot with an open-loop feedforward signal. The step profile is only changed every several steps for turning or stopping.

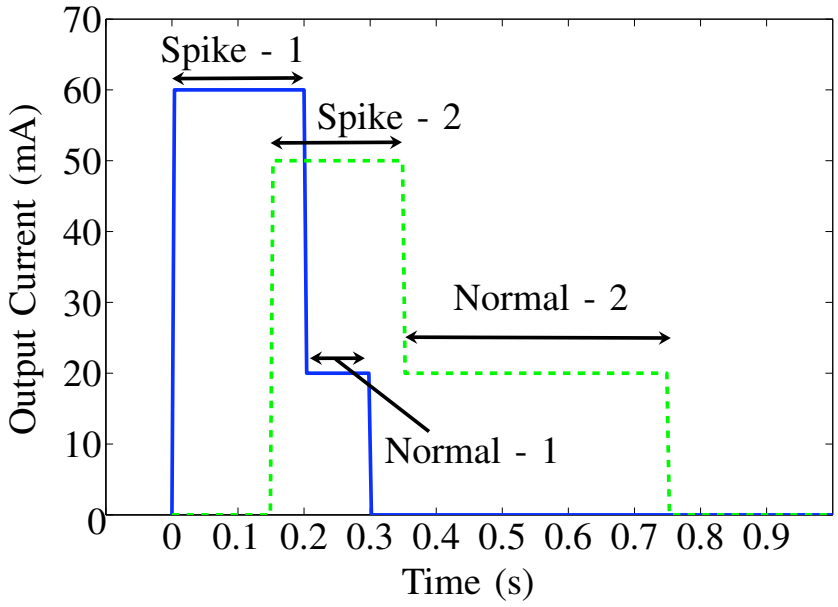

Figure 4.23: Typical current drive profile showing spike and normal hold currents for two actuators each switched at 1 Hz.

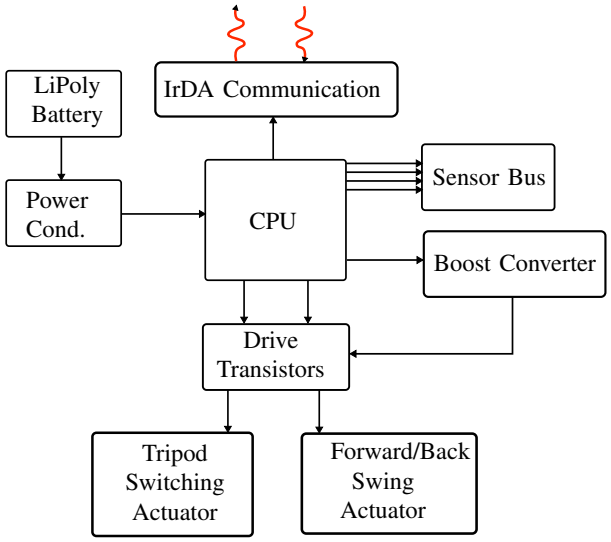

Figure 4.24: Electronics block diagram.

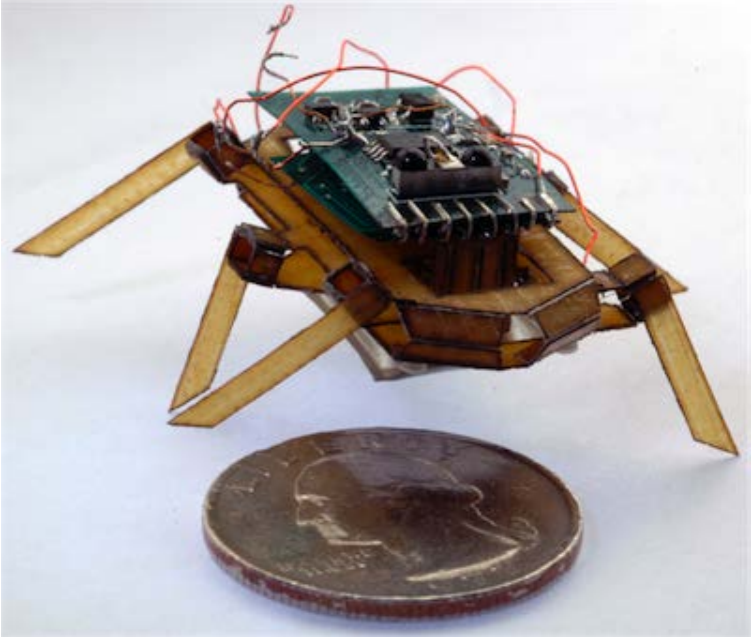

Figure 4.25: The 2.4 g RoACH standing over a US quarter

4.4 Experimental Results

The robot was run wirelessly in a series of trials and gait parameters such as the phase delay between the two actuators, current spike duty cycles, and the use of a normal or hold current were tuned experimentally. Our best results show the robot crawling at approximately 1 body length or 3 cm/s. Experimental battery life tests indicate a maximum running time of over 9 minutes when the legs are driven continuously at 3Hz, a frequency just beneath the 3dB point for 37.5 μm SMA wire.

4.4.1 Turning Control

To achieve turning, differential leg lengths were used. Both middle legs are slightly shorter than the four corner legs. During front/back swing actuation, the lateral degree of freedom is actuated before the swing finishes. This momentarily places the four corner legs on the ground simultaneously without the middle legs engaging with the ground. Since the legs on the left side are moving in the opposite direction to the legs on the right, a moment is applied to the robot. Slipping on one or both of the sides will occur, causing the robot to turn. As seen in Fig. 4.26, both left and right turning can be controlled simply through timing the actuation of the lateral (tripod switching) degree of freedom. To our surprise, gait parameter exploration also revealed that with zero forward velocity, the robot is capable of turning at a rate of approximately 1.5 rad s^{-1}.

Body Size	30 mm x 20 mm x 15 mm
Mass	2.4 grams
Maximum Speed	3.5 mm/s (1 body length/s)
Maximum Stride Frequency	3 Hz
Leg Angle	$\pm 30^{\circ}$
Power Consumption	1.3 W
Actuators	$2\times$ 37.5 μm dia. x 100 mm Shape Memory Alloy wire
Actuator Resistance	82.7 Ω each
Battery	20 mAhr, 20 C Lithium polymer (Full River)
Total Battery Life	9.5 min. at maximum speed

Table 4.4: Summary of the physical parameters for RoACH

Robot	**Size**	**Mass**	**Onboard Power/Control**	**Speed** (body lengths/sec)
Silicon μbot [28]	1.5 cm	83 mg	No	0.4
Mesoscale Quadruped [38]	9 cm	104 g	Yes	3
LIPCA Hexapod [99]	12 cm	35 g	No	1.5
HexBug [49]	5 cm	15.6 g	Yes	1.2
ARRIpede [68]	1 cm	3.8 g	Yes	0.15
RoACH	3 cm	2.4 g	Yes	1

Table 4.5: A comparison of similarly sized legged robots

4.4.2 Energetics

One major focus within the study of locomotion in organisms is energetics. One common approach to assessing the efficiency of an animal's mode of locomotion is called metabolic cost of transport [7]. The metabolic cost of transport is the measure of total energy required by an organism to move one kilogram of its mass one meter. The metabolic cost of transport can also be written:

$$\text{Metabolic Cost of Transport} = \frac{\text{Power}}{\text{Speed} * \text{Mass}} \tag{4.15}$$

This metric can also be applied to engineered systems like the RoACH robot. At maximum speed, RoACH consumes approximately 1.3 W of power. At the maximum walking speed, this implies a metabolic cost of transport of nearly 18,000 J/Kg-m! Fig. 4.27 puts this number in the context of biological systems. Though organisms necessarily become less efficient as their size decreases, RoACH's metabolic cost of transport is still more than two orders of magnitude larger than similarly sized biological systems.

The primary cause of RoACH's high cost of transport is the low efficiency of the shape memory alloy actuators. Previous studies [85], [63] have reported theoretical efficiency limits in the range of

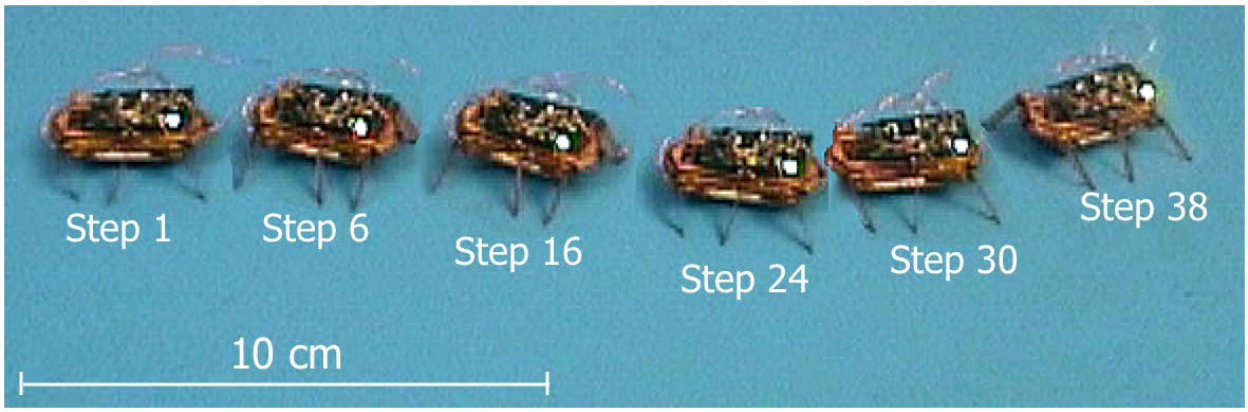

Figure 4.26: Composited frame captures from video demonstrating controlled right and left turning

3 - 13% for a single straight wire and ideal Carnot efficiencies of 8 - 15% for the same configuration depending on how output work is calculated. However, experimental reports of 1% efficiency (or less) are common in the literature [50]. This severe performance limitation will motivate the approach taken in the following chapter of using a single DC motor as a main power drive and shape memory alloys as lightweight steering actuators.

4.5 Concluding Remarks

In this chapter, we have presented mechanical and electronic designs as well as experimental results for an autonomous 2.4g hexapedal millirobot called RoACH. The robot is enabled by the SCM process for millirobot fabrication. We have demonstrated straight walking and controlled turning at speeds up to 3 cm/s. To the author's knowledge, as of 2010, RoACH was the smallest and lightest autonomous legged robot.

Though RoACH represents a significant step forward in the design and fabrication of legged mobile millirobots, efficiency of locomotion at this scale continues to be an issue. While shape memory alloy actuators are a good choice for actuation from the perspectives of ease of integration and control as well as power density, they are remarkably inefficient, especially compared to standard electromechanical actuators like DC motors. The next chapter introduces a hexapedal legged robot design approximately one order of magnitude larger (in mass) than RoACH, that takes advantage of dynamic locomotion and more efficient actuation and kinematics to be several orders of magnitude more efficient.

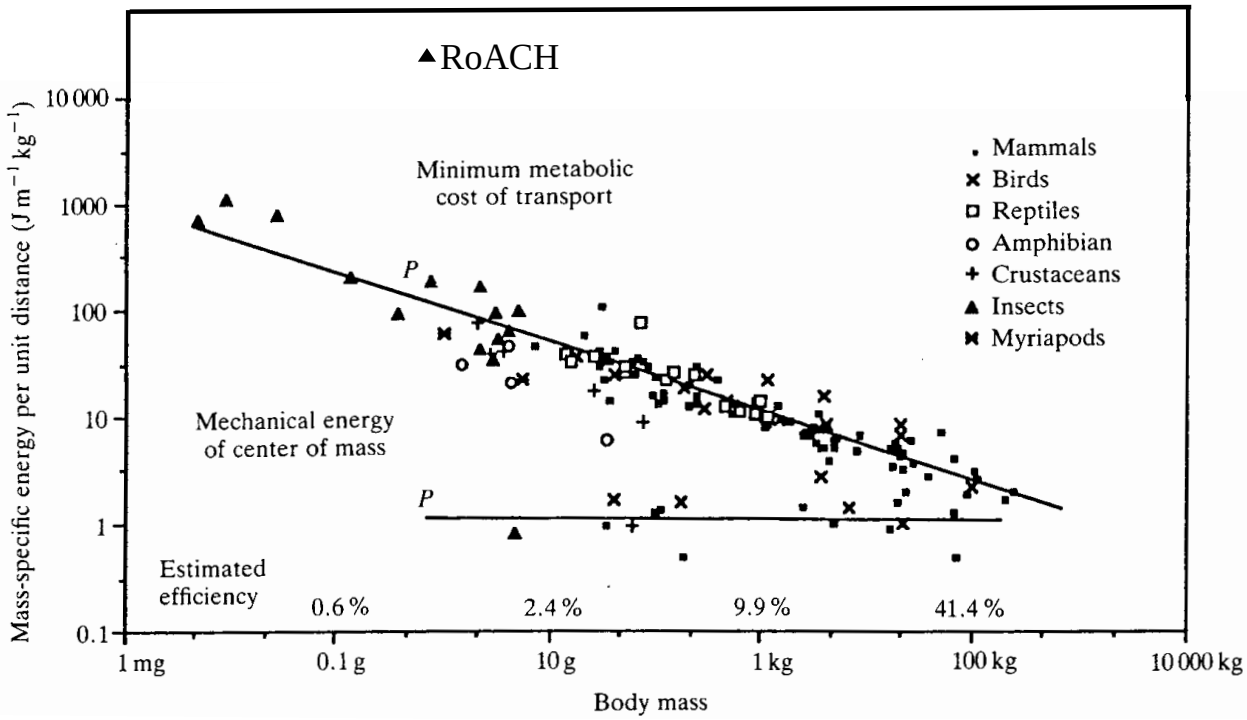

Figure 4.27: Data from [33] showing typical costs of transport for organisms over a range of sizes. Metabolic cost of transport for RoACH is shown in red and is approximately 18,000 - more than two orders of magnitude larger than similarly sized legged organisms.

Chapter 5

DynaRoACH: Design and Dynamic Maneuverability of a Hexapedal Runner

In this chapter, we present the kinematic design of a lightweight and efficient SCM-based transmission for driving a small legged robot from a single DC motor. Compared to the RoACH robot of the previous chapter, actuation using a DC motor enables far more dynamic and efficient locomotion than with SMA actuators. The single motor design also reduces the mass of the robot compared to one motor per leg designs like RHex [75] and yields a feedforward clock-driven gait. Coupling the transmission with passive compliant legs which exhibit viscoelastic damping results in stable dynamic straight-ahead running. Inspired by turning mechanisms in cockroaches, we demonstrate the potential to achieve turning during dynamic running by varying the stiffness of a single leg. For this work, stiffness was adjusted by physically exchanging the nominal legs for those fabricated from a stiffer material. We also experimentally establish the feasibility of using shape memory alloy wire to actively induce a change in the dynamic stiffness of the leg, providing a path to integration. Finally, preliminary data suggest that a large change in stiffness may enable dynamic maneuvers such as full-speed 90° turns over the course of 5 strides.

5.1 Robot Design

A major challenge in building a small-scale light-weight many-legged robot is the minimization of the number of actuators required to produce effective locomotion. The primary gait used by cockroaches running at high speed is the alternating tripod gait in which ipsilateral front and hind legs move in phase with the contralateral middle leg. Inspired by the incredible locomotory performance of these animals, we sought to design a robot's kinematics such that all six legs could

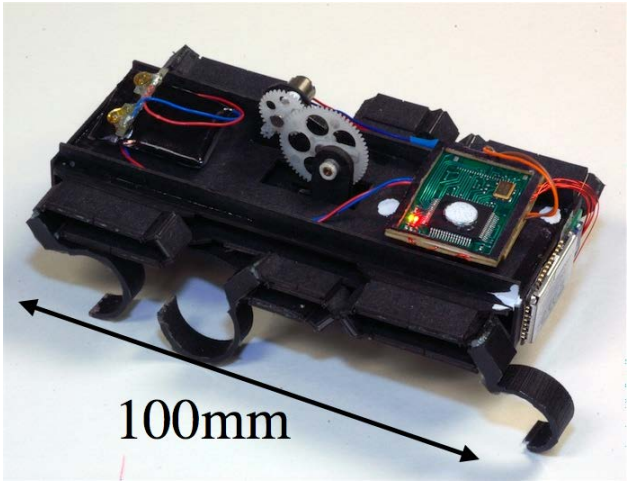

Figure 5.1: The DynaRoACH robot.

be driven by a single actuator to produce the alternating tripod gait at high speeds. Though it may seem arbitrary to restrict ourselves to a single motor for forward running, a minimal number of actuators is generally desirable for small-scale robots due to constraints on power density. In fact, for legged robot designs employing one motor per leg, each motor only does positive work on the robot for approximately 30% of the stride.

We have chosen a brushed DC motor as our primary power actuator. DC motors have a variety of advantages; they are: relatively power dense [83]; inexpensive; straightforward to control; and commercially available in a variety of windings, yielding a spectrum of torque and speed characteristics. However, due to the small size of the motor and therefore high operating speed, we employ a large gear reduction to obtain stride frequencies in a useful range, approximately 8-20Hz.

5.1.1 Kinematic Transmission Design

The primary difficulty of using a single DC motor to drive a many-legged robot is the kinematic design of a transmission that couples the angular output of the motor to the oscillatory motion of the legs. The Whegs™family [67][60][18] of robots uses a single motor to power hybrid "wheel-legs" through a standard transmission that uses elements like gears and chains. The iSprawl [55] robot uses a single DC motor with an attached slider crank to drive an arrangement of push-pull cables that lengthen and shorten its legs while protraction and retraction are accomplished passively using compliant rotational hips made from a viscoelastic polymer.

In the fabrication of the transmission for this robot, we have chosen to use a prototyping process [44] that is a scaled version of the approach used in smart composite microstructures (SCM) mechanisms. This method has many advantages: it is quite inexpensive; its planar nature enables rapid fabrication and assembly; it produces strong, lightweight mechanisms free of friction

Total Mass	23.7 g
Body Size	100 x 45 x 30 mm
Maximum speed	1.4 m/s 14 body lengths/s
Maximum stride frequency	20 Hz
Mean Metabolic Cost of Transport	3.5 J/(Kg · m
Motor	Didel MK07-3.3
Battery	Full River 90 mAHr lithium polymer
Microcontroller	dsPIC33F
Communications	Bluetooth (Roving Networks rn41 @ 230 Kpbs)

Table 5.1: Robot physical parameters

and backlash; and the compliant mechanisms used in the robotic design can be synthesized and analyzed using standard kinematic approaches.

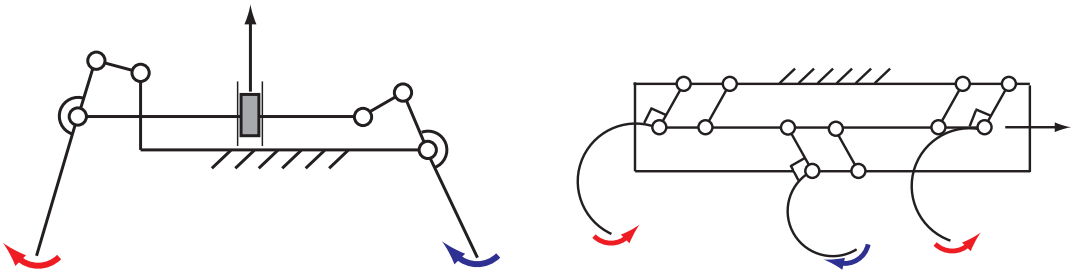

(a) Rear view of the ideal robot kinematics: ab- and adduction of legs from opposite tripods occurs out of phase when the middle member of the linkage is translated vertically

(b) Side view of the ideal robot kinematics: protraction and retraction of the legs is controlled by motion of the middle member in the fore-aft direction. The middle leg moves out of phase with the front and hind legs.

Figure 5.2: Ideal robot kinematics demonstrating the kinematic coupling enabling an alternating tripod gait. The motor output is aligned with the sagittal plane and a crank provides the vertical and fore-aft motion depicted in each figure.

The robot's kinematics are comprised of two primitive single degree of freedom mechanisms: the slider-crank linkage and the parallel fourbar. Rear and side views of the ideal kinematics of the robot are shown in Fig. 5.2. The slider crank linkages enable ab- and adduction of the legs, while fourbar linkages enable protraction and retraction.

Fourbar Kinematics

The fourbar linkages use a simple parallel geometry and therefore have a transmission ratio of unity. In fact, the driving configuration of the fourbars is an inversion of the standard configuration in which the crank is driven and output is taken from the rocker or coupler link. In the case shown in Fig. 5.2b, the coupler is driven by the output of the motor and the output of the fourbar is taken at one of the crank links to which a leg is attached. The fourbar was designed for a nominal protraction angle of $\pm 42^{\circ}$.

By inspection of Fig. 5.3, the output protraction angle of the leg with respect to the vertical is given by:

$$\theta = \sin^{-1}\left(\frac{h}{r_f}\right) \tag{5.1}$$

In Eqn. 5.1, h is due to the motion of the motor crank and is simply given by:

$$h = c \sin \alpha \tag{5.2}$$

where c is the length of the crank attached to the motor output and α is the crank angle measured with respect to top dead center.

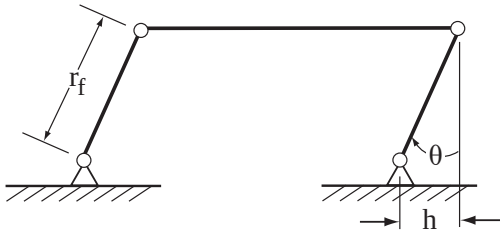

Figure 5.3: Schematic of fourbar kinematics

Slider Crank Kinematics

In Fig. 5.2a, the left slider crank is a kinematic inversion of the linkage on the right, and the two legs shown belong to opposite tripods. When the right leg is adducted, the left is abducted and vice versa. Each slider crank was designed to give a nominal abduction angle of 40° measured from the vertical.

To design the slider cranks, we solve the inverse kinematics problem — in our configuration,

the slider is the driven element while the output is taken from the crank which functions as a hip (see Fig. 5.4). The constraint equations are defined as follows:

$$\mathbf{A} = \begin{pmatrix} r_s \cos\psi \\ r_s \sin\psi \end{pmatrix} \tag{5.3}$$

$$\mathbf{B} = \begin{pmatrix} e \\ s \end{pmatrix} \tag{5.4}$$

$$(\mathbf{B} - \mathbf{A})^{\mathsf{T}}(\mathbf{B} - \mathbf{A}) = L^2 \tag{5.5}$$

Note that the link r is shared by both the fourbar linkage and the slider crank. However, in the slider crank formulation, r_s is the projection of r_f onto the transverse plane:

$$r_s = r_f \cos\theta \tag{5.6}$$

The input from the motor crank drives the slider in the vertical direction giving the relation:

$$s = s_0 - c(1 + \sin\alpha) \tag{5.7}$$

In Eqn. 5.7 s_0 is the initial value for s. Eqns. 5.3 - 5.7 are solved at top and bottom dead center of the crank to determine a value for the length of the coupler L that gives the 40° abduction angle.

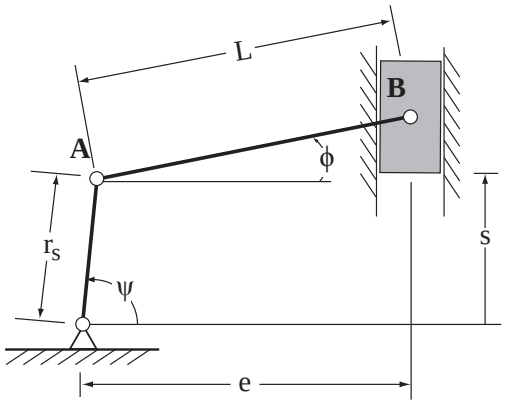

Figure 5.4: Schematic of slider crank kinematics

Eqns. 5.1 - 5.7 can be combined with the following loop closure equations for the slider cranks [62] to solve the 3D forward kinematics:

$$r_s \cos\psi + L\cos\phi - e = 0 \tag{5.8}$$

$$r_s \sin\psi + L\sin\phi \pm s = 0 \tag{5.9}$$

The sign of the s term in Eqn 5.9 is determined by whether the slider crank is a member of the left or right tripod. Three projections of the solutions to Eqns. 5.1, 5.8, and 5.9 are shown in Fig. 5.5.

5.1.2 Leg Design

We have chosen a semi-circle C shape for the robot's leg similar to the design used on the RHex robot [75]. The leg is manufactured by molding using a stiff polyurethane elastomer with 20% softener by weight (PMC-790 rubber and SO-FLEX softener, Smooth-On, Inc.). The C shape offers three primary advantages: lower vertical stiffness, directional collapsibility for obstacle climbing, and a rolling instead of point ground contact.

Lower vertical stiffness is obtained by changing the primary loading condition from material compression (as in a straight vertical leg) to material flexure. This allows for another actuator to more easily adjust the overall leg stiffness or to change the length of material allowed to deflect in a manner similar to the design in [34].

Collapsibility for obstacle climbing is achieved during forward running, where the open section of the C faces backwards. Upon collision with an object that is taller than the swing clearance height, the C can fold backwards, allowing the leg to continue its forward motion and position some portion of itself on top of the obstacle. During the stride phase, that leg can help pull the robot up and over the object.

The round shape of the C along with its compressibility allows it to form a rolling contact with the ground instead of the isolated point contact associated with a typical straight leg. The rolling behavior resembles a distributed foot, creating less vertical displacement of the center of mass and allowing for smoother overall motion [65].

5.1.3 Power, Communication, and Control Hardware

The robot uses the dsPIC33FJ128MC706-based microcontroller board described in [14] for control. Wireless communication is achieved using the Roving Networks rn41 Bluetooth radio interfaced to the PIC microcontroller. Full H-bridge motor control is possible with a custom 2 channel H-bridge motor driver board. However, for this work, the robot was run in a purely open loop, feedforward mode. The motor driver board includes a comparator circuit that enables real-time measurement of the motor back EMF voltage. The analog to digital converter on the PIC is configured to sample during the off portion of the pulse width modulation signal used to modulate the voltage of the motor drive signal.

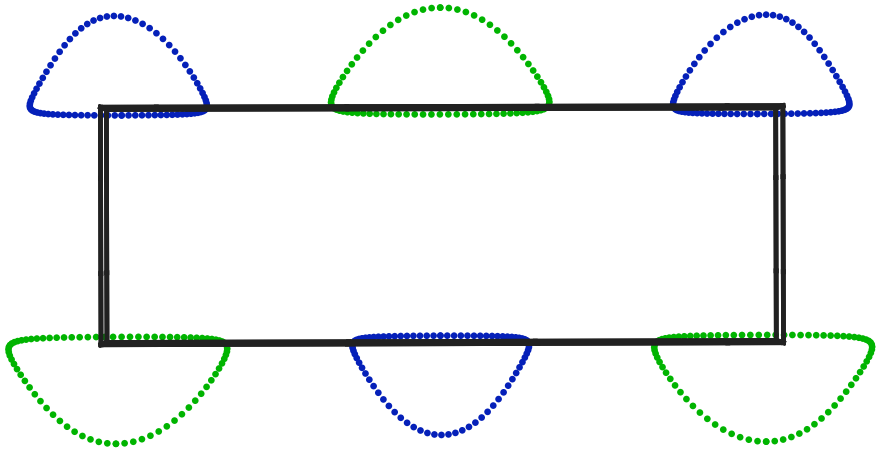

(a) Top view

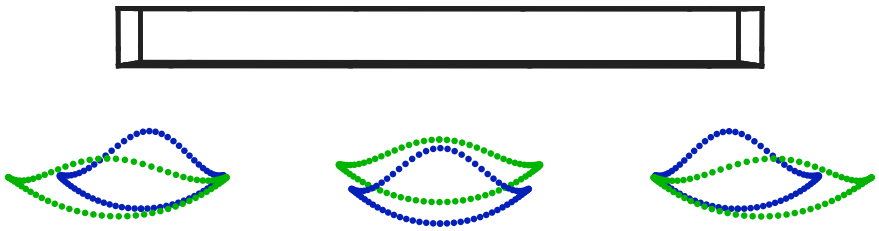

(b) Side view

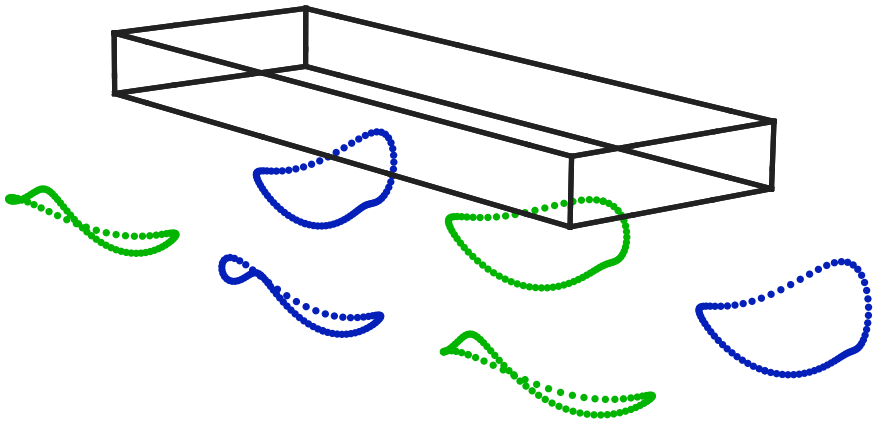

(c) Isometric view

Figure 5.5: Schematic views of the 3D foot trajectories of the robot plotted in the body-fixed coordinate frame.

5.2 Models for Dynamic Turning in Hexapods

In [52], Jindrich and Full argue that all legs of a cockroach can contribute to turning maneuvers. Inspired by measurements of leg kinematics ground reaction forces, they devise a simple planar model to describe turning. Then they propose a metric for leg turning effectiveness that represents the ability of the leg to generate forces perpendicular to the heading vector and apply the metric to the model. While the front leg on the outside of the turn was found to produce the most force perpendicular to the heading, the outside middle leg was also found to produce forces that rotate the cockroach appropriately. However, their model requires the middle leg to produce additional force parallel to the heading in order to compensate for the resulting change in body orientation relative to the heading.

In an effort to further explore the dynamics of turning, Proctor and Holmes demonstrated that the lateral leg spring (LLS) model [76], a low-dimensional conservative model of locomotion in the plane, is capable of producing dynamic turning [71]. By momentarily changing leg stiffness and touchdown angle, they demonstrate that translational kinetic energy can be temporarily exchanged for rotational kinetic energy, thus inducing a turn. In particular, they predict significant turning rates for increases in spring constant of $\approx 50\%$ and shifts in the location of the center of pressure (CoP) of less than $\approx 10\%$ of total body length; results from the simulation investigation are reprinted in Fig. 5.7.

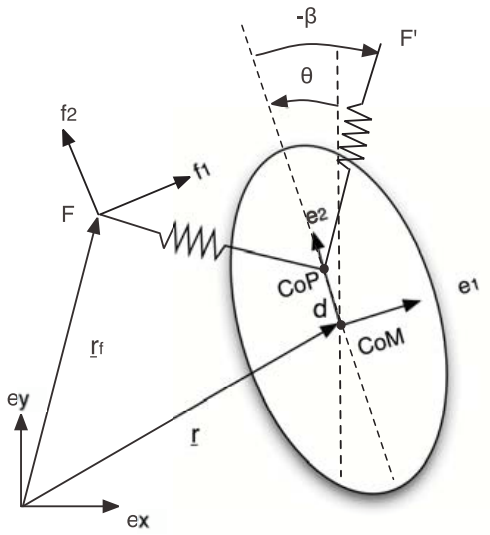

Figure 5.6: A schematic of the lateral leg spring (LLS) model and relevant physical parameters from [71].

While Proctor and Holmes' model seems to support Jindrich and Full's assertion that turning can be achieved with just small deviations from parameters for straight running, one drawback is that LLS parameters cannot be directly mapped to the actual parameters of a six-legged system. For example, LLS collapses a tripod of three legs into a single "effective" leg, making it impossible to

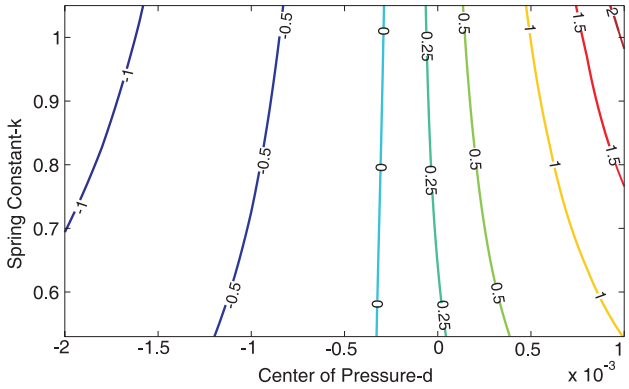

Figure 5.7: From [71]: A contour map of turning angle in radians over 3 strides as a function of the model parameters, leg spring constant, k, and distance between the center of pressure (CoP) and the center of mass (CoM) in mm.

differentiate between an outside front leg and an outside middle leg because those two legs belong to different tripods (but are located on the same side of the body).

For this reason, we attempt to induce turning of a real physical robotic system by directly adjusting leg stiffness and characterizing the turning behavior that results. By producing stiffness-modulated turning in a physical, hexapedal robotic model, we aim to increase understanding of the role of leg stiffness and propose a bio-inspired control approach suitable for small, underactuated robots.

5.3 Experimental Setup

Experiments were recorded with high-speed video from an overhead camera (250fps, 8bit grayscale, 1280×1024px, AOS Technologies). The frame sequences were downloaded to a desktop computer in uncompressed RAW format and processed with the Python programming language using OpenCV [2] and the SciPy package [3]. The image data from the high-speed camera was used for 3D reconstruction of the robot's position and orientation in the environment.

5.3.1 Substrate

A 1m×1m sheet of 1/8 inch thick cork was fixed to the laboratory floor, and experiments were performed entirely on the cork's surface; running on cork reduces foot slippage. However, the cork also introduces an additional compliance into the system. Based on the experimentally determined value of the Young's modulus of cork reported in [37], 20 MPa, we can estimate an approximate stiffness for the cork substrate. Assuming a dynamic load of twice the full weight of the robot

supported by a single leg contacting over an area of one 1 mm^2, the approximate stiffness of the cork is 6500 N/m — more than two orders of magnitude larger than the typical leg compliance.

5.3.2 Leg Stiffness

For the turning experiments we adjust leg stiffness by replacing the middle leg fabricated from soft polyurethane rubber containing 20% plasticizer ($E \approx 10.7$MPa) by weight with a leg of the same geometry fabricated from the same polyurethane without plasticizer ($E \approx 18.2$ MPa). Flexural moduli for the two materials were determined experimentally using a standard end-loaded linear beam test.

5.3.3 Camera Calibration

Our goal was to use high speed video data to estimate the kinematic state of the robot during trials in order to better understand its dynamic interaction with the environment. In order to do this estimation from video data, the camera had be calibrated for the volume in which the robot runs. The more accurate the calibration, the more accurately kinematic parameters can be estimated from video data. The calibration process consisted of estimating parameters intrinsic to the camera (such as lens distortion and tangential skew) and extrinsic parameters, or those describing the transformation between world coordinates and camera coordinates.

Intrinsics

Before conducting experiments with the robot, multiple image sequences were recorded of a planar calibration chessboard (7×8 squares, 29mm per side) held in different poses covering the image plane. We model the camera as a pinhole with fourth order radial lens distortion and zero tangential skew. The intrinsic parameters were estimated by running the software described in [59] on our calibration sequences.

2D Extrinsics

To support estimation of the kinematic state of the running robot, we estimated the equation of the plane containing the cork surface in the camera's reference frame. To simplify the estimation, we restricted the chessboard to slide across the cork surface for one sequence of calibration images, eliminating out-of-plane rotation and translation. Adding this constraint allowed us to simultaneously estimate the cork plane together with the three-dimensional pose of the chessboard on the surface in each video frame using nonlinear least-squares. This approach was superior to fitting a plane to the 3D point cloud obtained by estimating the chessboard's pose independently in each sample.

3D Extrinsics

To extract three-dimensional trajectory data, we use a single camera viewing a scene from two perspectives; one view is direct, and the other passes through a slanted mirror. We jointly estimate the intrinsic camera parameters and extrinsic rigid transformation between the stereo pair using the software described in [59].

5.3.4 Tracking Geometry

Retro-reflective spheres (Vicon, Los Angeles, CA) were affixed to laminated strips of balsa wood glued to the robot's chassis; see Fig. 5.8. Aligning a pair of HMI lights (Super-Sun Gun 200W, Frezzolini) with the camera axis enabled segmentation of these spheres in videos via simple thresholding. The three-dimensional geometry of the spheres affixed to the robot was estimated using the two-camera setup described in Section 5.3.3 using a video of the robot translating through the field of view. The 3D location of each reflective sphere was estimated independently in each sample, then these observations were rigidly transformed to align about the origin. We then averaged these 3D locations to obtain an estimate of the geometry.

Figure 5.8: The robot chassis with rigid tracking geometry and retro-reflective spheres attached.

5.3.5 State Estimation

Using the calibrated cork surface and robot tracking geometry from Sections 5.3.3 and 5.3.4, it is possible to estimate the robot's rotations and planar position using pixel observations of the reflective spheres from a single overhead camera. We perform state estimation using an Unscented Kalman Filter (UKF) whose state is comprised of Euler rotations $(\theta_x, \theta_y, \theta_z)$ about the x, y, and z axes and planar position (x, y) (for theoretical details about the UKF, refer to [53]; for implementation details, see [81]).

5.4 Results

5.4.1 Running Speed

In both straight ahead running and turning, the top speed of the robot was estimated to be 1.4 m/s or 14 bodylengths/s. Fig. 5.9 shows the robot's running speed as a function of stride frequency for all trials including turning and straight running.

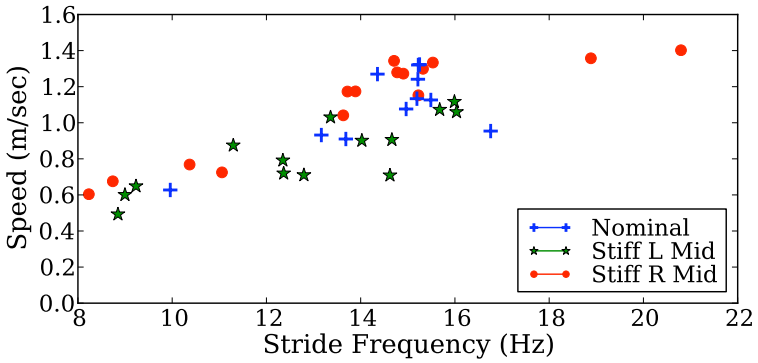

Figure 5.9: Forward speed vs. stride frequency

5.4.2 Cost of Transport

As we noted in the previous chapter, one performance metric for locomotion efficiency that's used among biologists is metabolic cost of transport. Recall that cost of transport is a measure of the total amount of energy required to move one kilogram of body mass one meter, and the millirobot, RoACH, has a "metabolic" cost of transport of more than 18,000 $J/Kg - m$.

To measure the metabolic cost of transport on DynaRoACH we measure the battery voltage

and the back EMF voltage while the robot is running. The difference of the two combined with the motor resistance determines the electrical power supplied to the motor simply from Ohm's law:

$$P_{electrical} = \frac{(V_{batt} - V_{emf})^2}{R_{motor}} \tag{5.10}$$

The electrical power consumed is divided by the product of the mass of the robot and its speed (as estimated from high speed video using the UKF) with the result being "metabolic" cost of transport. For the DynaRoACH robot, a plot of cost of transport at a variety of running speeds is shown in Fig. 5.10. Though it's biased by a larger number of samples at higher stride frequencies, we note that the mean metabolic cost of transport for the robot is around 3.5. This value is significantly lower than many other values reported in the literature recently [15] for small legged robots. Some possible explanations for such a low value include the very low-loss compliant transmission and well-tuned leg stiffness enabling dynamic energy storage and recovery.

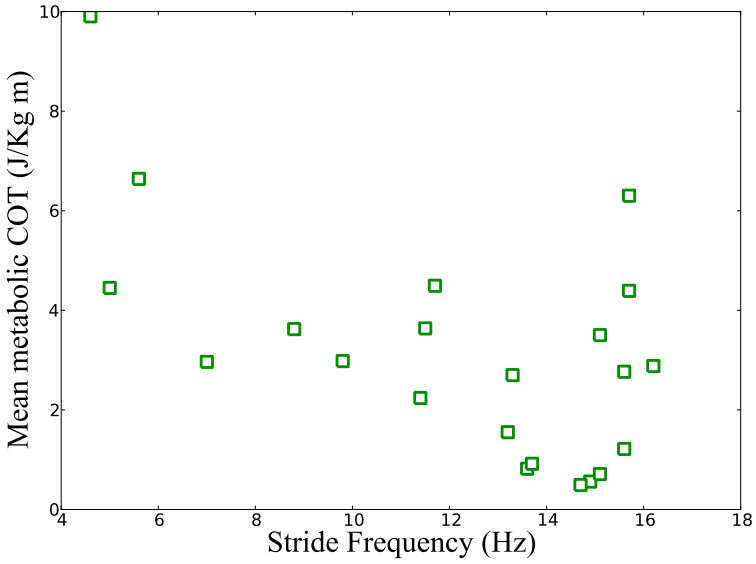

Figure 5.10: Metabolic cost of transport vs. stride frequency for the DynaRoACH robot.

5.4.3 Turning by Stiffness Control

Results from the study of turning in cockroaches suggest that all legs have the potential to contribute to dynamic turning. Small kinematic changes to the front leg were observed during turning maneuvers, while additional force production was required from the middle and hind legs to explain turning according to the simple dynamic model proposed in [52].

With the biological results in mind, we chose to adjust the stiffness of the middle leg in each tripod in order to affect turning. By increasing the stiffness of the middle leg, we reason that we can generate larger forces in that leg and induce a yaw torque that will cause the robot to turn.

With the stiffer leg in place, the robot was run over a smooth surface at a variety of speeds. The results from the turning experiments are shown in Figs. 5.11 and 5.12. Fig. 5.11 demonstrates that by stiffening the outside leg, we are able to consistently achieve turning in either direction. Qualitative examination of the figure, however, reveals that the robot turns more smoothly to the left than to the right, a fact that may be explained by small kinematic asymmetries in the robot's gait. Likewise, Fig. 5.12 shows that the maximum turning rate is relatively insensitive to stride frequency while there appears to be a wide scatter of turning rates possibly due to as yet unmodeled frequency-dependent dynamics. Data for the left turn show a mean turning rate of approximately 75 degrees per second, while the mean turning rate for right turns is approximately 50 degrees per second with significantly more variation in the data.

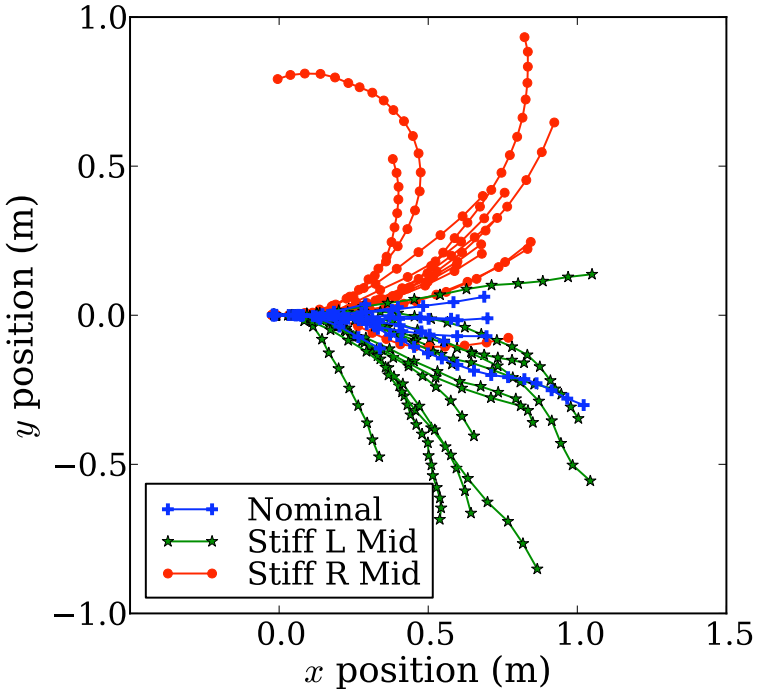

Figure 5.11: Summary data from all turning and straight running trials at 8-20Hz stride frequencies.

5.5 Adjustable Stiffness Leg Design

To actively initiate turning, we propose adjusting the stiffness of the middle leg on each side using shape memory alloy wire attached to the leg as shown in the CAD drawing in Fig. 5.13. The wire is 75 μm diameter Flexinol (Dynalloy, Tustin, California, USA) that is run from the hip down along the outside of the C, then turned around on a piece of plastic embedded in the leg material before running up along the C back to the hip, where it is connected to control electronics. Actuation of the SMA wire increases its modulus and decreases its length. The result is a significant increase in the area moment of inertia and, thus, the flexural rigidity of the whole leg.

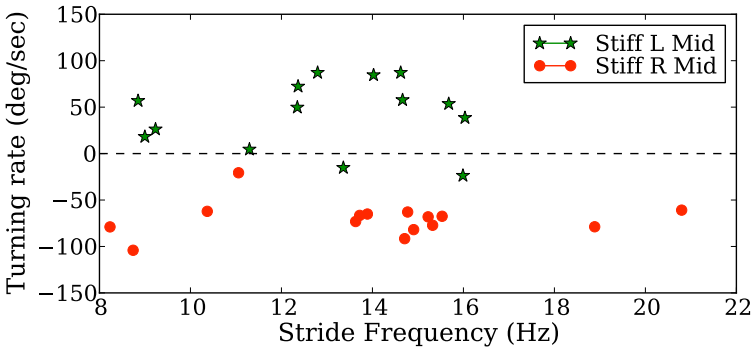

Figure 5.12: Turning rate vs. stride frequency

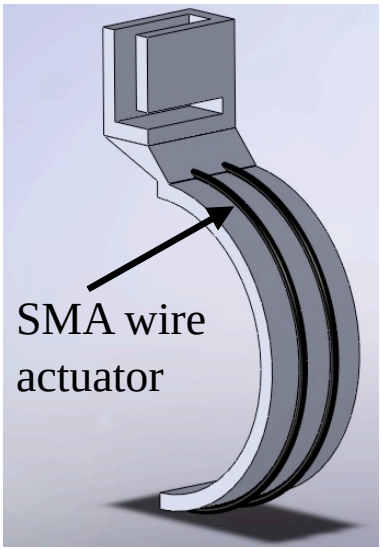

Figure 5.13: A CAD depiction of the compliant semi-circular leg with shape memory alloy wires running along the outside of the leg.

To verify that our design can achieve the same increase in stiffness as fabricating the legs without plasticizer, we tested the dynamic stiffness of a "soft" leg with an actuator attached using a muscle lever (300C, Aurora Scientific) to apply varying loads at frequencies in the range of the running frequencies the robot is capable of. Fig. 5.14 shows that at applied dynamic loads between 50mN and 80mN, the actuated leg is capable of matching or nearly matching the stiffness of the harder polyurethane. We are encouraged by this result as it demonstrates a clear integration path for active leg stiffness modulation.

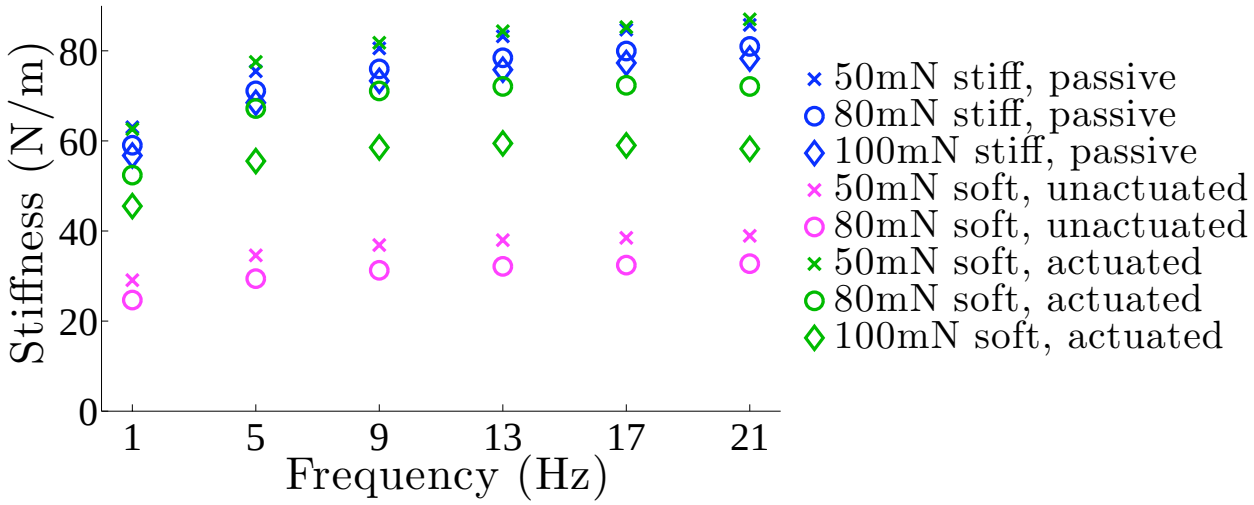

Figure 5.14: Experimental measurements of dynamic leg stiffness comparing a passive, "stiff" leg to a "soft" leg with an integrated shape memory alloy (SMA) wire actuator with applied dynamic loads of 50mN, 80mN, and 100mN.

5.6 Discussion

We demonstrated turning and rapid running in a small underactuated legged robot. Simply by stiffening the middle leg on the opposite side of the desired turn direction, we induced turning at rates of roughly 50 degrees per second to the right and 75 degrees per second to the left. At certain "troubling" stride frequencies, the robot dynamics were less predictable and hence turning behavior less repeatable; we believe that further kinematic refinements will help to reduce the frequency dependence.

Based on simple planar biological models for turning in hexapods, we anticipated that the middle leg would initiate turning. Although the model in [52] predicted that increasing the front leg stiffness would be most effective in causing turning, the middle leg gave better results for our robot. This inconsistency may arise simply due to differences in gait kinematics and scale between our robot and the cockroaches studied in [52]. In particular, our robot's limbs are significantly less sprawled than a cockroach's, possibly explaining the relatively large out-of-plane rotational dynamics reported in Tables 5.2 and 5.3. These dynamics, however, are not modeled in [52] or [71]. Fig. 5.15 shows the evolution of the pitch and roll rotations as a function of phase for a characteristic trial in which the robot turned as well as one in which it ran straight. For the turning trial, roll and pitch clearly oscillate antiphase, whereas, for straight-ahead trials, they appear to generally oscillate in phase. Consistent with aggregate data in Tables 5.2 and 5.3, the roll and pitch amplitudes are smaller for straight running. Altogether, these observations suggest that roll and pitch likely play a significant roll in the control of turning by adjusting leg stiffness.

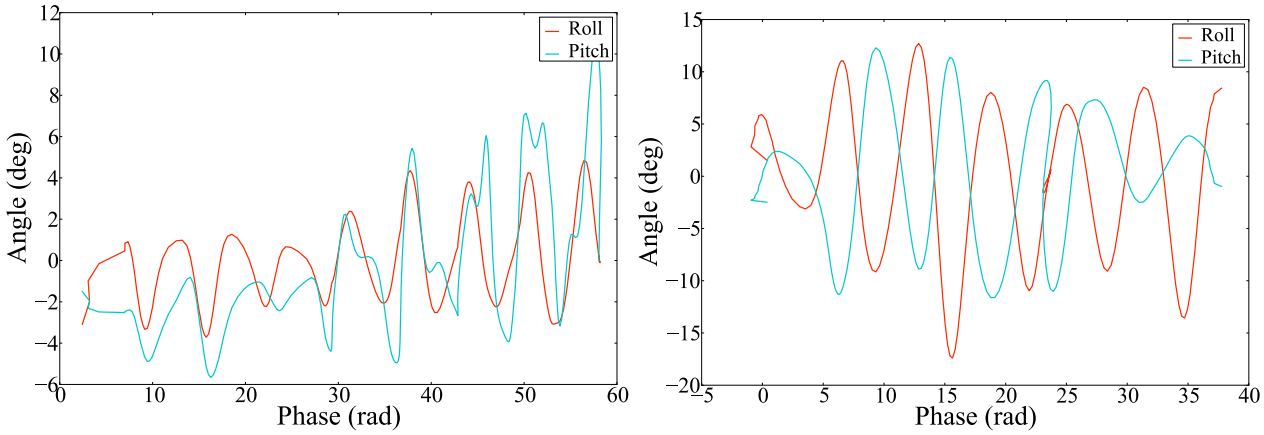

(a) (b)

Figure 5.15: Roll and pitch angle vs. phase for characteristic trials of (a) straight running at 13.5 Hz and (b) turning at 15 Hz

At specific stride frequencies, we observed rapid dynamic turns in which the robot turned $\approx 90^\circ$ over roughly 5 strides; see Fig. 5.17 for data from an illustrative trial. Of note is the fact that large instabilities in the robot's roll (rotation about the major body axis in the horizontal plane) and pitch (rotation about the body minor axis) correlate with the turns, settling out immediately following the execution of the maneuver. We believe this is an exciting result deserving of more study; the ability of a legged robot to reliably execute such sharp turns could enable extremely rapid navigation.

Our demonstration of consistent turning via modulation of leg stiffness has implications for biomechanics research. Since it is extremely easy to adjust leg stiffness by simply replacing the leg, the robot can support systematic studies of the parametric dependence of maneuverability. We have already provided preliminary experimental validation for the turning predictions from simple models like LLS, since we obtain substantial turning rates using the predicted scales of stiffness adjustment. One interesting future direction is to extend this result by carefully characterizing the connection between the lumped-element parameters in (for example) LLS and the design parameters of the physical robot.

Stride Frequency	Min. Roll	Max. Roll	Min. Pitch	Max. Pitch
10-15Hz	-7±3°	9±4°	-6±4°	7±3°

Table 5.2: Roll and pitch angle statistics for n=14 straight-running trials

Stride Frequency	Min. Roll	Max. Roll	Min. Pitch	Max. Pitch
5-10 Hz	-14±3°	13±2°	-10±2°	11±2°
10-15Hz	-10±6°	10±7°	-9±4°	8±4°
15-20Hz	-10±8°	9±6°	-10±5°	10±5°

Table 5.3: Roll and pitch angle statistics for n=31 turning trials

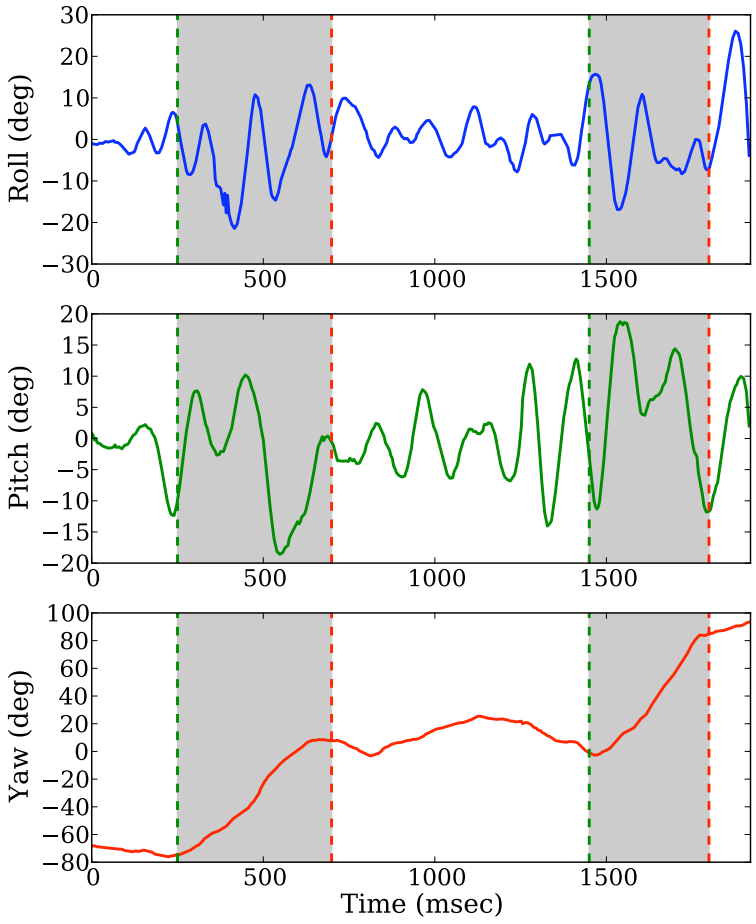

Figure 5.16: Angular orientation for the robot during dynamic turns. Note increases in roll and pitch magnitudes corresponding to sudden changes in yaw.

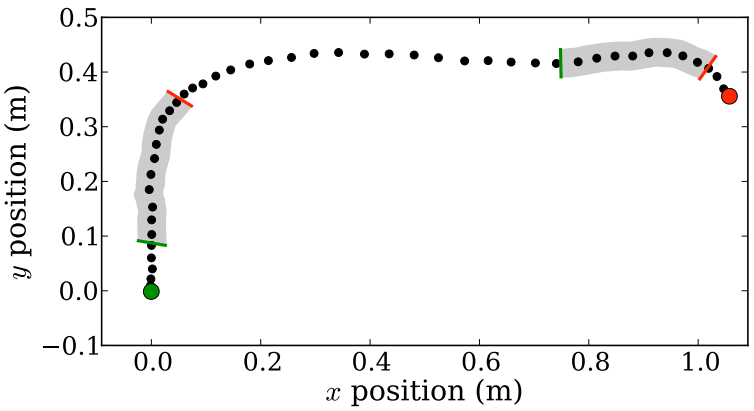

Figure 5.17: Position data for the robot during a series of dynamic turns. The time interval between markers is 2.5ms and the stride frequency is approximately 13 Hz.

Part IV

Conclusions and Appendices

Chapter 6

Conclusions

This work has explored the potential for designing legged robots at the milli- and meso-scales using the folded compliant mechanisms produced by the smart composite microstructures process and its analog scaled prototyping process. We've developed a spatial, strain energy-based approach to modeling and assessing the stiffness properties of parallel compliant mechanisms and experimentally demonstrated its ability to improve our designs through kinematic redundancy. We have also designed and built two autonomous legged robots at the milli- and meso-scales using SCM and scaled prototyping, respectively. To our knowledge, the 2.4g RoACH robot is the smallest legged robot to date capable of untethered, sustained, steerable locomotion. With the 24g DynaRoACH robot we have reduced actuation requirements to a single DC motor and improved efficiency through dynamic operation. The minimally actuated DynaRoACH design has also demonstrated the potential for controlled turning as well as highly dynamic maneuvers using the biologically inspired approach of modulating leg stiffness.

6.1 Future Work

However, even with the accomplishments in this dissertation, we have only begun to scratch the surface of what is possible with SCM (and its scaled prototyping analog) and power-dense, small-scale legged robots. Much work remains to be done to improve the capabilities of these robots as well as the tools used to design and fabricate them.

6.1.1 Improved Design Tools

Folded SCM mechanisms are a relatively new approach to designing and fabricating robots at the milli- and meso-scales. Their combination of kinematic mechanism design, compliant mecha-

nism theory, composite materials, and planar fabrication make them difficult to model in a unified way using existing computer-aided design (CAD) tools. Linkage synthesis and analysis software can be helpful in the kinematic design process, and finite element software is useful for ensuring that structural loads don't exceed maximum allowable stresses. Where fabrication is concerned, two-dimensional representations suitable for manufacturing on a laser-machining system can be produced using any number of drafting packages. However, no ability exists yet for the folded robot designer to synthesize a three-dimensional design directly, analyze it structurally or kinematically, and generate an unfolding that can then be manufactured automatically.

It is this manual translation of a folded design to a suitable 2D representation that is error prone and necessitates the scaled prototyping process in Appendix A. In the absence of effective computer aided design tools for these robots, the best tool for design evaluation is still a functional prototype that can be realized in less than an hour.

6.1.2 Integration of Electronics into Robot Structure

Printed circuit board and folded robot fabrication share a very important property - they are both planar. Integration of electronics with our existing folded robots is almost an afterthought in its current state. As robots get smaller and more dynamic, their performance becomes much more sensitive to mass distribution. Having the ability to integrate electronics (as the Microrobotics group at Harvard has begun to do [23]) and potentially even batteries into the robot structure would greatly simplify design and improve overall robustness. With integrated electronics, robots could be more easily ruggedized for operation in harsh or aquatic environments if necessary.

6.1.3 Dynamic Characterization and System ID

Clearly, from the results in Chapter 5, a great deal of interesting behavior is embedded in the dynamics of the DynaRoACH robot. Though we have proven the viability and capability of the design and shown the potential for turning control with small changes to leg stiffness, the full underactuated dynamics are not yet well understood. Reduced order models like SLIP [16] and LLS [76] are useful for providing insight into the dynamic behavior of animals and potentially robots, but mapping predictions from the model to the vastly more complicated physical system is difficult if not currently impossible.

One interesting approach to improving our understanding of these dynamic systems is the notion of "fitting" their dynamics to existing models in order to close the loop between model and design parameters like leg stiffness, stride frequency, leg morphology, etc. This is a very challenging problem, and its solution is far from clear. A combination of experimental techniques from biology like 3D motion capture and simultaneous ground reaction force measurements combined with engineering techniques from system identification could begin to shed light on the underlying dynamics of these systems.

6.1.4 Dynamic Climbing

The high power density of small SCM-based robots makes them ideal for challenging locomotion modes like dynamic vertical or inverted climbing. With a better understanding of their dynamics and current advances in adhesion technology [56][61], legged millirobots could make very effective, dynamic climbing platforms opening up a large space of applications in exploration, search and rescue, and structural monitoring.

6.1.5 Robots as Platforms for Testing Biological Hypotheses

Finally, perhaps one of the most exciting applications of these small SCM robots is at the interface of integrative biology and robotics. The ease with which robot designs can be modified and fabricated makes the scaled SCM process ideal for quickly generating a variety of morphologies to help test hypotheses about animal locomotion performance.

While this dissertation has hopefully made some progress toward the goal of realizing capable legged locomotion at the scale of a cockroach, we are clearly still very far from being able to produce the truly awesome locomotion capabilities that we see in these remarkable insects. We can only hope that some ideas contained in this work will inspire current and future engineers and biologists to take up the mantle and produce new approaches that will help us create insect-like locomotion in robotic platforms.

Appendix A

A Scaled Prototyping Process for Folded Millirobots

In this appendix we introduce an exact scaled version of the smart composite microstructure (SCM) process [91] that enables the millirobot designer to produce functional scaled prototypes of a robot design. The process utilizes very low cost, so-called "green" materials and allows for the physical realization of a robot prototype in less than one hour for the basic structure without wiring or actuators at a cost of less than $1 per robot. While the material costs for an SCM robot are similar, the speed of the SCM process is fundamentally limited by composite cure times, laser micro-machining times, and difficult hand assembly of very small structures. However, by closely mimicking the SCM process, we enable the designer to produce accurate macro models at anywhere from a 2-10$\times$ scale so that kinematic and static loading conditions can be explored quickly with a hands-on model. The speed and negligible material cost of the process significantly shorten the design cycle for an SCM-based millirobot.

For an overview of the SCM process we refer the reader to Chapter 3. In the following sections, we enumerate the steps necessary to produce scaled prototypes, briefly review design rules adapted from the SCM process for folded, flexure-based robots, and discuss the effects of scaling on the overall performance of a prototype.

A.1 Process Overview

A.1.1 The Prototyping Process

The macro-scale prototyping process closely follows the SCM process, but instead of pre-impregnated composite fiber laminate, we substitute lightweight, double sided coated posterboard (Nature Saver posterboard, available from Officemax.com). For the polyimide flexure layer, we substitute a thicker polyethylene terephalate (PET) film because thermal compatibility of the film is less of a concern than in the SCM process. In addition, the PET is less inert so it bonds better to various adhesive polymers. Just as in the SCM process, the posterboard is cut using a precision laser (VersaLaser VL200) according to a 2-dimensional design drawing. However, unlike with carbon fiber composites, the posterboard can be easily cut with an infrared laser. The steps for the prototyping process are outlined below with the step numbers corresponding to Fig. A.2:

1. The process begins with a sheet of posterboard.
2. Gaps are laser-cut into the posterboard where flexures will be in the final structure.
3. Two layers of adhesive polymer with one layer of flexural polymer (high melting point) are placed between two sheets of posterboard.
4. The resulting structure is rolled through heated rollers to apply pressure and melt the adhesive layers, bonding the structure.
5. Outlines of parts are then laser cut, releasing the parts from the original sheet.

Because the posterboard itself, unlike pre-impregnated composites, contains no adhesive, a simple thermoset polymer film for the flexure layer is insufficient. We must either add adhesive layers separately, or use a polymer film with an integrated adhesive to bond the structure. A carrier film with integrated adhesive is convenient because it's essentially monolithic. However, the standard thicknesses of such films limit the ability of the designer to change the stiffness of flexure hinges by using different thickness films. While it is possible to use more than one layer of such a film, the interaction of the adhesive layers between the carrier film layers creates a noticeable viscoelastic response from the flexure hinges. In order to retain the flexibility for the designer in the choice of flexure thickness, we have chosen to add a separate adhesive between the posterboard and the flexure film. For the the flexure film we use 50 or 75μm PET depending on the desired flexure stiffness. For the adhesive layer we use either UHU ^{TM}glue stick which is a gel-based polyacrylate adhesive, or we pre-laminate the inner faces of the workpieces with hot-mount thermal adhesive.

This prototyping method is appropriate for fabricating entire functional robots or simply mocking up a small mechanism to be integrated into a larger robot design. The hexapod crawler design presented in Chapter 4 highlights the difficulty of visualizing a complicated 3D mechanism that

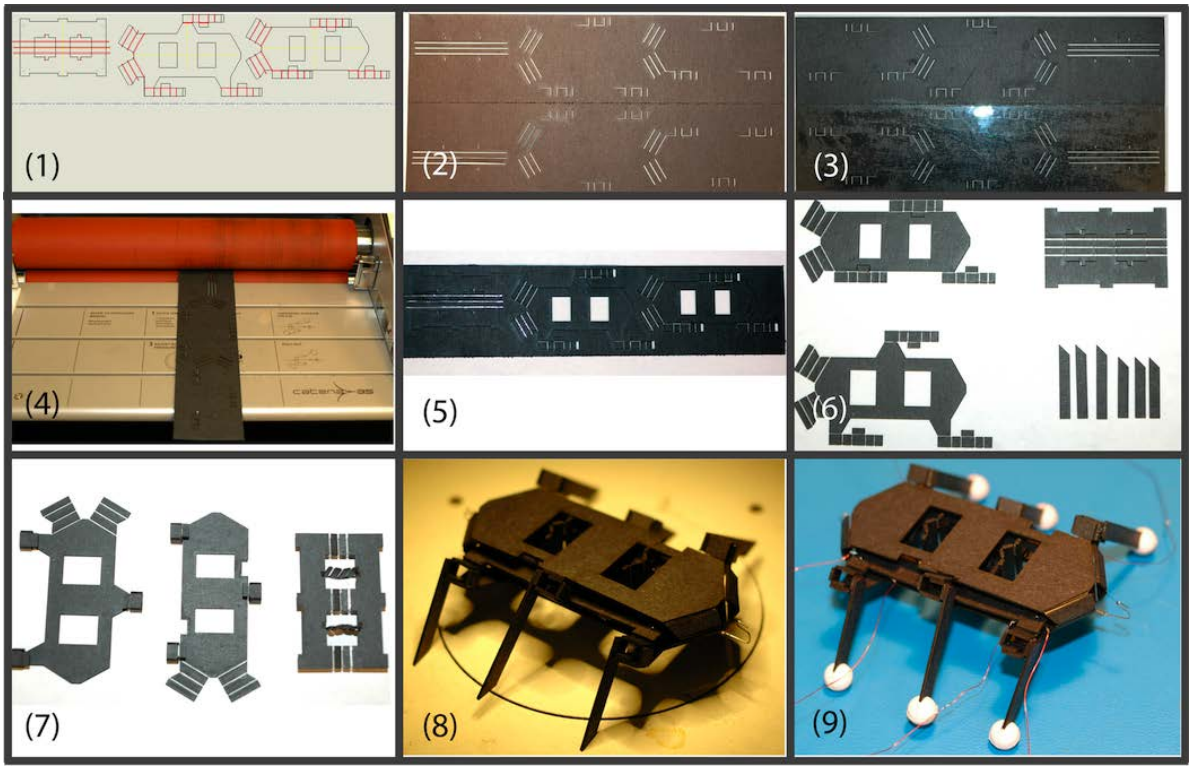

Figure A.1: Steps for prototyping a hexapod crawling robot: **(1)** A 2-dimensional drawing is made in a vector-based illustration program (Solidworks). **(2)** A blank piece of posterboard with a pre-cut fold line is folded and placed in a laser cutter, and the flexure cuts are made in both layers. **(3)** The workpiece is removed and adhesive is applied to both sides inside the fold. A 50 μm film of PET is sandwiched between the two sides of the fold. **(4)** The workpiece is fed through heated rollers at 230°F at a low speed (approx. 5 mm/sec). **(5)** The workpiece is placed back in the laser cutter and outlines of the parts are cut out. **(6)** Parts are released from the workpiece. **(7)** Individual linkages can be folded up in place. The three joints on the two leftmost pieces are fourbars used as hips. The joints in the rightmost piece form two Sarrus linkages when two are folded and glued out of plane. **(8)** The three plates are joined such that the hips for one tripod sit above the central plate while the hips for the other sit below, and the legs are attached to the hip fourbars. **(9)** SMA actuators are attached and wired in place and spherical PDMS feet are added.

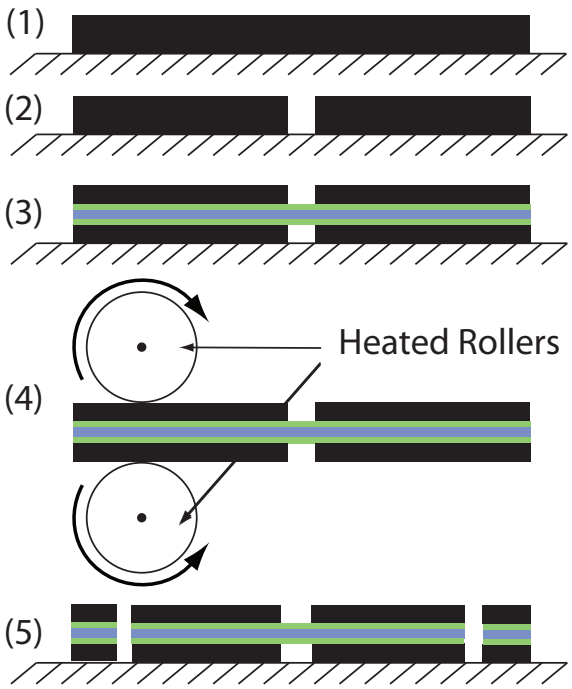

Figure A.2: A step-by-step illustration of the posterboard link and hinge fabrication process

results from folding a 2D design. The posterboard prototyping process enables the designer to quickly try out a folded design and explore features such as alignment tabs or self-jamming flexures that can aid significantly in the assembly process. In addition, because the goal of the prototyping process is to produce a large-scale model of a robot that will ultimately be fabricated using anisotropic, directional composites, the prototype can be used to explore folding approaches that ensure that the composite fibers are properly oriented for the loading conditions that will be imposed on the robot. For example, fiber direction should be perpendicular to any movable flexures because the composite laminate is very weak in bending about the fiber axis compared to bending about the axis transverse to fiber direction.

A.1.2 Flexure Design

It is important to address the issue of scaling in order to effectively use the prototypes for predicting mechanism behavior at the small scale. Ideally we would like to develop a scaling law that can be used to prototype at any scale. There are two parameters in which we're interested - the flexure hinge behavior and the stiffness of the structural members or links.

Simple design rules based on modeling flexures using the pseudo-rigid-body model presented in [47] are outlined in [91]. In short, to mostly closely match the behavior of an ideal pin joint, the ratio of the axial stiffness of the flexure to its rotational stiffness should be maximized. This

objective is subject to geometric constraints imposed by the maximum elastic strain sustainable in the flexures as well as the maximum angle of rotation of the flexure before the edges of the rigid links on opposite sides make contact and jam given by:

$$\phi_{max} = \frac{l}{t} \tag{A.1}$$

Eqn. A.1 is an important constraint when using the fast scale prototyping process. One limitation of the process is that the posterboard is available only in discrete thicknesses. The material used in our prototypes is approximately 6 times thicker than the true scale material. The implication is that this constraint will be stronger at the larger scale. Thus, we must take care in using the design equations from [91] to design the large scale flexures.

A.1.3 Compensation for Laser Dimensions

In some cases it is important to have an accurate prediction of joint stiffness and range of motion. For example, when specifying required force to actuate a linkage built using the scaled prototyping process, accurate knowledge of individual joint stiffness allows the designer to calculate an effective mechanism stiffness. Likewise, some designs require so-called "sacrificial" flexures that bend exactly to a specific angle and are then fixed with a permanent adhesive. This approach is very convenient for creating desired geometry. In both cases, it's important for the designer to know the relationship between drawn dimensions and the true resultant size of the part. Because the laser beam used to cut the cardboard has some fixed dimension, design drawings must compensate for its size. In addition, because of beam divergence the sidewalls of laser cuts are not vertical as shown in Fig. A.3, and this effect can also have an impact on design functionality. Fig. A.4 shows the relationship between the true flexure length and its length dimension in the design drawing, while Fig. A.5 shows the relationship between true flexure length and angle at which the flexure "jams" or no longer admits rotation.

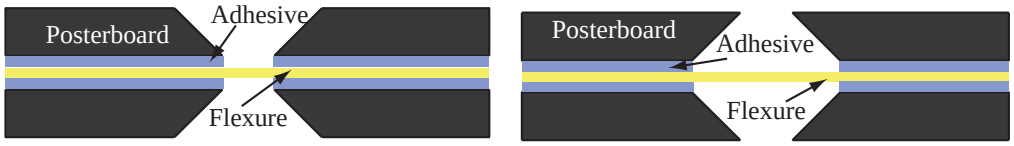

(a) A flexure in which the initial cuts were performed with inner adhesive faces down.

(b) A flexure in which the initial cuts were performed with the inner adhesive faces up.

Figure A.3: Effect of workpiece orientation on flexure geometry. Cut sidewall angles are exaggerated for effect.

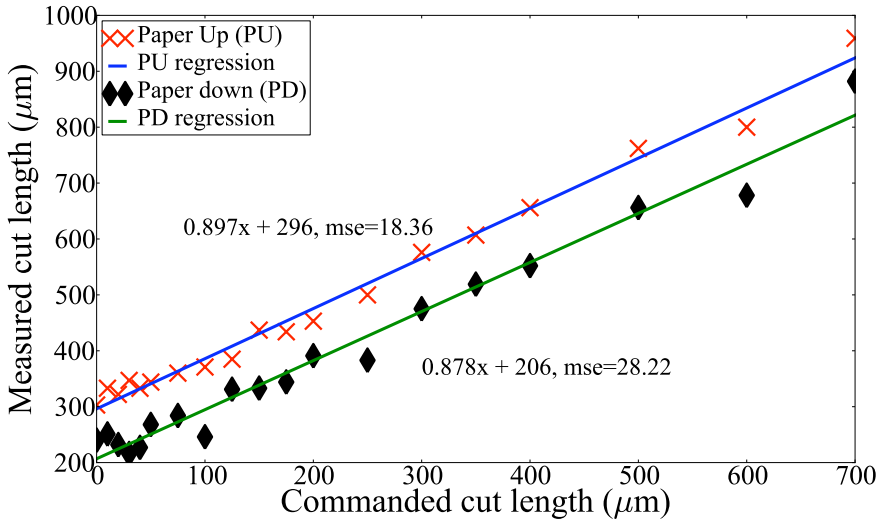

Figure A.4: Relationship between the flexure cut length in the design drawing and the resulting artifact. Posterboard was cut with thermal adhesive liner paper face up (PU) and face down (PD).

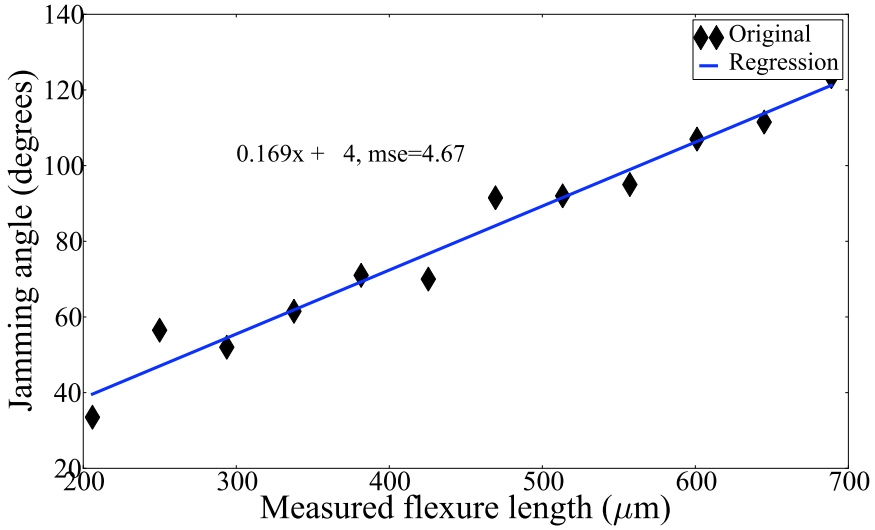

Figure A.5: Flexure jamming angle as a function of the true flexure length for 440 μm thick posterboard with a 25 μm flexure layer.

Linear regressions were performed on both the flexure length and jamming angle data in Figs. A.4 and A.5 to provide the prototype designer with a simple calculation to estimate true flexure dimensions and jamming angles.

A.1.4 Developing a Scaling Law

In order to scale the rigid members of a design, we must formulate a way of relating the material properties and geometry of a structure built at the small scale to those of the scaled structure. Because the materials used at the different scales are so different, we propose a dimensionless parameter to relate the actual size structure to the scaled prototype as follows:

$$\xi = \frac{kl_c}{g \cdot m} \tag{A.2}$$

where k is the stiffness of a characteristic link in bending, l_c is a characteristic length, and mg is the weight of the entire structure. This formulation comes from using structural stiffness vs. weight as a performance metric. This dimensionless parameter is also based on the implicit assumption that the robot is operating under quasi-static conditions. For a dynamic scenario, it would be preferable to use a characteristic load rather than the weight of the robot in the denominator. It is our aim to use this ratio as a guide in designing scaled prototypes of folded millirobots. That is, robotic structures at the macro scale will perform similarly to their true scale counterparts in terms of stiffness-to-weight ratio if they have similar values for ξ. In following section, we compare the values of ξ for both the scaled prototype and the milli-scale 2.4g hexapedal robot design in Chapter 4.

A.2 Comparison of Scaled Prototype to RoACH Millirobot

In this section, we use the example of the hexapod crawling robot from Chapter 4 to demonstrate the prototyping process and verify our scaling law.

Based on the two robot skeletons depicted in Fig. A.6 we can begin to compare the 2× prototype to the true scale version using the scaling law proposed above. The characteristic link we will use to determine the stiffness, k, is the leg link. We will use the leg length as our characteristic length, l_c. To determine the bending stiffness of each leg (posterboard and composite) the leg was clamped at one end and subjected to a known load at the free end. The tip displacement was observed with a video camera and measured on screen at a zoom of approximately 32×. Using these measurements we can compute the value of ξ for both the 2× scale prototype and the composite fiber structure. The measurements and results are summarized in Table A.1.

The value of ξ for the 2× prototype is within 30% of the value for the composite fiber structure. In fact, the value of ξ for the 2× prototype is higher than for the true scale model. This indicates that the prototype may, in fact, be overpredicting the performance of the composite. This discrepancy

Table A.1: Comparison of a 2× posterboard prototype to S-2 glass fiber composite using Eqn. A.2

	Posterboard	**S-2 Glass**
l_c	22 mm	11 mm
b (width)	5 mm	2.5 mm
h (thickness)	0.875 mm	0.15 mm
$P_{applied}$	0.01 N	0.01 N
$\delta_{observed}$	80 x 10^{-6} m	665 x 10^{-6} m
$K_{bending}$	125 $\frac{N}{m}$	66.5 $\frac{N}{m}$
m·g	4.6 x 10^{-2} N	3.2 x 10^{-3} N
ρ	750 $\frac{Kg}{m^3}$	2400 $\frac{Kg}{m^3}$
$E_{(11)}$	30 GPa	43 GPa
ξ	84.5	61.1

can be at least partly explained by the fact that the elastic modulus of paper used in the prototypes has been estimated to be on the same order as that for the S-2 glass [69] - approximately 30GPa. In addition, the posterboard is a factor of 3 less dense than the S-2 glass. To even more closely match the prototype to the true scale we could reduce the thickness of the leg links or increase the scaling factor slightly to approximately 2.4×.

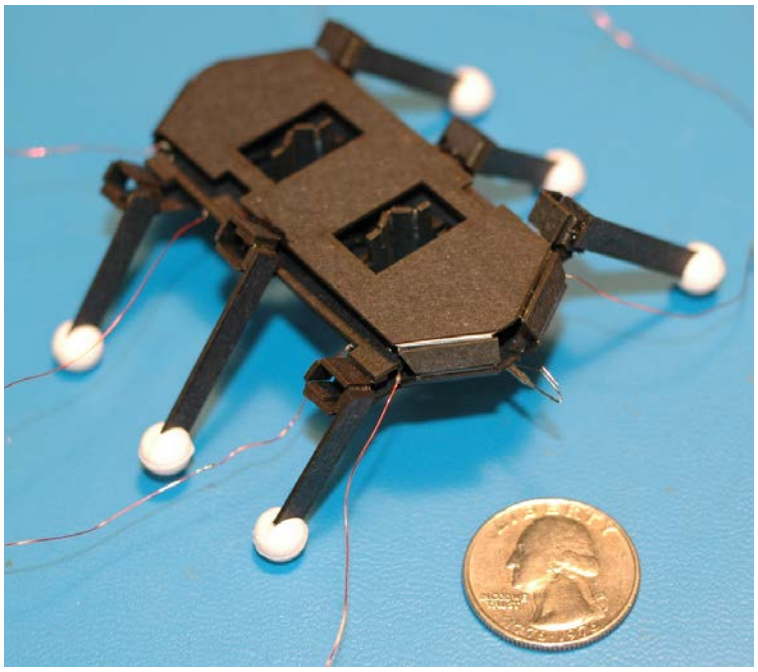

(a) 2× posterboard crawler model

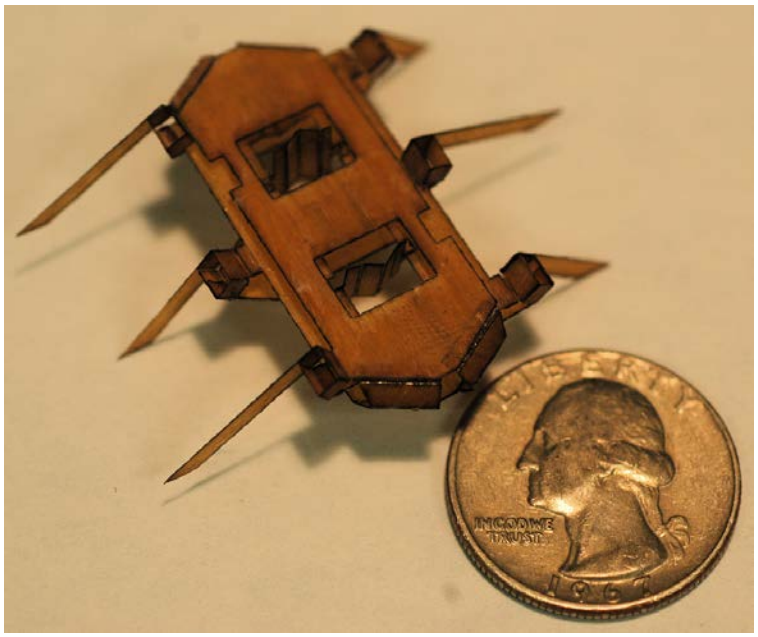

(b) True scale S-2 glass crawler structure

Figure A.6: The scaled prototype structure with actuators integrated and the actual size crawler structure (without actuators or wiring)

References

[1] [Online]. Available: http://dynalloy.com/TechSheets.shtml

[2] [Online]. Available: http://opencvlibrary.sourceforge.net

[3] [Online]. Available: http://www.scipy.org

[4] R. M. Alexander, *Size and Shape*. Edward Arnold, 1971.

[5] ——, *Perspectives in Experimental Biology*. Pergamon, 1976, ch. Mechanics of bipedal locomotion.

[6] ——, "Optimization and gaits in the locomotion of vertebrates," *Physiol. Rev.*, vol. 69, no. 4, pp. 1199–1227, 1989. [Online]. Available: http://physrev.physiology.org

[7] ——, *Principles of Animal Locomotion*. Princeton University Press, 2003.

[8] R. Altendorfer, N. Moore, H. Komsuoglu, M. Buehler, H. B. B. Jr., D. McCordie, U. Saranli, R. J. Full, and D. E. Koditschek, "RHex: A biologically inspired hexapod runner," *Autonomous Robots*, vol. 11, no. 3, pp. 207–213, November 2001.

[9] S. Avadhanula, "The design and fabrication of the MFI thorax based on optimal dynamics," Master's thesis, University of California, Berkeley, 2001.

[10] S. Avadhanula, R. J. Wood, and R. S. Fearing, "Dynamically tuned design of the MFI thorax," in *IEEE Int. Conf. on Robotics and Automation*, Washington, D.C., 2002.

[11] S. Awtar and A. Slocum, "Design of parallel kinematic xy mechanisms," in *Proceedings of the ASME International Design Engineering Technical Conferences*. American Society of Mechanical Engineers, Sept. 2005, pp. 89–99.

[12] A. T. Baisch and R. J. Wood, "Design and fabrication of the Harvard Ambulatory Micro-Robot," in *Int. Symposium on Robotics Research*, Lucerne, Switzerland, 2009.

[13] S. Bergbreiter, "Design of an autonomous jumping robot," in *IEEE Int. Conf. on Robotics and Automation*, Rome, Italy, April 2007.

[14] F. G. Bermudez and R. S. Fearing, "Optical flow on a flapping wing robot," in *Intl Conf on Intelligent Robots and Systems*, St. Louis, MO, 2009, pp. 5027–5032.

[15] P. Birkmeyer, K. Peterson, and R. S. Fearing, "Dash: A dynamic 16g hexapedal robot," in *IEEE Int. Conf. on Intelligent Robots and Systems*, St. Louis, MO, 2009.

[16] R. Blickhan, "The spring-mass model for running and hopping," *J. Biomechanics*, vol. 22, pp. 1217–1227, 1989.

[17] R. Blickhan and R. J. Full, "Similarity in multilegged locomotion: Bouncing like a monopode," *J. Comp. Physiol A*, vol. 173, no. 5, pp. 509–517, November 1993.

[18] A. Boxerbaum, J. Oro, G. Peterson, and R. Quinn, "The latest generation Whegs™; robot features a passive-compliant body joint," in *Intelligent Robots and Systems, 2008. IROS 2008. IEEE/RSJ International Conference on*, Nice, France, Sept. 2008, pp. 1636 –1641.

[19] D. Campbell and M. Buehler, "Stair descent in the simple hexapod 'rhex'," in *Robotics and Automation, 2003. Proceedings. ICRA '03. IEEE International Conference on*, vol. 1, Taipei, Taiwan, Sept. 2003, pp. 1380 – 1385.

[20] G. A. Cavagna, N. C. Heglund, and C. R. Taylor, "Mechanical work in terrestrial locomotion: two basic mechanisms for minimizing energy expenditure," *Am J Physiol Regul Integr Comp Physiol*, vol. 233, no. 5, pp. 243–261, 1977.

[21] J. G. Cham, S. A. Bailey, J. E. Clark, R. J. Full, and M. R. Cutkosky, "Fast and robust: Hexapedal robots via shape deposition manufacturing," *The International Journal of Robotics Research*, vol. 21, no. 10-11, pp. 869–882, 2002. [Online]. Available: http://ijr.sagepub.com/cgi/content/abstract/21/10-11/869

[22] Y. Chen and J. McInroy, "Estimation of symmetric positive-definite matrices from imperfect measurements," *Automatic Control, IEEE Transactions on*, vol. 47, no. 10, pp. 1721–1725, Oct 2002.

[23] K.-J. Cho, E. Hawkes, C. Quinn, and R. Wood, "Design, fabrication and analysis of a body-caudal fin propulsion system for a microrobotic fish," in *Robotics and Automation, 2008. ICRA 2008. IEEE International Conference on*, May 2008, pp. 706–711.

[24] M. Culpepper and G. Anderson, "Design of a low-cost nano-manipulator which utilizes a monolithic, spatial compliant mechanism," *Precision Engineering*, vol. 28, no. 4, pp. 469–482, Oct. 2004.

[25] T. J. Dawson and R. C. Taylor, "Energetic cost of locomotion in kangaroos," *Nature*, vol. 246, no. 5431, pp. 313–314, 1973. [Online]. Available: http://dx.doi.org/10.1038/246313a0

[26] F. DELCOMYN, "The effect of limb amputation on locomotion in the cockroach periplaneta americana," *J. Exp. Biol.*, vol. 54, no. 2, pp. 453–469, 1971. [Online]. Available: http://jeb.biologists.org/cgi/content/abstract/54/2/453

[27] F. Delcomyn, "The locomotion of the cockroach periplaneta americana," *J Exp Biol*, vol. 54, no. 2, pp. 443–452, 1971. [Online]. Available: http://jeb.biologists.org/cgi/content/abstract/54/2/443

[28] T. Ebefors, J. U. Mattsson, E. Kalvesten, and G. Stemme, "A walking silicon micro-robot," in *10th Intl Conf on Solid-State Sensors and Actuators*. Japan: IEEE, 1999, pp. 1202–1205.

[29] E. D. Fasse and P. C. Breedveld, "Modeling of Elastically Coupled Bodies: Part I—General Theory and Geometric Potential Function Method," *Journal of Dynamic Systems, Measurement, and Control*, vol. 120, no. 4, pp. 496–500, 1998. [Online]. Available: http://link.aip.org/link/?JDS/120/496/1

[30] R. S. Fearing, "Survey of sticking effects for micro parts handling," in *IEEE Int. Conf. on Intelligent Robots and Systems*, 1995.

[31] S. N. Fry, R. Sayaman, and M. H. Dickinson, "The Aerodynamics of Free-Flight Maneuvers in Drosophila," *Science*, vol. 300, no. 5618, pp. 495–498, 2003. [Online]. Available: http://www.sciencemag.org/cgi/content/abstract/300/5618/495

[32] R. J. Full, "Mechanics and energetics of terrestrial locomotion: Bipeds to polypeds," in *Energy transformations in cells and organisms*, W. Wieser and E. Gnaiger, Eds., 1989.

[33] R. J. Full and M. S. Tu, "Mechanics of a rapid running insect: 2-legged, 4-legged, and 6-legged locomotion," *J. exp. Biol.*, vol. 156, pp. 215–231, Mar. 1991.

[34] K. Galloway, J. Clark, and D. Koditschek, "Design of a tunable stiffness composite leg for dynamic locomotion," in *ASME IDETC/CIE*, 2009.

[35] J. M. Gere and S. P. Timoshenko, *Mechanics of Materials*, 3rd ed. PWS, 1990.

[36] R. M. Ghigliazza, R. Altendorfer, P. Holmes, and D. Koditschek, "A simply stabilized running model," *SIAM Review*, vol. 47, no. 3, pp. 519–549, 2005. [Online]. Available: http://link.aip.org/link/?SIR/47/519/1

[37] L. J. Gibson, K. E. Easterling, and M. F. Ashby, "The structure and mechanics of cork," *Proceedings of the Royal Society of London. Series A, Mathematical and Physical Sciences*, vol. 377, no. 1769, pp. 99–117, 1981. [Online]. Available: http://www.jstor.org/stable/2397034

[38] M. Goldfarb, M. Gogola, G. Fischer, and E. Garcia, "Development of a piezoelectrically-actuated mesoscale robot quadruped," *J. of Micromechatronics*, vol. 1, no. 3, pp. 205–219, July 2001.

[39] L. C. Hale, "Principles and techniques for designing precision machines," Ph.D. dissertation, Massachusetts Institute of Technology, February 1999.

[40] N. Heglund, G. Cavagna, and C. Taylor, "Energetics and mechanics of terrestrial locomotion. III. Energy changes of the centre of mass as a function of speed and body size in birds and mammals," *J Exp Biol*, vol. 97, no. 1, pp. 41–56, 1982. [Online]. Available: http://jeb.biologists.org/cgi/content/abstract/97/1/41

[41] J. A. Hetrick, N. Kikuchi, and S. Kota, "Robustness of compliant mechanism topology optimization formulations," V. V. Varadan, Ed., vol. 3667, no. 1. SPIE, 1999, pp. 244–254. [Online]. Available: http://link.aip.org/link/?PSI/3667/244/1

[42] J. K. Hodgins and M. H. Raibert, "Biped gymnastics," *The International Journal of Robotics Research*, vol. 9, no. 2, pp. 115–128, 1990. [Online]. Available: http://ijr.sagepub.com/cgi/content/abstract/9/2/115

[43] S. Hollar, A. Flynn, C. Bellew, and K. S. J. Pister, "Solar powered 10mg silicon robot," in *IEEE MEMS*, 2003.

[44] A. M. Hoover and R. S. Fearing, "Fast scale prototyping for folded millirobots," in *IEEE Int. Conf. on Robotics and Automation*, Pasadena, CA, 2008.

[45] A. M. Hoover, E. Steltz, and R. S. Fearing, "Roach: An autonomous 2.4g crawling hexapod robot," in *IEEE Int. Conf. on Intelligent Robots and Systems*, Nice, France, Sept. 2008.

[46] A. Hoover and R. Fearing, "Analysis of off-axis performance of compliant mechanisms with applications to mobile millirobot design," in *Intelligent Robots and Systems, 2009. IROS 2009. IEEE/RSJ International Conference on*, oct. 2009, pp. 2770 –2776.

[47] L. L. Howell, *Compliant mechanisms*. John Wiley & Sons, 2001.

[48] L. L. Howell and A. Midha, "A method for the design of compliant mechanisms with small-length flexural pivots," *Journal of Mechanical Design*, vol. 116, no. 1, pp. 280–290, 1994. [Online]. Available: http://link.aip.org/link/?JMD/116/280/1

[49] http://www.hexbug.com. [Online]. Available: http://www.hexbug.com

[50] J. E. Huber, N. A. Fleck, and M. F. Ashby, "The selection of mechanical actuators based on performance indices," *Proceedings: Mathematical, Physical and Engineering Sciences*, vol. 453, no. 1965, pp. 2185–2205, 1997. [Online]. Available: http://www.jstor.org/stable/53045

[51] D. J. Irschick, C. C. Austin, K. Petren, R. N. Fischer, J. B. Losos, and O. Ellers, "A comparative analysis a comparative analysis of clinging ability among pad-bearing lizards." *Biol. J. Linn. Soc.*, vol. 59, no. 21-35, 1996.

[52] D. Jindrich and R. Full, "Many-legged maneuverability: dynamics of turning in hexapods," *J Exp Biol*, vol. 202, no. 12, pp. 1603–1623, 1999. [Online]. Available: http://jeb.biologists.org/cgi/content/abstract/202/12/1603

[53] S. J. Julier and J. K. Uhlmann, "New extension of the Kalman filter to nonlinear systems," I. Kadar, Ed., vol. 3068, no. 1. SPIE, 1997, pp. 182–193.

[54] J. M. Kahn, R. H. Katz, and K. S. J. Pister, "Next century challenges: mobile networking for "smart dust"," in *Proc. ACM/IEEE Int. Conf. on Mobile Computing and Networking*. New York, NY, USA: ACM Press, 1999, pp. 271–278. [Online]. Available: http://dx.doi.org/10.1145/313451.313558

[55] S. Kim, J. E. Clark, and M. R. Cutkosky, "iSprawl: Design and tuning for high-speed autonomous open-loop running," *The International Journal of Robotics Research*, vol. 25, no. 9, pp. 903–912, 2006. [Online]. Available: http://ijr.sagepub.com/cgi/content/abstract/25/9/903

[56] S. Kim, M. Spenko, S. Trujillo, B. Heyneman, V. Mattoli, and M. Cutkosky, "Whole body adhesion: hierarchical, directional and distributed control of adhesive forces for a climbing robot," in *IEEE Int. Conf. on Robotics and Automation*, Rome, Italy, 2007, pp. 1268–1273.

[57] M. Kovač, M. Schlegel, J.-C. Zufferey, and D. Floreano, "Steerable miniature jumping robot," *Autonomous Robots*, vol. 28, no. 3, pp. 295–306, 2010. [Online]. Available: http://www.springerlink.com/content/y64187652016t834/

[58] A. D. Kuo, J. M. Donelan, and A. Ruina, "Energetic consequences of walking like an inverted pendulum: Step-to-step transitions," *Exercise and Sport Sciences Reviews*, vol. 33, no. 2, 2005. [Online]. Available: http://journals.lww.com/acsm-essr/Fulltext/2005/04000/Energetic_Consequences_of_Walking_Like_an_Inverted.6.aspx

[59] G. Kurillo, Z. Li, and R. Bajcsy, "Framework for hierarchical calibration of multiple-camera systems for teleimmersion," in *IMMERSCOM*. ICST, 2009, p. 1.

[60] B. Lambrecht, A. Horchler, and R. Quinn, "A small, insect-inspired robot that runs and jumps," in *IEEE Int. Conf. on Robotics and Automation*, Barcelona, Spain, 2005, pp. 1240–1245.

[61] J. Lee, B. Bush, R. Maboudian, and R. S. Fearing, "Gecko-inspired combined lamellar and nanofibrillar array for adhesion on nonplanar surface," *Langmuir*, vol. 25, no. 21, pp. 12 449–12 453, 10 2009. [Online]. Available: http://dx.doi.org/10.1021/la9029672

[62] J. M. McCarthy, *Geometric Design of Linkages*, 1st ed., J. E. Marsden, L. Sirovich, and S. Wiggins, Eds. Springer, 2000.

[63] O. Mercier and K. N. Melton, "Theoretical and experimental efficiency of the conversion of heat into mechanical energy using shape-memeory alloys," *Journal of Applied Physics*, vol. 52, no. 2, pp. 1030–1037, 1981. [Online]. Available: http://link.aip.org/link/?JAP/52/1030/1

[64] R. Merz, F. Prinz, K. Ramaswami, M. Terk, and L. Weiss, "Shape deposition manufacturing," in *Solid Freeform Fabrication Symposium*. University of Texas at Austin, August 1994.

[65] E. Moore, "Leg design and stair climbing control for the rhex robotic hexapod," Master's thesis, McGill University, 2002.

[66] E. Moore, D. Campbell, F. Grimminger, and M. Buehler, "Reliable stair climbing in the simple hexapod 'rhex'," in *Robotics and Automation, 2002. Proceedings. ICRA '02. IEEE International Conference on*, vol. 3, 2002, pp. 2222 –2227.

[67] J. M. Morrey, B. Lambrecht, A. D. Horchler, R. E. Ritzmann, and R. D. Quinn, "Highly mobile and robust small quadruped robots," in *Intl Conf on Intelligent Robots and Systems*, vol. 1, 2003, pp. 82–87.

[68] R. Murthy, A. Das, and D. Popa, "Arripede: A stick-slip micro crawler/conveyor robot constructed via 2 x00bd;d mems assembly," in *Intelligent Robots and Systems, 2008. IROS 2008. IEEE/RSJ International Conference on*, sept. 2008, pp. 34 –40.

[69] D. H. Page, "A theory for the elastic modulus of paper," *Brit. J. Appl. Phys.*, vol. 16, pp. 253–258, 1965.

[70] K. S. J. Pister, M. W. Judy, S. R. Burgett, and R. Fearing, "Microfabricated hinges," *Sensors and Actuators*, vol. 33, pp. 249–256, 1992.

[71] J. Proctor and P. Holmes, "Steering by transient destabilization in piecewise-holonomic models of legged locomotion," *Regular and Chaotic Dynamics*, vol. 13, no. 4, pp. 267–282, 2008. [Online]. Available: http://dx.doi.org/10.1134/S1560354708040047

[72] M. H. Raibert, J. Brown, H. Benjamin, and M. Chepponis, "Experiments in Balance with a 3D One-Legged Hopping Machine," *The International Journal of Robotics Research*, vol. 3, no. 2, pp. 75–92, 1984. [Online]. Available: http://ijr.sagepub.com/cgi/content/abstract/3/2/75

[73] R. Sahai, R. E. Groff, E. Steltz, M. Seeman, and R. S. Fearing, "Towards a 3g crawling robot through the integration of microrobot technologies," in *IEEE Int. Conf. on Robotics and Automation*, May 2006.

[74] R. Sahai, E. Steltz, and R. S. Fearing, "Carbon fiber components with integrating wiring for millirobot prototyping," in *International Conference on Robotics and Automation*. IEEE, 2005.

[75] U. Saranli, M. Buehler, and D. E. Koditschek, "RHex: A simple and highly mobile hexapod robot," *The Int. J. of Robotics Research*, vol. 20, no. 7, pp. 616–631, 2001.

[76] J. Schmitt and P. Holmes, "Mechanical models for insect locomotion: dynamics and stability in the horizontal plane I. theory," *Biol. Cyber.*, vol. 83, no. 6, pp. 501–515, 2000.

[77] ——, "Mechanical models for insect locomotion: dynamics and stability in the horizontal plane –II. application," *Biological Cybernetics*, vol. 83, no. 6, pp. 517–527, 11 2000. [Online]. Available: http://dx.doi.org/10.1007/s004220000180

[78] J. Seipel and P. Holmes, "A simple model for clock-actuated legged locomotion," *Regular and Chaotic Dynamics*, vol. 12, no. 5, pp. 502–520, 2007.

[79] J. Selig and X. Ding, "A screw theory of static beams," *Intelligent Robots and Systems, 2001. Proceedings. 2001 IEEE/RSJ International Conference on*, vol. 1, pp. 312–317 vol.1, 2001.

[80] R. T. Shield and W. Prager, "Optimal structure design for given deflection," *Zeitschrift für Angewandte Mathematik und Physik (ZAMP)*, vol. 21, no. 4, pp. 513–523, July 1970.

[81] A. Spence, S. Revzen, J. Seipel, C. Mullens, and R. Full, "Insects running on elastic surfaces," *Journal of Experimental Biology*, In preparation.

[82] S. Sponberg and R. J. Full, "Neuromechanical response of musculo-skeletal structures in cockroaches during rapid running on rough terrain," *J Exp Biol*, vol. 211, no. 3, pp. 433–446, 2008. [Online]. Available: http://jeb.biologists.org/cgi/content/abstract/211/3/433

[83] E. E. Steltz, "Redesign of the micromechanical flying insect in a power density context," Ph.D. dissertation, University of California, Berkeley, 2008.

[84] C. R. Taylor, K. Schmidt-Nielsen, and J. L. Raab, "Scaling of energetic cost to body size in mammals," *Am. J. Physiol.*, vol. 210, pp. 1104–1107, 1970.

[85] M. A. Thrasher, A. R. Shahin, P. H. Meckl, and J. D. Jones, "Efficiency analysis of shape memory alloy actuators," *Smart Materials and Structures*, vol. 3, no. 2, p. 226, 1994. [Online]. Available: http://stacks.iop.org/0964-1726/3/i=2/a=019

[86] B. P. Trease, Y. Moon, and S. Kota, "Design of large displacement compliant joints," *Journal of Mechanical Design*, vol. 127, no. 4, pp. 788–798, July 2005.

[87] W. S. N. Trimmer, "Microrobots and micromechanical systems," *Sensors and Actuators*, vol. 19, pp. 267–287, 1989.

[88] R. von Mises, "Motorrechnung, ein neues hilfsmittel in der mechanik," *Zeitschrift für Angewandte Mathematik und Physik (ZAMP)*, vol. 4, no. 2, pp. 155–181, 1924, English translation by E.J. Baker and K. Wohlhart. Motor Calculus, a New Theoretical Device for Mechanics. Institute for Mechanics, University of Technology Graz, Austria 1996.

[89] R. J. Wood, "The first takeoff of a biologically inspired at-scale robotic insect," *IEEE Trans. Robotics*, vol. 24, no. 2, pp. 341–347, April 2008.

[90] R. J. Wood, S. Avadhanula, M. Menon, and R. S. Fearing, "Microrobotics using composite materials: The micromechanical flying insect thorax," in *International Conference on Robotics and Automation*. Taipei, Taiwan: IEEE, Sep. 2003.

[91] R. J. Wood, S. Avadhanula, R. Sahai, E. Steltz, and R. S. Fearing, "Microrobot design using fiber reinforced composites," *J. Mech. Design*, vol. 130, no. 5, May 2008.

[92] R. J. Wood, S. Avadhanula, E. Steltz, M. Seeman, J. Entwistle, A. Bachrach, G. Barrows, S. Sanders, and R. Fearing, "Enabling technologies and subsystem integration for an autonomous palm-sized glider," *IEEE Robotics and Automation Magazine*, vol. 14, pp. 82–91, 2007.

[93] R. J. Wood, E. Steltz, and R. S. Fearing, "Nonlinear performance limits for high energy piezoelectric bending actuators," in *IEEE Int. Conf. on Robotics and Automation*, Barcelona, Spain, April 2005.

[94] R. J. Wood, E. Steltz, and R. Fearing, "Optimal energy density piezoelectric bending actuators," *Sensors and Actuators A: Physical*, vol. 119, no. 2, pp. 476 – 488, 2005. [Online]. Available: http://www.sciencedirect.com/science/article/B6THG-4F05G63-2/2/479c823e48f9592c889532f2ddfc8182

[95] J. Yan, S. A. Avadhanula, J. Birch, M. H. Dickinson, M. Sitti, T. Su, and R. S. Fearing, "Wing transmission for a micromechanical flying insect," *Journal of Micromechatronics*, vol. 1, pp. 221–237, 1 July 2001.

[96] J. Yan, R. J. Wood, S. Avadhanula, M. Sitti, and R. S. Fearing, "Towards flapping wing control for a micromechanical flying insect," in *ICRA*. IEEE, 2000.

[97] R. Yeh, E. J. J. Kruglick, and K. S. J. Pister, "Surface-micromachined components for articulated microrobots," *J. Microelectromechanical Systems*, vol. 5, pp. 10–17, 1996.

[98] L. Yin and G. K. Ananthasuresh, "Design of distributed compliant mechanisms," *Mechanics Based Design of Structures and Machines*, vol. 31, no. 2, pp. 151–179, 2003.

[99] A. Yumaryanto, J. An, and S. Lee, "A cockroach-inspired hexapod robot actuated by lipca," in *IEEE Conf. on Robotics, Automation, and Mechatronics*, Dec. 2006, pp. 1–6.